OBSERVATION AND MODELING OF VERTICAL HEAT EXCHANGE OF LAKES IN NAMCO BASIN, TIBETAN PLATEAU

Binbin Wang

OBSERVATION AND MODELING OF VERTICAL HEAT EXCHANGE OF LAKES IN NAMCO BASIN, TIBETAN PLATEAU

DISSERTATION

to obtain
the degree of doctor at the University of Twente,
on the authority of the rector magnificus,
prof.dr. T.T.M. Palstra,
on account of the decision of the Doctorate Board,
to be publicly defended
on Friday 12 April 2019 at 16:45 hrs

by

Binbin Wang
born on 17 November 1986
in Henan Province, China

This dissertation has been approved by
Prof.dr. Z. Su, Supervisor
Prof.dr. Y. Ma, Supervisor

ITC dissertation number 348
ITC, P.O. Box 217, 7500 AE Enschede, The Netherlands

ISBN 978-90-365-4750-5
DOI 10.3990/1.9789036547505

Cover designed by Benno Masselink
Printed by ITC Printing Department

UNIVERSITY OF TWENTE.

FACULTY OF GEO-INFORMATION SCIENCE AND EARTH OBSERVATION

Graduation committee:

Chairman/Secretary

Prof.dr.ir. A. Veldkamp

Supervisors

Prof.dr. Z. Su
Prof.dr. Y. Ma

Members:

Prof.dr.ir. A. Veldkamp	University of Twente
Dr. S. Salama	University of Twente
Prof.dr. K. Yang	ITP / Tsinghua University
Prof.dr. G. Kirillin	Leibnitz Institute of Freshwater Ecology and Inland Fisheries
Prof.dr. M. Menenti	TU Delft / Capital Normal University

Contents

Acknowledgements

Six years of long PhD journey is approaching to an end and I feel grateful to many people during my study periods of three years in Enschede, Netherlands and three years in Beijing, China. Without all your help and accompany, I could not even achieve my research objectives and accomplish this thesis; and I want to express my sincere gratitude to all of you and to finish the most important content of this thesis.

First and foremost, I want to express the most sincere gratitude to my promoter, Prof. Bob Su. I still remember that your initial two simple questions (How is the evaporation from a high-elevation lake with environments of strong solar radiation and low air density? How could we obtain the lake evaporation by our observations?) aroused my interests and opened my journey of the lake research in the high-elevation Third Pole region. Every time when I have doubts on research issues, you could always discuss questions with your wealthy knowledge and point out directions for me. Your modesty, knowledge, patient, and enthusiasm set an excellent example for me to my research career, and I want to express my sincere respect to you, to my captain.

I express my deeply thanks to another important promoter and supervisor, Prof. Yaoming Ma. You gave me the chance to start the abroad study in Netherlands and supported the lake research from every aspects: instrument erection design, financial support, discussion and solution of academy problems, research publication and etc. You also provide free development space for all aspects of my growth, where I have developed from an ignorant and green researcher to an independent and mature one. Every time when I'm confused with my work and life, I could always find help from your wise and farsighted advises.

I would like to express my sincere thanks to Prof. Weiqiang Ma. I still remember that you helped to install the automatic weather station on the island in 2015 and give suggestions and supports for academic research of lakes. And I also thank to Professor Xuelong Chen greatly. You are the one who firstly guided me to set up instruments over the lakes; and also encouraged me to response to hard questions when I doubted about quality of the manuscript; and the contents are revised in a much better shape and finally are published. I would like to thank Professor Maoshan Li, who are the one that took me to the Tibetan Plateau for field work for the first time of my life.

Many thanks should also be given to Prof. Kun Yang and his group. You set a good example for me in doing research. Your hard working, rigorous altitude,

tireless teaching and diligent pursuit of science also influence me on my altitude of living and studying. The edification of “research is not just about publishing papers, but for advance scientific progress with good objectives” is rooted in my mind. I feel fortunate to be able to learn from you in my research journey. I also want to show my highly respective to Prof. Massimo Menenti. I gain a lot from you, not only in the office academic discussion, but also on the trips to the field on the Tibetan Plateau.

The PhD experience in Netherland is a valuable asset of my life and I feel so lucky to study and work with so many good colleagues in groups of Prof. Bob Su and Prof. Yaoming Ma. I give special thanks to the secretaries of Water Resources Department, Anke and Tina and thanks for your help in every aspects of my study in Enschede. I also thank to my colleagues and friends in ITC, Netherlands, including: Rong Liang and Yijian Zeng, Xiaojing Wu and Donghai Zheng, Hong Zhao and Wen Bai, Jing Liu and Peiqi Yang, Suhyb, Shaoning Lv, Chandra, Ying Huang, Qiang Wang, Junping Du, Min Xu, Chengliang Liu, Lianyu Yu, Xu Yuan, Novi, Xiaolong Yu, Yifang Shi, Ruosha Zeng, Bo Zhang, Pei Zhang, Zhuola, Cesar, Harm-Jan, Haris, Lichun Wang, Mireia, and many others. And I also thanks my friends and colleagues in Institute of Tibetan Plateau Research Chinese Academy of Sciences in China: Fanglin Sun, Zhongyan Wang, Yongjie Wang, Zhangwei Ding, Zhikun Zhu, Chao Xu, Lian Liu, Yue Lai, Jie Xu, Yuyang Wang, Ling Yuan and many others. I thank to “Chinese Scholarship Council” for supporting me to study in Netherlands for 2013.

Lastly, I want to thank my mom and my wife for your endless love and support. My sweetheart, Yan Wang, I could not accomplish this thesis without your encouragement and tolerance. There are many interesting things in life waiting for us to explore and accomplish; and I feel so lucky and also confidence to be with you for a beautiful future worth looking forward to.

Summary

Lakes are an important part of the landscape on the Tibetan Plateau (TP). They impact atmosphere boundary layer processes and are thus important for local climate modeling and catchment-scale water and heat budget analysis. However, due to lack of observational data and adequate modeling systems, studies that examine lake-atmosphere interaction and evaporation are very limited and the results show large uncertainties. Thus, observation and modeling of vertical heat exchange including the characteristics of lake-atmosphere interaction, the precise evaporation of water bodies, the energy budget and water balance, the lakes' response to climate change show high priority and strong significance for research over high-elevation lakes of the TP.

To understand the vertical heat exchange in lakes over the TP, the closed lake basin of Nam Co is chosen as our study area, where meteorological and hydrological observations over a grass land station since 2005 could provide enormous climatological data. In addition, field experiments with eddy covariance (EC) observation systems, four component radiation sensors and instruments for measuring water temperature profiles were carried out in the small Nam Co lake ("small lake" for short hence force) during April 2012 to October 2014 and in the island of Nam Co lake ("large lake" for short hence force) during July 2015 to now. These comprehensive datasets together with the supplemental satellite data can be used to address for the above mentioned issues in Chapter 3 to Chapter 6, respectively.

Firstly, Chapter 3 focuses on observation and modeling of lake-atmosphere interaction processes of the "small lake". We found that the lake-atmosphere temperature and humidity gradients are positive during the ice-free season, and unstable and neutral atmosphere conditions dominate in the "small lake". The typical value of roughness lengths for momentum is 3.35×10^{-4} m, while the roughness length for water is larger than that for heat. As influenced by free convection, it gives a square root dependence of latent heat flux on wind speed. After that, by selecting observations of lake-atmosphere interaction through footprint and data quality control, two lake-atmosphere interaction methods (Bulk aerodynamic transfer method and multi-layer method, B method and M method for short hence force) are evaluated by in-situ eddy covariance observations. The results indicate that the two methods show high consistency, but both show underestimation of turbulent heat flux compared with observations. The underestimation of turbulent heat flux is found to be related to the

underestimation of roughness lengths. After we optimized the Charnock number from 0.013 to 0.031 and the roughness Reynold number from 0.11 to 0.54 through EC observations, the simulated momentum roughness lengths are also much closer to the observations and the simulated friction velocity and turbulent heat flux also show obvious improvement.

Secondly, Chapter 4 deals with the precise estimation of evaporation, understands the physical controls on turbulent flux and finally analyzes lakes' energy budget by using in-situ observations introduced in Chapter 2 and the B method evaluated in Chapter 3. Because of the limitation due to eddy covariance observations at the lake shore, the B method, with parameters optimized for momentum roughness length in the two water bodies, is used to provide reliable and consistent results for data interpolation of EC measurements with inadequate footprint or bad quality due to malfunction of the EC instrument. After that, we found that: the diurnal variation of sensible heat flux and latent heat flux have quite different diurnal patterns, with the former peaking in the early morning and the latter peaking in the afternoon. For the "small lake", wind speed shows significance at temporal scales of half-hourly, whereas water vapor and temperature gradients have higher correlations over temporal scales of daily and monthly in lake-air turbulent heat exchange. For the "large lake", temperature gradient has higher correlation coefficient to sensible heat flux than that by wind speed, while wind speed has larger correlation coefficient to latent heat flux than that by water vapor gradient. The evaporation during the ice-free season (April to November) of the "small lake" is approximately 812 mm while the evaporation during the ice-free season (May to January) of the "large lake" is around 981 ± 18 mm. The energy budget during the open water period of the "small lake" is generally closed, with a value of approximately 0.97; while the energy budget closure ratio during July to November of the "large lake" is 0.859.

After that, with the obtained data series of meteorological variables and turbulent heat flux in the two water bodies, Chapter 5 explores the differences of lake-atmosphere interaction parameters, meteorological variables and turbulent heat fluxes between the "small lake" and the "large lake", and significant differences exist in their lake-atmosphere interaction processes due to differences in their inherent attributes and environmental backgrounds. Relative to the "small lake", maximum surface temperature of the "large lake" is approximately 3 ℃ lower, in addition to a larger wind speed, a higher monthly average air temperature and delayed peaks of seasonal variations of water and air temperature. The typical values of roughness length and standard bulk transfer coefficient for momentum

are about 80% and 21% higher respectively in the “large lake”. The typical values of roughness lengths for heat and water are one order of magnitude lower in the “large lake” while the corresponding standard bulk transfer coefficients are only 7% lower. The latent and sensible heat fluxes of the two lakes have quite different seasonal variations, with evaporation peaking in November over the “large lake” and in June over the “small lake”. The estimated evaporation during ice-free season of the “large lake” (around 981 ± 18 mm) is also higher than that (812 mm) in the “small lake”, which is mainly related to the lower Bowen ratio observed for the "large lake". Our results show evidences that it is inappropriate to evaluate lake evaporation by Pan observations, especially for its seasonal variation.

Lastly, Chapter 6 quantifies lake evaporation over the two high-elevation lakes, investigates lakes’ responses to climate change and determines the dominant driving forces behind. Two methods (one for traditional evaporation estimation method in the “small lake” and the other with Flake modeling in the “large lake”) are used for long term trend analysis:

For the first method, ten methods for estimating evaporation at a temporal resolution of 10 days over the “small lake” were evaluated by using eddy covariance (EC) observation-based reference datasets. After examination of the consistency of the parameters used in the different methods, the ranking of the methods under different conditions are shown to be inconsistent. The Bowen ratios derived from meteorological data and EC observations are consistent, and it supports a ranking of energy-budget-based methods (including the Bowen Ratio Energy Budget, Penman, Priestley-Taylor, Brutsaert-Stricker and DeBruin-Keijman methods) as the best when heat storage in the water can be estimated accurately. The elevation-dependent psychometric constant can explain the differences between the Priestley-Taylor and DeBruin-Keijman methods. The Dalton-type methods (Dalton and Ryan-Harleman methods) and radiation-based method (Jensen-Haise) all improve significantly after parameter optimization, with better performance by the former than the latter. The deBruin method yields the largest error due to the poor relationship between evaporation and the drying power of the air. The good performance of the Makkink method, with no significant differences before and after optimization, indicates the importance of solar radiation and air temperature in estimation of lake evaporation. The Makkink method was used for long-term evaporation estimation due to lack of water temperature observations in lakes on the TP. Lastly, long-term evaporation during the open-water period (April 6th to November 15th from 1979 to 2015)

were obtained; the mean bias was only 6% for average over years 2012 and 2013. A decreasing-increasing trend in lake evaporation with a turning point in 2004 was noted, and this trend corresponds to the published decreasing-increasing trend in reference evapotranspiration on the TP and can be explained by variations in related meteorological variables.

For the second method, the performances of Flake modeling through ITP (Institute of Tibetan Plateau Research) forcing are evaluated by eddy covariance and meteorological data over the "small lake" during 2012-2013 and over the "large lake" during 2015-2016. The results indicate that the observed mixed layer depth (D_{ml}) in the "large lake" show clearly diurnal variation with monthly averaged amplitude of approximately 8 m and it results from the significant surface warming during the day and surface cooling at night. Flake simulations could reproduce the seasonal variations of water surface temperature (T_s) and D_{ml} over daily and seasonal resolutions, but the amplitude of simulated T_s and D_{ml} are significantly underestimated. Further, the seasonal variations of simulated sensible heat flux (*H*) and latent heat flux (*LE*) are close to the observations with a proper extinction coefficient and lake depth, with RMSE values of simulated daily T_s, *H* and *LE* of only about 1 ℃, 8 W m^{-2} and 22 W m^{-2} respectively. The simulated *LE* through land-dominated forcing shows clear underestimation compared to that by lake-dominated forcing, and the reasons result from the observed larger wind speed and warmer air temperature in the latter. In addition, no significant differences exist for the simulations with different forcing used in the "small lake". Lake warming and increasing trends of simulated *H* and *LE* are found through long term simulations of corrected ITP forcing. Downward longwave radiation ($R_{l\downarrow}$), rather than air temperature, is considered to play the dominant role in lakes' response to climate change. Our results found the significance of lake-dominant observations in lake modeling over the "large lake" and suggest the importance of $R_{l\downarrow}$ in lake warming and in trends of simulated *H* and *LE*.

Samenvatting

Meren vormen een belangrijk onderdeel van het landschap op het Tibetaans Plateau (TP). Ze zijn van invloed op processen in de atmosferische grenslaag, en zijn daarom belangrijk voor lokale klimaatmodellering en de analyse van water- en warmtebalansen op stroomgebiedsniveau. Vanwege een gebrek aan observaties en adequate modelsystemen zijn studies naar de meer-atmosfeer-interactie en verdamping echter beperkt en de resultaten tonen grote onzekerheden. Daarom hebben de observatie en modellering van verticale warmte-uitwisseling, waaronder de karakteristieken van de meer-atmosfeer-interactie, de verdamping vanuit waterlichamen, de energiebalans en waterbalans, en de respons van de meren op klimaatverandering een hoge prioriteit en zijn van groot belang voor onderzoek van de meren op de grote hoogte van het TP.

Om de verticale warmte-uitwisseling in meren op het TP te begrijpen is het gesloten meer-systeem van Nam Co gekozen als ons studiegebied. Meteorologische en hydrologische waarnemingen van een graslandstation leveren sinds 2005 een enorme hoeveelheid klimatologische data op. Daarnaast zijn veldexperimenten gedaan met eddy covariantie (EC)-systemen, vier componenten stralingssensoren en instrumenten voor het meten van watertemperatuurprofielen, van april 2012 tot oktober 2014 in het kleine Nam Co meer (vanaf hier "klein meer" genoemd) en van juli 2015 tot nu op het eiland in het Nam Co meer (vanaf hier "groot meer" genoemd). Deze uitgebreide datasets en aanvullende satellietgegevens zijn gebruikt om de bovengenoemde problemen te onderzoeken in hoofdstuk 3 tot en met hoofdstuk 6.

Hoofdstuk 3 behandelt de observatie en modellering van meer-atmosfeer-interactieprocessen van het "kleine meer". We hebben gevonden dat gedurende het ijsvrije seizoen de meer-atmosfeer temperatuur- en vochtigheidsgradiënten een positieve waarde hebben en dat instabiele en neutrale atmosferische condities dominant zijn voor het "kleine meer". De typische waarde van ruwheidslengte voor momentum is 3.35×10^{-4} m, en de ruwheidslengte is groter voor water dan voor warmte. Onder invloed van vrije convectie geeft dit een wortelverband van latente warmteflux op windsnelheid. Daarna, door de selectie van observaties van de meer-atmosfeer-interactie op basis van voetafdruk en gegevenskwaliteitscontrole, worden twee meer-atmosfeer-interactiemethoden (de bulk aerodynamische overdrachtsmethode en de meerlaagse methode, vanaf hier B-methode en M-methode genoemd) geëvalueerd met in situ EC-observaties. De resultaten laten zien dat de twee methodes een grote consistentie hebben, maar

beiden onderschatten de turbulente warmteflux in vergelijking met de observaties. De onderschatting van de turbulente warmteflux blijkt gerelateerd te zijn aan de onderschatting van ruwheidslengtes. Nadat we het Charnock-getal van 0.013 tot 0.031 en het ruwheidsgetal van Reynold van 0.11 tot 0.54 hebben geoptimaliseerd op basis van EC-observaties, komen de gesimuleerde momentum ruwheidslengtes veel dichter bij de waarnemingen en de gesimuleerde wrijvingssnelheid en turbulente warmteflux vertonen ook een duidelijke verbetering.

Hoofdstuk 4 behandelt de bepaling van verdamping, de fysische effecten op turbulente flux en tenslotte de energiebalans van de meren op basis van de in situ observaties (hoofdstuk 2) en de B-methode die geëvalueerd is in hoofdstuk 3. Vanwege de beperking dat de EC-observaties bij de oever van het meer zijn gedaan wordt de B-methode, met parameters geoptimaliseerd voor momentum ruwheidslengte van de twee waterlichamen, gebruikt voor betrouwbare en consistente resultaten van data-interpolatie van de EC-observaties met een inadequate voetafdruk of slechte kwaliteit ten gevolge van storing van het EC-instrument. Daarna hebben we ontdekt dat de dagelijkse variatie van de voelbare warmteflux en de latente warmteflux een verschillend dagelijks patroon hebben, waarbij de eerste maximaal is in de vroege ochtend en de tweede ’s middags maximaal is. Voor de turbulente warmte-uitwisseling tussen het meer en lucht van het “kleine meer” toont windsnelheid significantie op de tijdschaal van een halfuur, terwijl waterdamp- en temperatuurgradiënten hogere correlaties hebben op tijdschalen van een dag en een maand. Voor het “grote meer” heeft de temperatuurgradiënt een hogere correlatie met voelbare warmteflux dan windsnelheid, terwijl windsnelheid een hogere correlatie heeft met latente warmteflux dan de waterdampgradiënt. De verdamping tijdens het ijsvrije seizoen (april tot november) van het “kleine meer” is ongeveer 812 mm, terwijl de verdamping tijdens het ijsvrije seizoen (mei tot januari) van het “grote meer” ongeveer 981 ± 18 mm is. De energiebalans tijdens de open water periode van het “kleine meer” is over het algemeen gesloten met een waarde van ongeveer 0.97, terwijl de sluitingsratio van de energiebalans van het “grote meer” van juli tot november 0.859 is.

Vervolgens, met de verkregen datareeksen van meteorologische variabelen en turbulente warmteflux voor de twee waterlichamen, onderzoekt hoofdstuk 5 de verschillen in meer-atmosfeer-interactieparameters, meteorologische variabelen en turbulente warmtefluxen tussen het “kleine meer” en het “grote meer”. Er bestaan aanzienlijke verschillen in hun meer-atmosfeer-interactieprocessen

vanwege verschillen in hun inherente eigenschappen en omgevingsfactoren. Vergeleken met het "kleine meer" is de maximale oppervlaktetemperatuur van het "grote meer" ongeveer 3 ℃ lager, is de windsnelheid hoger, de gemiddelde luchttemperatuur per maand hoger en zijn de pieken van seizoensvariaties van de water- en luchttemperatuur vertraagd. De typische waarden van ruwheidslengte en standaard bulkoverdrachtscoëfficiënt voor momentum zijn respectievelijk ongeveer 80% en 21% hoger voor het "grote meer". De typische waarden van ruwheidslengtes voor warmte en water zijn één orde van grootte lager in het "grote meer", terwijl de bijbehorende standaard bulkoverdrachtscoëfficienten slechts 7% lager zijn. De latente en voelbare warmtefluxen van de twee meren hebben verschillende seizoensvariaties, waarbij de piek van verdamping voor het "grote meer" in november is en voor het "kleine meer" in juni. De geschatte verdamping tijdens het ijsvrije seizoen van het "grote meer" (ongeveer 981 ± 18 mm) is ook hoger dan die van het "kleine meer" (812 mm), wat voornamelijk te maken heeft met de lagere Bowen-ratio die is waargenomen voor het "grote meer". Onze resultaten tonen aan dat Pan-metingen van verdamping niet geschikt zijn om meer-verdamping te evalueren, vooral vanwege de seizoensgebonden variatie.

Hoofdstuk 6 kwantificeert de meer-verdamping voor de twee hooggelegen meren, onderzoekt de respons van de meren op klimaatverandering en bepaalt de dominante drijvende krachten hierachter. Twee methodes (een traditionele verdampingsschattingsmethode voor het "kleine meer" en Flake-modellering voor het "grote meer") worden gebruikt voor een lange termijn trendanalyse:

Voor de eerste methode zijn tien methodes voor het schatten van verdamping met een temporele resolutie van 10 dagen voor het "kleine meer geëvalueerd met de op EC-observaties gebaseerde referentiedata. Na onderzoek van de consistentie van de parameters die in de verschillende methodes worden gebruikt, blijkt de rangorde van de methodes inconsistent te zijn voor verschillende omstandigheden. De Bowen-ratio's van de meteorologische gegevens en EC-observaties zijn consistent, en ondersteunen een klassering van methodes op basis van energiebalans (waaronder de Bowen-ratio energiebalans, Penman, Priestley-Taylor, Brutsaert-Stricker en DeBruin-Keijman methodes) als beste als de warmteopslag in het water nauwkeurig bepaald kan worden. De hoogteafhankelijke psychometrische constante verklaart de verschillen tussen de Priestley-Taylor en de DeBruin-Keijman methode. De Dalton-type methodes (de Dalton en Ryan-Harleman methodes) en de op straling gebaseerde methode (Jensen-Haise) verbeteren aanzienlijk na optimalisatie van de parameters, waarbij

de eerstgenoemden beter presteren dan de laatstgenoemde. De DeBruin methode levert de grootste fout op vanwege de slechte relatie tussen verdamping en de droogkracht van de lucht. De goede prestatie van de Makkink methode, zonder significante verschillen voor en na optimalisatie, geven het belang aan van zonnestraling en luchttemperatuur bij de schatting van meer-verdamping. De Makkink methode is gebruikt voor lange termijnschattingen van verdamping vanwege het ontbreken van observaties van watertemperaturen in meren op het TP. Tenslotte is lange termijn verdamping verkregen voor de open water periode (6 april tot 15 november van 1979 tot 2015); de gemiddelde bias was slechts 6% voor het gemiddelde over de jaren 2012 en 2013. Een keerpunt van een dalende trend in meer-verdamping naar een stijgende trend was opgemerkt voor 2004, en deze trend komt overeen met de gepubliceerde dalende-stijgende trend in referentieverdamping op het TP en kan verklaard worden door variaties in gerelateerde meteorologische variabelen.

Voor de tweede methode worden de prestaties van de Flake-modellering, met forcering die is ontwikkeld door het ITP (Institute of Tibetan Plateau Research), geëvalueerd met EC en meteorologische gegevens voor het "kleine meer" gedurende 2012-2013 en voor het "grote meer" gedurende 2015-2016. De resultaten laten zien dat de geobserveerde diepte van de gemengde laag (D_{ml}) in het "grote meer" een dagelijkse variatie heeft met een maandelijks gemiddelde amplitude van ongeveer 8 m. Dit is het gevolg van significante opwarming van het oppervlak gedurende de dag en afkoeling van het oppervlak gedurende de nacht. Flake-simulaties kunnen de seizoensgebonden variaties van de temperatuur van het oppervlaktewater (T_s) en D_{ml} op dagelijkse en seizoensschaal reproduceren, maar de amplitudes van gesimuleerde T_s en D_{ml} worden aanzienlijk onderschat. Verder liggen de seizoensvariaties van gesimuleerde voelbare warmteflux (*H*) en latente warmteflux (*LE*) dicht bij de observaties met een juiste extinctiecoëfficiënt en diepte van het meer, met RMSE-waarden van gesimuleerde dagelijkse T_s, *H* en *LE* van respectievelijk slechts ongeveer 1 ℃, 8 W m^{-2} en 22 W m^{-2}. De gesimuleerde LE met land-gedomineerde forcering toont een duidelijke onderschatting vergeleken met meer-gedomineerde forcering. De redenen hiervoor zijn de geobserveerde grotere windsnelheid en warmere luchttemperatuur bij de laatstgenoemde. Er bestaan geen significante verschillen voor de simulaties met verschillende forceringen voor het "kleine meer". Opwarming van het meer en stijgende trends van gesimuleerde *H* en *LE* worden gevonden in lange termijnsimulaties met gecorrigeerde ITP-forcering. Neerwaartse langgolvige straling ($R_{l\downarrow}$), in plaats van luchttemperatuur, wordt

geacht om de dominante rol te spelen in de respons van meren op klimaatverandering. Onze resultaten laten het belang zien van de meer-dominante observaties in de meer-modellering van het "grote meer" en suggereren het belang van $R_{l\downarrow}$ in de opwarming van het meer en in trends van gesimuleerde H en LE.

Chapter 1 Introduction

1.1 Research background

1.1.1 Largest high-elevation lake zone of the world

The global extent of natural lakes has a number of 304 million and an area of 4.2 million km^2, and these water bodies account for about larger than 3% of the earth's continental "land" surface (Downing et al. 2006). Tibetan Plateau (TP) is considered as "Asia's water tower" and the "Third Pole of the Earth", and it forms the largest high-elevation inland lake zone, which has an average elevation of about 4 km above sea level (a.s.l.) and lake numbers of approximately 32843 (Zhang et al. 2014). Amongst these lakes, approximately 1204 are larger than 1 km^2 and the rest are smaller than 1 km^2. The lake area with a value of 43151.08 ± 411.49 km^2 makes up 1.4% of the total area of the TP (Wang and Dou 1998; Zhang et al. 2014).

Widely accepted as an important climate indicator in this climate sensitive area, lakes generally show an obvious expansion in the central of TP due to increased precipitation and glacier retreating (Yang et al. 2017; Zhang et al. 2014). Observation and modeling of low-elevation lakes have been conducted world widely, however, due to harsh climatic conditions and the difficulties associated with measuring these parameters over the high-elevation water surface on the TP, little attention was paid to observation and modeling of lake-air water and heat exchange during previous TP energy and water cycle experiments (such as the GAME/Tibet-Global Energy and Water Cycle Experiment, and the CAMP/Tibet-Coordinated Enhanced Observing Period Asia-Australia Monsoon Project) (Ma et al. 2002; Ma et al. 2006; Ma et al. 2004; Tanaka et al. 2001; Tanaka et al. 2003; Yang et al. 2008).

1.1.2 Lake-atmosphere interaction processes

Observations in low-elevation lakes have shown that heat and water exchange between lakes and the overlying atmosphere differs from the exchange between land and atmosphere. The solar heating over the lake could be stored in the water in Spring and be released for atmospheric heating in Autumn. Lakes can influence local climate via vertical heat and water exchange (i.e. sensible heat flux and latent heat flux) through lake-land breeze circulation and the alteration of local precipitation (Blanken et al. 2003; Blanken et al. 2011; Lee et al. 2014; Liu et al. 2009a; Venalainen et al. 1999; Verburg and Antenucci 2010; Xiao et al. 2013).

The lake-air heat and water exchange is not only related to the lake surface conditions, such as lake surface temperature, ice coverage, lake depth, and waves, but is also influenced by the surrounding environment and atmospheric conditions (Blanken et al. 2003; Blanken et al. 2011; Gao et al. 2006; Panin et al. 2006; Spence et al. 2011). For example, a stable/unstable atmosphere can reduce/increase the heat loss from lake water (Brutsaert 1982). Due to the relatively greater heating and cooling effect from the surrounding land, small lakes generally have a more variable atmospheric boundary layer than large lakes (Deng et al. 2012; Katsaros 1998). The phase shift of seasonal variations of air temperature, latent heat flux, sensible heat flux to the net radiation are different for lakes with different depths, areas, thermal capacities, as well as environmental and climatic conditions.

Lake has inherent characteristics of lower albedo, smaller roughness length, higher thermal conductivity and larger thermal capacity relative to surrounding land area. Such properties could cool the atmosphere in summer and warm the atmosphere in winter (Wen et al. 2015), influence the diurnal and seasonal variation of air temperature, weaken/strengthen the turbulent heat flux (Long et al. 2007; Zhu et al. 2017), promote the annual precipitation amounts (Thiery et al. 2015; Wen et al. 2015) and alter the distribution of energy budget components (Long et al. 2007; Rouse et al. 2005). Due to its significance in catchment-scale water balance, energy budget and climate change (Martynov 2012; Rouse et al. 2005; Subin et al. 2012; Thiery et al. 2015; Wen et al. 2015; Zhou et al. 2013), enormous lake models have been applied and evaluated over different environments world widely (Perroud et al. 2009; Stepanenko et al. 2014b; Thiery et al. 2014b), also on the TP recently (Huang et al. 2017; Kirillin et al. 2017; Lazhu et al. 2016; Wen et al. 2016; Zhu et al. 2017). Thus, in presence of high elevation, strong solar heating, less impact of human activities, quantitatively analysis of lake-atmosphere interaction processes based on eddy covariance observations over the vast majority of lakes over the TP show higher priority for hydrologic, meteorological and ecological studies in this area. And it also becomes paramount that the reliability is established of different methods for estimation of evaporation for long term evaporation analysis based on direct observational evidence.

1.1.3 Lake evaporation related studies

TP is the source region of many large rivers in Asia and its water resources could raise billions of people downstream. Lake evaporation is an important component

in catchment scale hydrological cycle, energy budget and water balance analysis (See Table (1.1) for collected references on topics of lake evaporation and evaporation related issues over the TP). The evaporation could be estimated by methods of Pan evaporation (Li et al. 2007; Liu et al. 2009b; Shi et al. 2010; Zhou et al. 2013b), bulk transfer method (Haginoya et al. 2009; Xu et al. 2009; Yu et al. 2011), Flake model (Lazhu et al. 2016), Complementary Relationship Lake Evaporation (CRLE) model (Ma et al. 2016), Penman-Moteith method (Li et al. 2001; Wu et al. 2014; Zhang et al. 2011a; Zhu et al. 2010) and direct eddy covariance (EC) observations (Guo et al. 2016; Li et al. 2016; Li et al. 2015b; Liu et al. 2014; Wang et al. 2017; Wen et al. 2016). The reported evaporation from Pan observations and model simulations over the same lake (i.e. in Nam-Co) show very large discrepancy in their seasonal variations and annual amounts (Lazhu et al. 2016; Ma et al. 2016; Wang et al. 2017; Wu et al. 2014; Xu et al. 2009; Zhu et al. 2010). The difference in estimated evaporation, i.e. around 600 mm in Zhou et al. (2013) and around 1430 mm in Zhu et al. (2010) in lake Nam-Co, could lead to contrary water balance conclusions. Moreover, models such as Flake (Lazhu et al. 2016) and CRLE (Ma et al. 2016) have recently been used to derive lake evaporation in Nam-Co, however, opposite evaporation trends have been reported using the same forcing data. These inconsistencies may result from the facts that: (1) Pan evaporation, widely used as a validation dataset for actual lake evaporation, may result in significant errors due to the differences in sizes of water body and also the differences in their overlying atmosphere and environments; (2) Bulk transfer method, in addition to simulations of Flake, CRLE and Penman-Moteith method, widely used in lake-atmosphere heat flux simulation (Wang et al. 2017; Wang et al. 2015; Xu et al. 2009; Yu et al. 2011), needs validation and evaluation in advance, rather than referring to existing published parameterization schemes over other low-elevation lakes (Xu et al. 2009; Yu et al. 2011).

Table 1.1 Summary of relevant lake studies on the Tibetan Plateau (the current paper is added for completeness). In the Key results column the abovementioned components are identified by the code: (1)quantify lake evaporation and its trend; (2) issues related to energy budget or water balance. Studies do not assess the two components and N/A directly follows the code in such cases.

Study	Method	Lake	Key results
Wang et al. (2017)	EC and Bulk method	Small lake adjacent to Nam Co	(1) Averaged value of 812 mm during its open water period in 2012 and 2013; (2) Estimated energy budget closure value of 0.97;
Lazhu et al. (2016)	Flake model	Nam Co	(1) Averaged annual value of 832 ± 69 mm during 1980-2014; and an un-significant increasing trend was reported; (2) The change of evaporation has suppressed the recent expansion of Nam Co;
Ma et al. (2016)	CRLE	Nam Co	(1) Averaged annual value of 635 mm during 1979-2012; and a slight decreasing trend was reported; (2) The decreasing trend of evaporation is responsible for about 4% of the recent rapid expansion of Nam Co;
Zhou et al. (2013a)	Pan observation	Nam Co	(1) Around 600 mm during May to October in 2007-2011; (2) Subsurface water seepage exist in this area;
Zhu et al. (2010)	Penman-Monteith model	Nam Co	(1) Average annual value of 1430 mm during 1971-2004; (2) The supply of water could not complement the need for the evaporation and water volume increasing;
(Zhang et al. 2011a)	Penman-Monteith model	Nam Co	(1) Average annual value of 1184 mm during 1976-2009; a decreasing trend was reported; (2) N/A;
Haginoya et al. (2009)	Bulk method	Nam Co	(1) Averaged annual value of 658 mm during 2006-2008; (2) N/A;
Li et al. (2016)	EC observation	Qinghai lake	(1) Average annual value of 826 mm during May 2013 to May 2015; (2) N/A;
(Li et al. 2007)	Pan observation	Qinghai lake	(1) Average annual value of 924 mm during 1959-2000; (2) Water balance was primarily influenced by surface runoff and precipitation and less by evaporation and anthropogenic factors;
(Shi et al. 2010)	Pan observation	Qinghai lake	(1)Average annual value of 880 mm during 1958-2004; a decreasing trend was reported; (2) N/A;
(Guo et al. 2016)	EC observation	Serling Co	(1) 417 mm during April 26 to September 26 in 2014; (2) N/A;
Li et al. (2015b)	EC	Ngoring	(1) Averaged value of 436 mm during Jun-Nov in 2011-2012; (2) N/A;
Liu et al. (2014)	EC	Erhai	(1) Annual evaporation of 1165 mm in 2012; (2) N/A;
Yu et al. (2011)	Bulk method	Yamdrok Yum Co	(1) Averaged annual value of 1252 mm during 1961-2005; a decreasing trend of -2.4 mm $year^{-1}$ was reported; (2) N/A;
Xu et al. (2009)	Bulk method	Yamdrok Yum Co	(1) Averaged annual value of 621 mm during 1961-2005; and a decreasing of 7% during warm season (May-Sep) in 1961-2005 was reported; (2) N/A;
(Liu et al. 2009b)	Pan observation	Zigetang and Cuona	(1) Mean evaporation value of around 950 mm; a decrease of annual evaporation since 1990s; (2) Lake growth was related to increase in annual precipitation, runoff and decrease in evaporation;
Li et al. (2001)	Penman method	Zigetang	(1) Average annual value of 925 mm during 1958-1998, and an increasing trend was reported;

			(2) N/A;
(Morrill 2004)	1-dimensional lake energy balance model	Ahung Co	(1) Annual value of about 760 mm during 1986-2001; (2) Precipitation play significant role in overall water balance while the influence from evaporation is small;
Chapter 4	EC and Bulk method	Nam Co and an adjacent small lake	(1) Annual evaporation value of about 981 ± 18 mm during open water period of 2016; Significant differences exist in evaporations of the "small lake" and the "large lake"; (2) Energy budget closure value is 0.859 during observational periods of July to November;

Due to the significance of lake evaporation in catchment-scale hydrologic processes, water resource management and regional climate modelling, numerous methods for deriving evaporation over wet surfaces have been proposed (Bowen 1926; Brutsaert and Stricker 1979; Dalton 1802; Finch and Calver 2008; Priestley and Taylor 1972; Winter et al. 1995; Yao 2009). These methods mainly include: empirical methods, bulk transfer methods, water budget methods, energy budget methods, combination methods and direct observations (Finch and Calver 2008). The principles and disadvantages of these methods are briefly summarized as follows.

Simple empirical methods, such as Pan evaporation corrected with Pan coefficients, are inadequate for widespread application due to the large uncertainties originating from Pan types, lake properties and difference in environmental and meteorological settings. Other empirical methods relate evaporation to meteorological variables, for example, solar radiation, air temperature, and wind speed (McGuinness and Bordne 1972). Bulk transfer methods originate from Dalton (1802) and relate evaporation to water vapor differences between the water surface and atmosphere, and evaporation is regulated by a wind function and a bulk transfer coefficient, which can be influenced by lake size and depth and local climatic and environmental conditions (Assouline et al. 2008; Oswald and Rouse 2004; Panin et al. 2006). Water budget methods determine evaporation by conservation of inflow, outflow, precipitation, and change in the water level. However, errors inherent in measurements of water budget components, including the difficulty in observing subsurface water exchange, will cause large uncertainties (Finch and Calver 2008). Energy budget methods treat the latent heat flux (LE, with L as the latent heat of vaporization and E as evaporation) as the residual heat of all other energy components, and assume that incoming solar radiation is the principal source of energy for evaporation (McGuinness and Bordne 1972). The Bowen ratio ($Bo = H/LE$, (Bowen 1926)) has been widely used for allocating the ratio of heat loss by conduction to that by evaporation. Combination methods usually combine energy

budget methods and bulk transfer methods by eliminating requirement of water surface temperature. However, the key observations of water temperature for Bo and heat storage in the water (Q_x) are always limited worldwide, especially on the TP. Studies of long-term lake evaporation have been conducted over all types of lakes in different climatic environments all over the world (Yao, 2009), and the Bowen ratio energy budget (BREB) method has been widely chosen as the standard reference method for evaluation of other evaporation methods (Rosenberry et al. 2007; Winter et al. 1995; Yao 2009). In the past several years, direct observation of lake evaporation using an eddy covariance technique has been widely applied, mostly on large lakes of the TP, for analysis of lake-atmosphere interaction processes and evaluation of model simulations (Biermann et al. 2013; Li et al. 2015b; Liu et al. 2014; Wang et al. 2017a; Wang et al. 2015; Wen et al. 2016). However, the adequacy and reliability of the evaporation methods over high-elevation lakes urgently needs evaluation based on the precise EC observations.

1.1.4 Lake's response to climate change

As an important component of the climate system, lakes relative to other underlying surfaces have characteristics of transparent to visible solar radiation, low albedo, small momentum roughness length, high thermal conductivity and large thermal capacity. They can impact atmosphere boundary layer processes in numerical climate modeling and affect local atmosphere circulation and regional heat and water budget (Gerken et al. 2014; Long et al. 2007). Much higher latent heat flux than sensible heat flux exists over the lake surface (Wang et al. 2015; Wen et al. 2016), and thus could yield a lower lifting condensation level and higher boundary layer equivalent potential temperature, which favor convective precipitation (Small and Kurc 2001). Lakes affect overlying atmosphere through lake-air turbulent heat flux, which are not only related to lake surface conditions (surface temperature, waves, water plants etc.), but also influenced by meteorological and environmental backgrounds (warm-dry/cold-moist air, cloud cover, lake area, lake depth, etc.) (Blanken et al. 2003; Li et al. 2015b; Rouse et al. 2005; Wang et al. 2015; Wen et al. 2016).

Under global warming, TP shows dramatically stronger variation of hydrological cycle, in addition to a significant air warming and moistening, solar dimming, wind stilling, glacier melting, permafrost degradation (Yang et al. 2014; Yang et al. 2010). Warming trends of lake surface temperature are reported to be close to the air temperature and the lake surface temperature is showing increasing trend

and decreasing trend in close area (O'Reilly et al. 2015). Thus, how is lakes' response to climate change over the high-elevation lakes over the TP? To answer this question, long term reanalysis data and in-situ observations are needed for model forcing. However, before application of the models to the lakes on the TP, the parameterization schemes and simulation results need a thorough evaluation using in-situ observations, for which we have found that the constants for parameterizing momentum roughness length are different from the values in oceanic research (Wang et al. 2015). Thus, to evaluate lakes' responses and effects to climate change, detailed evaluation of models' performance in this data scant area of the vast high-elevation lake zone show high priority.

1.2 Objectives and scope of this study

To address questions related to vertical heat exchange over lakes and lakes' response to climate change, in-situ observations of eddy covariance, traditional meteorological variables and temperature profile in the water of small Nam Co lake ("small lake" for short hereafter) and Nam Co lake ("large lake" for short hereafter) are carried out since April 2012. The main objective of this thesis is to arrive at a better quantification of vertical heat exchange both at the lake-atmosphere interface and in the water of the "small lake" and the "large lake" in Nam Co basin, Tibetan Plateau. A comprehensive observational dataset including traditional meteorological variables, eddy covariance observations, temperature profile measurements in the water, ITP forcing, as well as satellite data are collected. To understand the processes governing the water and heat exchanges of lakes, Flake modeling was evaluated by in-situ observations and further used for long-term trend analysis. The following research questions are formulated to achieve the objectives:

Q1. What are the characteristics of lake-atmosphere interaction processes in these high-elevation lakes? What are the adequate schemes of roughness lengths for momentum, heat and water to predict their turbulent heat fluxes?

Q2. What are the exact evaporations during the open-water periods of "small lake" and "large lake"? And how are the energy budget of these two water bodies?

Q3. What differences exist in lake-air interaction processes of the "small lake" and the "large lake"? Whether evaporation in small water bodies are suitable for evaluation of that in large water bodies?

Q4. How are lake's responses to climate change? And what are the driving factors behind?

1.3 Thesis outline

The four research questions are addressed in Chapters 3, 4, 5 and 6 of this thesis respectively. The thesis is structured as follows:

Chapter 2 provides a brief introduction of the study area, observational data sets, as well as evaluation metrics;

In **Chapter 3**, based on the in-situ observations in the "small lake", the initial characteristics of lake-atmosphere interaction processes are obtained and the performances of two lake-atmosphere boundary layer methods are evaluated. And the optimized B method could be used for gap filling to construct a continuous data series of turbulent heat flux.

Chapter 4 uses bulk aerodynamic transfer method (Chapter 3) for data interpolation due to inadequate footprint and data qualities; determines the driving forces of lake-atmosphere turbulent heat fluxes and then analyzes the evaporation and energy budget of the "small lake" and "large lake" during their open-water periods;

Chapter 5 compares the differences of seasonal variations of lake-air transfer parameters, meteorological variables and turbulent heat fluxes and quantitatively explains the possible reasons to the existed observed differences, especially the higher evaporation in the "large lake" than in the "small lake";

In **Chapter 6,** the performances of traditional evaporation estimation methods and Flake modeling in the two water bodies are evaluated; and lake's responses to climate change and its driving forces behind are analyzed through long-term trend analysis;

Chapter 7 synthesizes the main findings of Chapters 4, 5, 6 and 7 with respect to the four research questions; and directions for further research are presented as well.

The logic of the thesis structure is shown in Figure 1.1. The in-situ observational data sets provide the data basis for this study. Chapter 3, 4, 5, 6 present the investigation of vertical heat transfer processes of the two water bodies in Nam Co. Particularly, Chapter 3 shows the observed characteristics of lake-atmosphere boundary layer processes, and makes an evaluation of lake-atmosphere interaction methods, which could provide gap-filling method for continuous data

series of lake-air turbulent heat flux. Chapter 4 analyzes the characteristics of both the evaporation and the energy budget of the two water bodies during their open-water periods. Chapter 5 analyzes the differences of boundary layer physics and evaporations existing in these two water bodies. Chapter 6 validates all kinds of methods for modeling lake-atmosphere water and heat transfer (including traditional evaporation estimation methods and Flake modeling) and quantitatively analyzes the lake's response to climate change and its driving forces behind. Subsequently, the findings are summarized in Chapter 7.

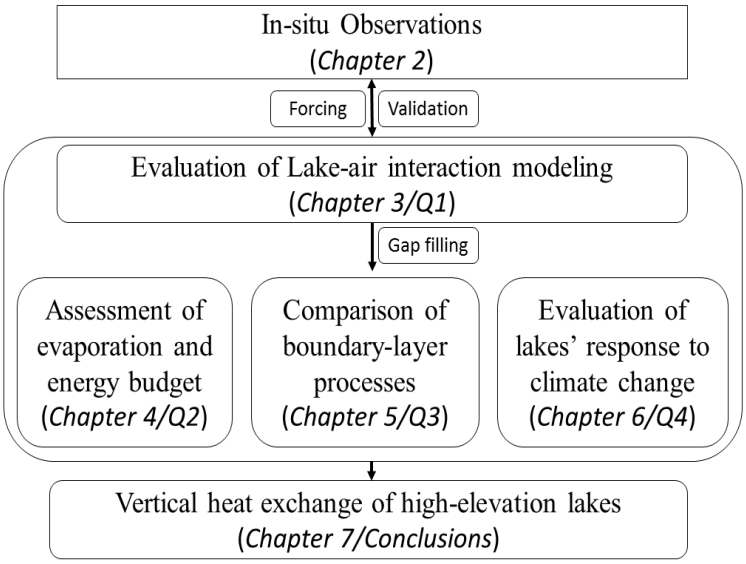

Figure 1.1 Diagram and logic of the thesis structure. Four research questions (Q1-Q4) are answered in Chapters 3-6.

Chapter 2 In-situ datasets and methods

2.1 The target lakes in Nam Co basin

Being considered as Asia's water tower and consisting of more than 1200 lakes larger than 1 km^2 in surface area and tens of thousands of small lakes (Zhang et al. 2014), TP with an average elevation of about 4000 m above sea level forms the largest high-elevation inland lake zone (Ma et al. 2011; Zhang et al. 2014). The water resources, hydrological cycle and ecological change over the TP have attracted significant attention for scientific research based on the limited field measurements (Immerzeel et al. 2010; Oku et al. 2006; Singh and Nakamura 2009; Wei et al. 2012; Yang et al. 2014).

Nam Co lake basin with an area of 10610 km^2 lies in a transition region of semi-arid and semi-humid climatic zone in the central TP and its climate can be influenced both by westerlies and South Asia summer monsoon. The dominant land cover is a homogeneous ecotone composed of alpine meadows and steppe grasses, with mixed vegetation including Kobresia macrantha and Stipa purpurea (Miehe et al. 2011; Wei et al. 2012). The Nyainqentanglha Mountains (glacier-capped mountains with an altitude ranging from approximately 5300 m to 6400 m a.s.l.) form the south edge of the lake basin. The land-lake breeze circulation in the area of Nam Co lake and the Nyainqentanglha Mountains displays obvious diurnal variations (Biermann et al. 2013; Gerken et al. 2014; Zhou et al. 2011). The wind mostly blows from the lake area during the day and from the land at night. Since 2005, the first meteorological and hydrological station (Ma et al. 2009), Nam-Co Monitoring and Research Station for the Alpine Environment (Nam-Co station, black circle in Figure 2.1b1), was set up and it has provided enormous data for research in this catchment. The annual mean air temperature is approximately 0 °C, and the annual mean wind speed is approximately 4.04 m s^{-1} based on Planetary Boundary Layer (PBL) tower measurements of 2 m high on land taken from 2007 to 2012 in the Nam-Co station. Precipitation mainly occurs during the monsoon period (May to October), and the multiyear average (from 2007 to 2011) is approximately 505mm (Zhou et al. 2013).

The target lakes contain adjacent two lakes: the Nam Co lake ($90°15' - 91°03'\mathrm{E}, 30°29' - 30°56'\mathrm{N}$, "large lake", Figure (2.1a)) and the small Nam-Co lake ($90°58'10''\mathrm{E}, 30°46'55''\mathrm{N}$, "small lake", white box '1' in Figure (2.1a) and Figure (2.1b1)). The "large lake" is the third largest lake on the TP, with a surface elevation of approximately 4715 m a.s.l., an area of more than 2000 km^2 and a

maximum depth of larger than 90 m (Wang et al. 2009). The "small lake", with an area of 1.4 km^2 and a maximum depth of about 14 m, is located to the southeast direction of the "large lake". The distance of the land between the two lakes are only about 500 m. According to field observation experiences, the start dates of ice-formation in the "small lake" and the "large lake" are around mid-November and beginning of January respectively while the dates of ice-melt are around beginning of April and beginning of May respectively.

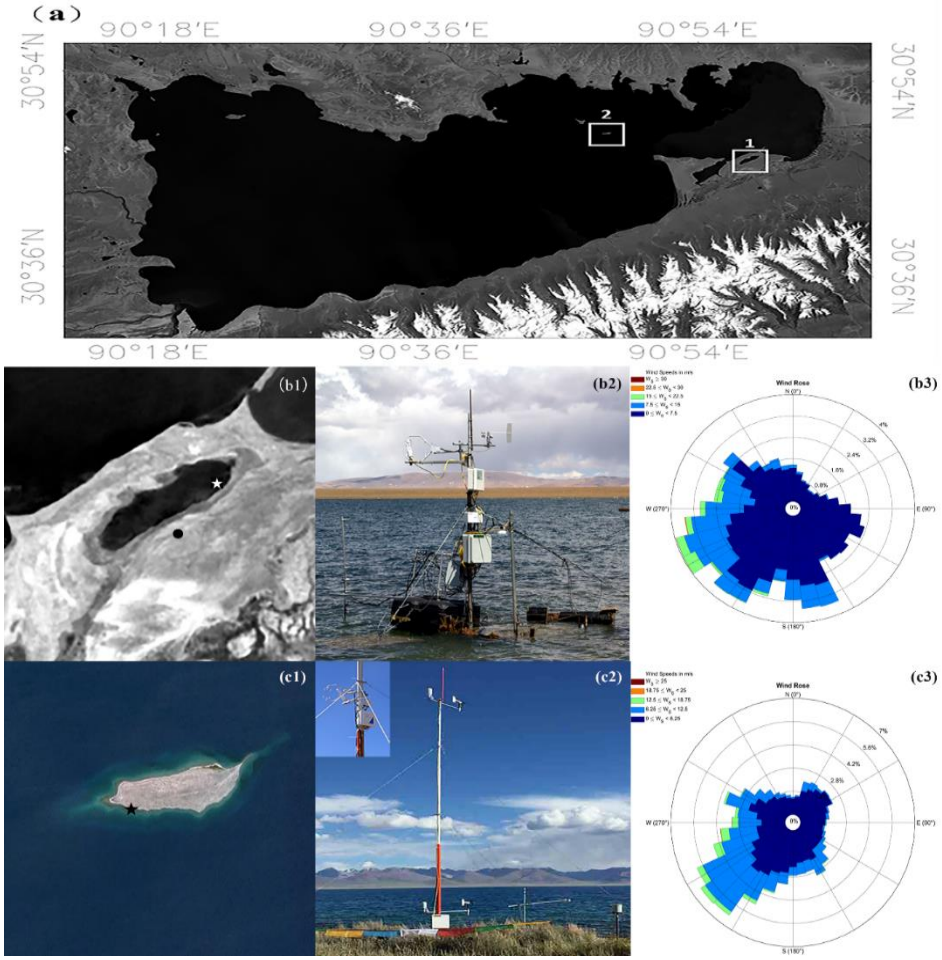

Figure 2.1 (a) The positions of observation sites of the "small lake" (white box '1') and of the "large lake" (white box '2') in the Nam-Co basin; (b1) the enlarged view of the "small lake" area; the white pentagram shows the position of the measurements in the "small lake" while the black circle shows the position of "Nam-Co station"; (b2) the photo of the instruments; (b3) the wind rose in the "small lake" area; (c1) the enlarged view of the "large lake" area; The black pentagram indicates the position of the measurements on the island of the "large lake"; (c2) the photo of the instruments; (c3) the wind rose in the "large lake" area.

2.2 Observational dataset

2.2.1 In-situ observations in two lakes

The "small lake" is situated to southeast of the "large lake" and stretches from northeast to southwest and measures approximately 2620 m by 510 m in size with a generally rectangular shape. After the short-term lake-air interaction experiment with an EC system in 2010 (Biermann et al. 2013), we set up an energy balance system in the "small lake" for long-term measurements of evaporation and energy budget analysis. The lake eddy covariance (EC) observation system (Figure (2.1b1)) is situated 8 m off shore and approximately 500 m from the northern shore and the water depth around the lake EC system is approximately 1.5 m. The lake EC system (Figure (2.1b2)) includes a three-dimensional sonic anemometer (CSAT3, Campbell Scientific, Inc.) and an open-path CO_2/H_2O infrared gas analyser (LI-7500A, LI-COR Biosciences), which are installed approximately 2.7 m above the water surface. The CSAT3 faces west and the LI-7500A is situated 25 cm south of the CSAT3. Three components of wind velocity, air temperature, air humidity, air pressure, and CO_2 were observed at a frequency of 10 Hz by CAST3 and LI-7500A. A radiation sensor (CNR4, Kipp & Zonen) at a height of 1.5 m provided measurements of downward shortwave radiation ($R_{s\downarrow}$), downward longwave radiation ($R_{l\downarrow}$), upward shortwave radiation ($R_{s\uparrow}$) and upward longwave radiation ($R_{l\uparrow}$). Observations of eddy covariance and the radiation budget were recorded by a data logger (CR5000) every half-hour. Three fixed lake water temperature sensors were installed (Pt100, at 5 cm, 10 cm, and 20 cm), avoiding direct exposure to sunlight. In addition, six water temperature sensors were set from the water surface to a depth of 60 cm, and the one close to the water surface was used as the water surface temperature (T_s) considering the influences of waves and lake level variations. Due to the freezing and thawing processes, the temperature sensors in the water were all destroyed in April 2013. Because of the importance of surface water temperature changes caused by surface warming and cooling (Fairall et al. 1996c), one temperature sensor in the air was used to measure the T_s of the water in the "small lake". Except for that, the temperature profiles did not function during May 16th to July 6th in 2012. Thus, considering the wave effects, lake level variations (less than 20 cm), and strong mixing in the water surface layer, two representative temperatures, one close to the water surface and one at a depth of 60 cm, are chosen to represent the shallow mixing layer and "deep layer", with thicknesses of 0.3 m and 0.7 m, respectively. Lake level variations were observed at a 10-minute resolution using

a water level gauge in the "small lake". All the instruments are fixed onto concrete platforms in the water.

The observation site in the "large lake" is situated on the island (an area of about 0.18 km^2, white box '2' in Figure (2.1a) and Figure (2.1c1)). The instruments are setup at the southwest of the island and include the following observations: (1) on July 28th 2015, automatic weather station (AWS, Figure (2.1c2)) was established on the island and is about 10 m far from the shore. The meteorological variables consist of two layers of air temperature, air humidity, wind speed and wind direction at heights of 1.52 m and 9.52 m above the land surface. Besides, air pressure, precipitation and four components radiation are also observed. The AWS system is sampled by a data logger of CR1000 at 10 minutes and is powered by 12 volts battery and charged by solar panels. (2) On July 7th 2016, EC observation system (insert in upper left of Figure (2.1c2), facing south) is added in the middle of the AWS tower at a height of 4.5 m above the island surface (another 1.5 m above the water surface). Temperature, humidity, CO_2 and three-dimension wind speeds are measured at a frequency of 10 Hz by gas analyzer (Li-7500A, LI-COR Biosciences) and ultrasonic anemometer (CSAT3, Campbell Scientific, Inc.) and the data are collected by a second CR1000. (3) Water temperature gradients to a depth of 40 m (90.7979 E, 30.8107 N) are installed during July 28th to November 19th in 2015 and during July 7th to November 18th in 2016, respectively. The temperature sensors are distributed at 10 depths (0.5 m, 1.5 m, 3 m, 6 m, 10 m, 15 m, 20 m, 25 m, 30 m, 35 m) and are affixed to a floating buoy weighted to the lake bottom. The sensor at a depth of 30 m was damaged in 2016. The temperature measurements at 0.5 m depth is chosen as water surface temperature (T_s or T_0, ℃). Moreover, variations in the water level of Nam Co lake were measured manually each day during the open-water periods of 2012 and 2013. Specification of the stations in the "small lake" and the "large lake" are summarized in Table (2.1).

Table 2.1 Specifications of the field observations in the "small lake" and the "large lake"

Instruments	The "small lake" (Figure (2.1b))	The "large lake" (Figure (2.1c))
Ultrasonic anemometer	CSAT3 (Campbell Scientific, Inc.); 2.7 m above the water surface and face west; April 2012 –October 2014;	CSAT3 (Campbell Scientific, Inc.), about 6 m above the water surface and face south; July 2016 – July 2018
Open path CO_2/H_2O analyzer	Li-7500A (LI-COR Biosciences), 2.7 m above the water surface and 25 cm south of the CSAT3; April 2012 – October 2014;	Li-7550 (LI-COR Biosciences), 6 m above the water surface and 20 cm west of the CSAT3; July 2016 – July 2018
Water temperature	Depths of 0.05 m, 0.1 m, 0.15 m, 0.3 m, 0.6 m; April 2012 – November 2013;	HOBO water temperature Pro v2 Data Logger 021001, at depths of 0.5m, 1.5m, 3m, 6m, 10m, 15m, 20m, 25m, 30m, 35m; August 2015 – November 2015 and July 2016 – November 2016;
Net radiometer	CNR1 (Kipp & Zonen), 1.5 m above the water surface; April 2012 – November 2013;	CNR1 (Kipp & Zonen), 1.5 m above the land surface; August 2015 – Now;
Water level	10 minutes interval; April 2012 – November 2013;	Manual observation, daily interval;
Air temperature and humidity	----	HMP 155A (Vaisala), 1.52 m and 9.52 m above the land surface; August 2015 – Now;
Wind speed and direction	----	RM Young wind Monitor, 1.52 m and 9.52 m above the land surface; August 2015 – Now;
Rain gauge	----	Tipping bucket; August 2015 – Now;

2.2.2 Observations in Nam Co station

Since September 2005, the Nam Co Monitoring and Research Station for the Alpine Environment (black circle in Figure (2.1b1)) has operated a PBL tower, an EC system, and a four-component radiation sensor over the grassland for monitoring climatic, meteorological and environmental changes in the lake basin (Ma et al. 2014). The PBL tower system includes observation sensors of air temperature, air humidity, wind speed at five layers (1.5 m, 2 m, 4 m, 10 m, and 20 m) and wind direction at 3 layers (1.5 m, 2 m and 20 m), with all sensor types of Vaisala; and soil temperature and soil moisture at five depths (0 cm, 10 cm, 20 cm, 40 cm, 80 cm, 160 cm) under the ground; and air pressure and global solar radiation near the land surface. Three terraces exist from the level of the observation site in the "small lake" (white pentagram in Figure (2.1b1)) to the Nam Co station, spanning a distance of 900 m and an average slope of 8° (Biermann et al. 2013). Close to the PBL tower in the Nam Co station, EC observational system and radiation sensors are set up over the grass land. The characteristics of water, heat and CO_2 transfer between the grass land and atmosphere have been researched during the previous TP energy and water cycle

experiments of GAME/Tibet and CAMP/Tibet (Ma et al. 2002; Ma et al. 2006; Ma et al. 2004; Tanaka et al. 2001; Tanaka et al. 2003; Yang et al. 2008). Measurements in Nam Co station include precipitation and additional meteorological data, and it can provide us a supplemental data for continuous meteorological observations in the Nam Co lake basin.

2.2.3 Satellite and reanalysis data

MODIS (Moderate Resolution Image Spectro-radiometer) multispectral sensor on board National Aerodynamic and Space Administration's (NASA) Earth Observation System's (EOS) Terra and Aqua satellites monitor the earth's solar radiation, atmosphere, ocean and land continuously at an orbit of 705 km since December 1999 and May 2012 respectively. MODIS contains 36 spectral bands, spanning from visible light (0.4 μm) to thermal infrared (14.4 μm). Various types of standard MODIS land, atmosphere, and ocean products (including land surface temperature (LST), land cover, precipitable water vapor, cloud top temperature, total ozone etc.) have been created by NASA and Unites States Geological Survey (USGS). MODIS LST products (MOD11A1 and MYD11A1) including land surface temperature and land surface emissivity at a spatial resolution of 1 km are used in this study.

A high spatial resolution (0.1°) forcing dataset covering China was produced by Institute of Tibetan Plateau research (hereafter ITP forcing) by merging a variety of data sources (He and Yang, 2011). The ITP forcing data mainly includes observations (wind speed, air temperature, relative humidity, sunshine duration, precipitation and air pressure) from in-situ sites organized by China Meteorological Administration (CMA); TRMM (Tropical Rainfall Measuring Mission) precipitation data; downward shortwave radiation from GLDAS (Global Land Data Assimilation Systems); Princeton forcing data (including wind speed, air temperature, relative humidity and surface pressure). The temporal resolution of ITP forcing is 3 hour, spanning from 1979 to 2016. This dataset has been widely used as forcing data in climate change studies over the TP (Huang et al. 2017; Ma et al. 2016; Wang et al. 2018).

2.3 Preprocessing of EC data

The EC method for high-frequency sample data was chosen to determine heat, water vapor, and momentum flux. The "Turbulence Knight 3" (TK3) software package developed by Bayreuth University was used to process the turbulence data (Mauder and Thomas 2015) (https://zenodo.org/record/20349#). The

processing includes time lag compensation, spike removal, planar fit coordinate rotation (Wilczak et al. 2000), spectral correction (Foken et al. 2004), conversion of buoyancy into sensible heat, and correction for density fluctuations (Webb correction) to determine the flux of scalar quantities such as H_2O (Foken et al. 2004; Webb et al. 1980). Moreover, planar fit rotation, including data only from the direction of the lake, is performed to correct for the influence of the terrain structure of the bank (Biermann et al. 2013). Values of sensible heat flux (*H*), latent heat flux (*LE*), and friction velocity were produced at half-hourly intervals, together with data quality indicators 1 – 9 (1 indicates high quality, 9 low quality) (Foken et al. 2004). Footprint analysis (Göckede et al. 2004) was used to identify observations collected when lake surface was the dominant source area. Biermann et al. [2013] showed that the observed turbulent heat flux for conditions with wind direction from the lake can represent the land surface type of "water surface". We selected the turbulent flux data from specific wind sectors (wind direction >240° and wind direction <40°, with north at 0° and the azimuth increasing clockwise) as lake measurements in the "small lake".

Standard turbulent heat flux processes by TK3 software mentioned above are also performed for EC observations in the "large lake". In order to ensure data qualities of EC observations, the following criteria are also considered: (1) data quality flags (1-9, 1 indicates highest quality, 9 indicates low quality) considering the "steady state test" and the "integral turbulence characteristics test" are used for high-quality heat flux selection. More accurately, turbulent heat flux with quality flags larger than 3 are discarded. (2) Similar to the footprint analysis in the "small lake" (Wang et al. 2015), turbulent heat flux of the "large lake" from wind directions ($\mathrm{WD} < 135° \,\&\, \mathrm{WD} > 270°$, with north as 0° and the azimuth increasing clockwise) contaminated by land are discarded, and the remained turbulent flux have upstream fetches of more than 30 km and water depths of larger than 90 m. (3) The impact of internal boundary layers caused by discontinuities of surface properties are also checked. The following fetch-height relation was used to roughly estimate the height of the new equilibrium layer (δ): $z \leq \delta = 0.3\sqrt{x}$, where x is the fetch (m) and z is the height (m) of sensor. Thus, the internal boundary layer height caused by land is only about 1 m, which is much lower than the height of sensors. (4) Due to the strong influence of local free convection on turbulence at small wind speed, the turbulent heat flux at small wind ranges ($U_z < 3$ m s^{-1}) are also ignored in boundary layer parameters estimation. This criteria through U_z will also guarantee a fully mixed surface layer and justify T_s substituted by water temperature at 0.5 m depth. After all

these quality controls, the EC observations could represent lake-atmosphere interaction of the "large lake" and the valid data percentages are 54.8% with only wind direction criteria, 82.3% with only quality criteria, 83.8% with wind speed criteria and 42.4% with criteria of wind speed, wind direction and data quality.

2.4 Assessment metrics

Models are used to simulate processes of lake-atmosphere interaction processes and internal mixing. The performances of these models can be tested and ranked based on the root mean square error (RMSE), Pearson correlation coefficient (R), relative error (RE) and mean bias (MB) between simulated results and eddy covariance observations. Smaller values of RMSE, RE and MB and higher values of R indicate better performance of a method. The equations for obtaining these statistical measures are as follows

$$RMSE = \sqrt{\frac{\sum_{i=1}^{n}|S_i - O_i|}{n}} \tag{2.1}$$

$$RE = \frac{1}{n}\sum_{i=1}^{n}\left|\frac{S_i - O_i}{O_i}\right| \tag{2.2}$$

$$MB = \frac{1}{n}\sum_{i=1}^{n}(S_i - O_i) \tag{2.3}$$

Where S_i are the simulated results, O_i are the observed results, and n is the number of observations.

To describe the similarity of variations between environmental variables and H & LE in Chapter 4, the Fréchet distance (Alt and Godau 1995) and root mean squared error (RMSE) are used to measure differences among selected pairs of normalized variables. All the variables (including H, LE, $U_z\Delta T$, $U_z\Delta E$, U_z, ΔT, ΔE, ζ, R_n) are normalized to the range [0 1] using the largest and smallest values from time series representing half-hourly, daily and monthly data. The normalization equation is $Out_i = \frac{In_i - In_{min}}{In_{max}}$, where In is the original dataset and Out is the normalized dataset, where In_{min} is the minimum, In_{max} is the maximum, In_i is a specific value at position i for half-hourly, daily, or monthly data series. A small Fréchet distance or low RMSE value indicate high similarity between two curves.

Chapter 3 Evaluation of lake-air interaction modeling

3.1 Introduction

A few studies have used eddy covariance (EC) observations to examine the high-elevation lakes of the TP. For example, Biermann et al. (2013) analyzed differences in water and heat flux transport between water and grassland by combining footprint analysis with short-term EC observations on the shoreline of the "small lake". Liu et al. (2014) analyzed the heat and water exchange coefficients (i.e., roughness lengths and bulk transfer coefficients) over Lake Erhai (1978 m a.s.l.) on the southeast edge of the TP. And Li et al. (2015b) reported a persistently unstable atmosphere over the Lake Ngoring (4274 m a.s.l.) on the eastern plateau.

To better understand heat and water vapor exchange and to find the appropriate modeling approach for high-elevation lakes on the TP, we employs two popular lake-air heat and water exchange methods of different complexity, the widely used Bulk aerodynamic transfer method (Fairall et al. 1996a; Verburg and Antenucci 2010) and the experiment-based multilayer method (Foken 1979, 1984), hereafter referred to as the B method and M method, respectively. The two methods have different structures and theories of representing turbulent diffusion over the water surface of a lake. In the B method, sensible heat flux (*H*), latent heat flux (*LE*) and wind stress are related to traditional meteorological observations (such as wind speed, water temperature, air temperature, and air humidity) through bulk transfer coefficients, which can be parameterized using the roughness lengths for momentum, heat, and water vapor (Beljaars and Holtslag 1991; Brutsaert 1999; Fairall et al. 1996b; Katsaros 1998; Liu et al. 1979; Pond et al. 1974; Rouse et al. 2003; Smith 1988; Verburg and Antenucci 2010)[*]. In principle, the M method describes much better heat and vapor transfer, since it takes into account contributions from different planetary boundary layer (PBL) sublayers: the molecular layer, buffer layer, and turbulent layer (Foken 1984). For each layer, various atmospheric stratification exchange coefficients and

[*] **This Chapter is based on the paper:** Wang. B., Y. Ma, X. Chen, W. Ma, Z. Su, and M. Menenti, (2015) Observation and simulation of lake-air heat and water transfer processes in a high-altitude shallow lake on the Tibetan Plateau, J. Geophys. Res. Atmos., 2015, 12,327-12,344, doi:10.1002/2015JD023863.

experimental constants are used (Foken 1979, 1984; Foken and Skeib 1983; Mangarella et al. 1973; Merlivat and Coantic 1975; Panin et al. 2006).

The roughness length for momentum is a basic and fundamental parameter in lake-air heat flux modeling. It is highly variable with different water surface conditions, and scientists have attempted to quantify it by taking into account field information on wave height, wave length, and wave age (Ataktürk and Katsaros 1999; Charnock 1955; Donelan et al. 1993; Fairall et al. 1996a; Gao et al. 2009a; Smith et al. 1992). At similar wind and fetch conditions, waves generated in shallow water have a smaller wave height and a shorter wave length than in deep water (Whalin et al. 1984). The effective roughness length for momentum increases with wave height and decreases with wave length (Menenti and Ritchie 1994; Taylor et al. 1989). It has been reported that roughness length for momentum is higher for coastal water than open sea water (Gao et al. 2009a). Panin and Foken (2005) described a correction on heat flux transfer to take into account the dependence of wave height on water depth, see also Panin et al. (2006).

Another feature relevant to the thermal stratification of lake water is salinity, which is 1198 mg L^{-1} in the "large lake" (Wang et al. 2009). Assuming the salinity in the "small lake" is similar or higher, a water density gradient may be established like in a solar pond (Hull 1979), which reduces mixing in the water and increases the surface water temperature. Because of the higher temperature in the surface water layer, higher air specific humidity close to the water surface is likely to occur. Due to higher air temperature and humidity at the water-air interface, free convective conditions (FCCs) (Zhou et al. 2011), i.e., when buoyancy is dominant over shear, are likely to occur. In this study, we use the term FCCs to refer to the occurrence of free convection in the surface layer.

3.2 Materials and methods

3.2.1 Bulk aerodynamic transfer method

The modeled values for *H* and *LE* are linearly proportional to the stability-dependent bulk transfer coefficients, and they are also affected by wind velocity and the gradients of temperature and humidity between water and atmosphere, respectively (Verburg and Antenucci 2010; Vickers and Mahrt 2010; Vincent 2008). *H* and *LE* then can be expressed as follows:

$$H = \rho_a c_p C_H U_z (T_0 - T) \tag{3.1}$$

$$LE = \rho_a L_v C_E U_z (q_0 - q) \tag{3.2}$$

where ρ_a is the air density ($\mathrm{kg\,m^{-3}}$); c_p is the specific heat of air (1005 $\mathrm{J\,kg^{-1}\,K^{-1}}$); L_v is the latent heat of vaporization ($\mathrm{J\,kg^{-1}}$); U_z ($\mathrm{m\,s^{-1}}$) is the wind speed at the reference height (2.7 m); T (K) and q ($\mathrm{kg\,kg^{-1}}$) are the temperature and specific humidity at the reference height, and T_0 (K) and q_0 ($\mathrm{kg\,kg^{-1}}$) are the same quantities at the water surface; C_H and C_E are the bulk transfer coefficients for heat and water, respectively. In oceanic research, the roughness lengths for heat and water (z_{0h} and z_{0q}) are assumed to be the same (Zeng et al. 1998). Thus, the B method used in this study assumes that C_H and C_E are equal and given by the following equation:

$$C_H = C_E = k^2 \Big/ \left\{ \left[\ln\left(\frac{z_m}{z_{0m}}\right) - \psi_M \right] \left[\ln\left(\frac{z_m}{z_{0h}}\right) - \psi_H \right] \right\} \tag{3.3}$$

where k = 0.4 is the von Kármán constant; z_m (m) is the observational height; and ψ_M and ψ_H are atmospheric stability correction functions for momentum and heat/water vapor, respectively, with different forms in stable (Dyer 1967) and unstable (Businger et al. 1971) atmospheric conditions. These functions are related to the stability parameter ($\zeta = z_m/L$), where L is the Monin-Obukhov length given by eq. (3.4). The roughness length for momentum (z_{0m}) is expressed as a combination of smooth flow ($R_r \frac{v}{u_*}$) and rough flow ($\alpha \frac{u_*^2}{g}$) (Fairall et al. 1996b) by eq. (3.5); and z_{0h} is related to the roughness Reynolds number and was defined as eq. (3.6) by Zeng et al. (1998). Where T_V is the virtual air temperature (K); g is the gravitational acceleration ($\mathrm{m\,s^{-2}}$); α is the Charnock number, which depends on wave-field conditions and the observational environment; the roughness Reynolds number for smooth flow is related to the viscous shear in sea dynamic roughness length parameterizations (Fairall et al. 1996b); v is the kinematic viscosity of air ($\mathrm{m^2\,s^{-1}}$) (Massman 1999); u_* is the friction velocity; and Re can be expressed as follows: $Re = u_* \frac{z_{0m}}{v}$.

$$L = \frac{-\rho_a u_*^3 T_V}{kg\left(\frac{H}{C_p} + 0.61\frac{T \times LE}{L_v}\right)} \tag{3.4}$$

$$z_{0m} = \alpha \frac{u_*^2}{g} + R_r \frac{v}{u_*} \tag{3.5}$$

$$z_{0h} = z_{0m} \exp(-2.67 Re^{0.25} + 2.57) \tag{3.6}$$

3.2.2 Multi-Layer Method

The transformed universal energy exchange formula for near-surface layers of the atmosphere (Foken 1984) can be expressed as follows:

$$X(z) - X(0) = \overline{X'w'} \int_0^z \frac{f(\frac{z}{L})dz}{v_t + v_m} \tag{3.7}$$

Where X denotes the wind velocity for momentum, the temperature for heat, or the specific humidity for water vapor with the observational heights defined by "z" and "0" in the parentheses; w' is the fluctuation in the vertical wind component; v_t is the turbulent exchange coefficient, which can be expressed as $v_t = kzu_*$ (Foken 1984; Monin and Yaglom 1965); and v_m is the molecular exchange coefficient, referred to as the kinematic viscosity of air. The inverse of the integral term in eq. (3.8) is the so-called profile coefficient Γ (Foken 1979, 1984; Panin et al. 2006), and it can be expressed in four-layer integration as follows:

$$\Gamma = (\int_0^{\delta} \frac{dz}{v_m} + \int_{\delta}^{\delta_z} \frac{dz}{v_m + v_t} + \int_{\delta_z}^{\delta_D} \frac{dz}{v_t} + \int_{\delta_D}^{z_m} \frac{\Phi(\frac{z_m}{L})dz}{v_t})^{-1} \tag{3.8}$$

The profile coefficient divides the atmosphere into four layers: a molecular boundary layer, a buffer layer, a turbulent layer without stability correction, and a turbulent layer with the stability corrective function $\Phi(\frac{z_m}{L})$. This profile coefficient is related only to the thicknesses of the molecular boundary layer (δ), the buffer layer (δ_z), and the dynamical sublayer (δ_D), as well as z_m, u_*, and L. More details about δ, δ_z, and δ_D can be found in Foken (1984). Finally, the integral formulas for unstable, neutral, and stable atmospheres can be given, respectively, as follows:

$$\Gamma = \frac{ku_*}{[\frac{v_m}{v_{Xm}}a_1 \times k + 4k + ln\frac{\zeta_c L u_*}{20v} + \frac{1}{n}(1 - \frac{z_m}{L \times \zeta_{c1}})^{-n}]} \quad \text{for } \zeta \leq -0.075 \tag{3.9}$$

$$\Gamma = \frac{ku_*}{[\frac{v_m}{v_{Xm}}a_1 \times k + 4k + ln\frac{\zeta_c L u_*}{20v} + ln\frac{z_m}{L \times \zeta_c}]} \quad \text{for } -0.075 \leq \zeta \leq 0.16 \tag{3.10}$$

$$\Gamma = \frac{ku_*}{[\frac{v_m}{v_{Xm}}a_1 \times k + 4k + ln\frac{\zeta_c L u_*}{20v} + \frac{1}{m}(1 - \frac{z_m}{L \times \zeta_{c2}})^{-m}]} \quad \text{for } \zeta \geq 0.16 \tag{3.11}$$

where $\frac{v_m}{v_{Xm}}$ = Pr (the Prandtl number), $\zeta_c = \frac{\delta_D}{L}$, $a_1 = 6$, n = 0.5, m = -2, $\zeta_{c1} = -0.075$, and ζ_{c2} = 0.16. As the simulated heat flux is usually underestimated in the M method for small lakes (Panin et al. 2006), we selected the smallest δ_D by setting $\zeta_c = \zeta_{c1}$ for unstable conditions, $\zeta_c = \zeta_{c2}$ for stable conditions, and $L \times \zeta_c$ = max($|L \times \zeta_{c1}|$, $|L \times \zeta_{c2}|$) for neutral conditions. After derivation of the profile coefficient Γ, H and LE can be obtained using eq. (3.12) and eq. (3.13)

$$H = \rho_a c_p \Gamma U_z (T_0 - T) \tag{3.12}$$

$$LE = \rho_a L_v \Gamma U_z (q_0 - q) \tag{3.13}$$

3.2.3 Obtaining FCCs and roughness lengths

FCCs, which can be triggered by the appearance of clouds and changes in wind direction during the diurnal thermally forced land-lake breeze circulation, occurred over nearly 40% of the observational period at the Nam Co station (Zhou et al. 2011). These FCCs correspond to high buoyancy flux, strongly reduced wind speed, and an extremely unstable atmosphere. These characteristics of FCCs lead to higher values of the bulk transfer coefficients in eq. (3.1) and eq. (3.2). For the half-hourly data in our research, we used both $z_m/L < -0.3$ and $U_z < 3\ m\ s^{-1}$ to represent conditions influenced by the FCCs.

The roughness lengths are important parameters for parameterization of bulk transfer coefficients in heat flux modeling of the water surface. These values can be obtained through large amounts of observational data under both neutral and non-neutral atmospheric conditions, and the optimal values of roughness lengths should correspond to the peak of its frequency distribution (Yang et al. 2002; Yang et al. 2008). Although this method does not give an exact value for the water surface subject to wave fields and variable lake environments, it can be used to calculate z_{0m}, z_{0h}, and z_{0q} by predicting their possible ranges of variation. The equations are as follows (Foken 2008):

$$\ln(z_{0m}) = \ln(z_m) - \psi_M\left(\frac{z_{0m}}{L}, \frac{z_m}{L}\right) - \frac{k u_z}{u_*} \tag{3.14}$$

$$\ln(z_{0h}) = \ln(z_m) - \psi_E\left(\frac{z_{0h}}{L}, \frac{z_m}{L}\right) - \frac{k(T_0 - T)}{T_*} \tag{3.15}$$

$$\ln(z_{0q}) = \ln(z_m) - \psi_E\left(\frac{z_{0q}}{L}, \frac{z_m}{L}\right) - \frac{k(q_0 - q)}{q_*} \tag{3.16}$$

where u_*, T_*, and q_* are the related Monin-Obukhov similarity scaling parameters (Fairall et al. 1996b; Panofsky and Dutton 1984), which can be derived from observational data in the equations $T_* = -H/\rho_a c_p u_*$ and $q_* = -LE/\rho_a L_v u_*$, respectively. The observed roughness lengths for momentum, heat, and water vapor that are used to evaluate the models can be obtained from eq. (3.14) – eq. (3.16).

3.3 The characteristics of lake-air interaction variables

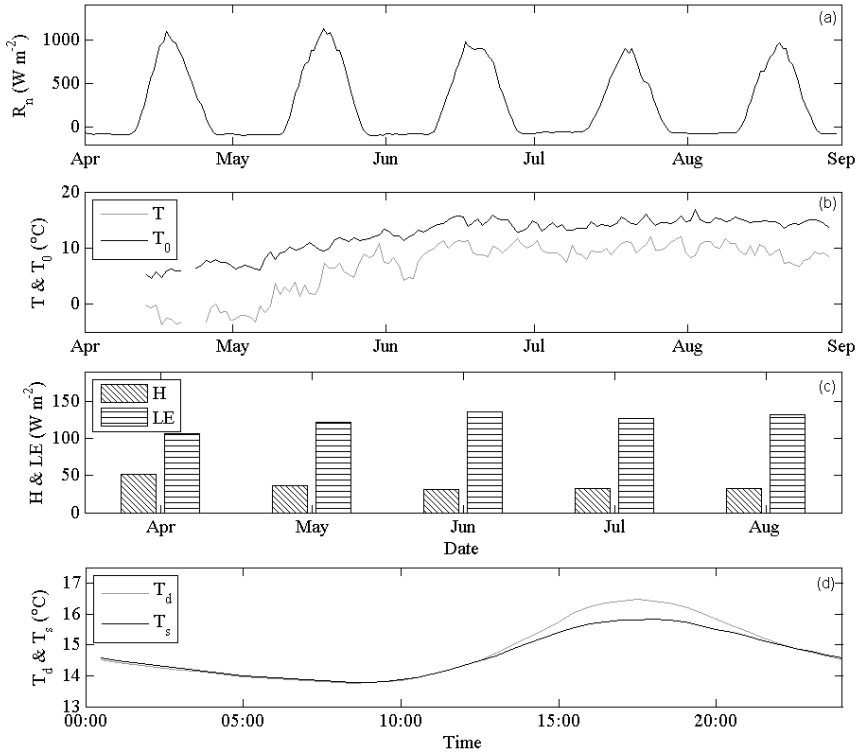

Figure 3.1 Meteorological observations: (a) monthly-averaged diurnal variation of $\boldsymbol{R_n}$; (b) daily-averaged T and $\boldsymbol{T_0}$; (c) monthly averaged H and LE; and (d) diurnal variation of temperature in a deep layer ($\boldsymbol{T_d}$) and a shallow layer ($\boldsymbol{T_s}$) over August in the "small lake".

Because of the low air density and small optical depth of the atmosphere on the TP, very high net radiation (R_n) is observed at the high-elevation "small lake" (Figure (3.1a)). Due to strong solar heating, daily mean water surface temperature (T_0) increased quickly from 4.5°C on 14 April to approximately 15°C on 13 June, while daily mean air temperature (T) rose from -3.8°C to approximately 11°C over the same period (Figure (3.1b)). We note that daily mean T_0 is higher than daily mean T for the whole observational period, and the average water-atmosphere temperature gradient (ΔT) is approximately 5.4 °C. ΔT of the "small lake" is much higher than ΔT of large Lake Ngoring during period of June to August. The temporal variation of ΔT corresponds to a higher H in the beginning of the observational period relative to later in the season (Figure (3.1c)). The LE is much higher than H, and the available energy is primarily consumed by LE. In addition to the large ΔT, there is also very strong wind with an average U_z of 4.8

m s^{-1} and an instantaneous value of over 10 m s^{-1} during the observational period. Moreover, the large average values for ΔT and U_z from the observational data suggest prevailing unstable and neutral atmospheric conditions in the boundary layer (Croley 1989). Such atmospheric conditions are also observed and confirmed at a larger high-elevation lake (Lake Ngoring) in Li et al. (2015b); they may be related to the higher solar radiation on high-elevation lakes of the TP (Verburg and Antenucci 2010). In addition, the thermal stratification of lake water (Figure (3.2d)) shows a high temperature in the surface layer (T_s, average value of 9 cm and 15 cm) and a low temperature in the deep layer (T_d, 65 cm),which is attributed to the reduced mixing in the shallow and small lake. Generally, assuming there is a larger evaporation than precipitation in the "small lake", the salinity in the "small lake" should increase. Although this process leads to extremely large water temperature gradients (solar pond), the observation in the lake do not support the onset of a solar pond-like situation, which may be due to lower salinity subsurface inflow from the "large lake".

The large observed value for U_z and ΔT indicates strong mechanical dynamic and thermal effects of turbulent generation on the "small lake". Many environmental factors, such as the intensity of turbulent mixing, ΔT, and the water-atmosphere vapor pressure gradient (ΔE) can affect the turbulent exchange of heat and water vapor (Nordbo et al. 2011; Zhang and Liu 2014). It has suggested that H is mostly determined by the product of U_z and ΔT ($U_z \times \Delta T$) (Liu et al. 2009a; Nordbo et al. 2011), while the product of U_z and ΔE ($U_z \times \Delta E$) can best describe *LE* (Blanken et al. 2000; Liu et al. 2009a; Nordbo et al. 2011). As shown in Figure (3.2), $U_z \times \Delta T$ and $U_z \times \Delta E$ are most highly correlated ($U_z \times \Delta T$, R = 0.85; $U_z \times \Delta E$, R = 0.83) of all the factors. These high-correlation coefficients imply that both the B method and the M method are suitable for modeling water and heat flux with the differences between C_H&C_E and Γ. It is remarkable that U_z shows a much higher-correlation coefficient (R = 0.66) than ΔE (R = 0.38) for *LE* and has the same value (R = 0.62) as the correlation between ΔT (R = 0.62) and *H*. Respectively, 14.4% and 38.4% of the variability in *LE* and *H* can be explained by ΔE and ΔT, while U_z alone explains 43.6% and 38.4% of the variability. The correlation between *H*, *LE*, and U_z on a half-hourly time scale is similar to the results for three small lakes in Canada found by Granger and Hedstrom (2011). However, our results differ from those of other studies, such as the poor correlations for the Great Slave Lake in northwest Canada (Blanken et al. 2000), a small boreal lake in southern Finland (Nordbo et al. 2011), and the large Ross Barnett Reservoir in the U.S. (Zhang and Liu 2014). In a brief

summary, wind speed plays an important role in water and heat transport on the high-elevation "small lake".

To evaluate the combined effect of temperature and humidity on the air density gradient, we have calculated the gradient in virtual temperature, which was on average 6.5 K over the observation period. The large virtual temperature gradient indicates a large air density gradient, which leads to FCCs. The square root fitting, rather than linear fitting, in Figures (3.2b and 3.2c) indicates that indeed FCCs had a significant impact on heat and vapor fluxes at the water-air interface. Linear fitting (Figures (3.2e – 3.2f)) was still adequate for sensible heat flux, possibly due to its small magnitude, especially in the low wind speed range, where *H* is comparable or smaller than instrumental noise. Further evidence is provided later on (see Figure (3.8)).

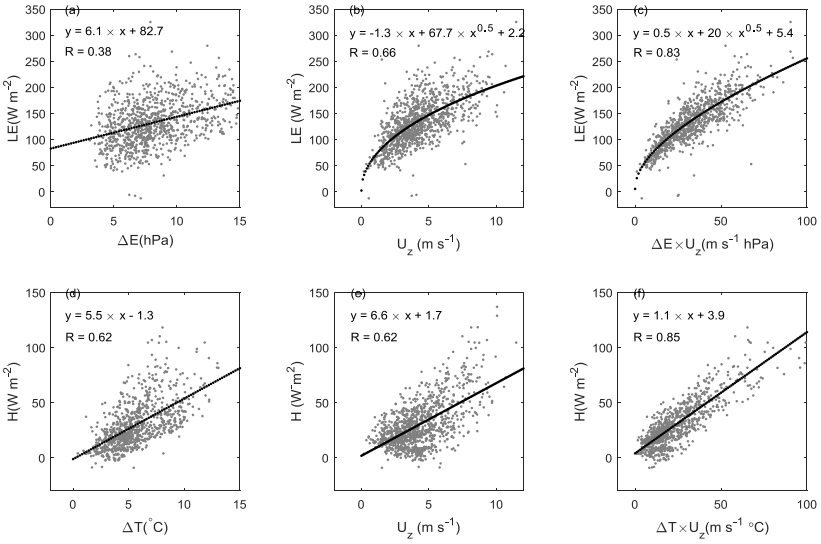

Figure 3.2 Scatterplots between half-hourly (a) *LE* and $\boldsymbol{\Delta E}$; (b) *LE* and $\boldsymbol{U_z}$; (c) *LE* and $\boldsymbol{\Delta E \times U_z}$; (d) *H* and $\boldsymbol{\Delta T}$; (e) *H* and $\boldsymbol{U_z}$; and (f) *H* and $\boldsymbol{\Delta T \times U_z}$. The fitting lines are plotted as dot line with fitting equations and correlation coefficients (R) marked.

3.4 Evaluation of lake-air interaction modeling

3.4.1 Comparison between models and its sensitivity

We compared the simulation results from the B method and the M method. The comparison shows very consistent results, with correlation coefficients of 0.99 for *H*, *LE*, and u_* (Figures (3.3a – 3.3c)). However, the *H* and *LE* simulated by the B method are approximately 10% and 9% higher, respectively, than those

from the M method (Figures (3.3a and 3.3b)). The similarity between the simulated u_*, *H*, and *LE* indicates that the B method (based on flux-profile similarity theory) and the M method (based on experiments and atmospheric stratification theory) are consistent and give similar values when simulating heat flux over the lake water surface.

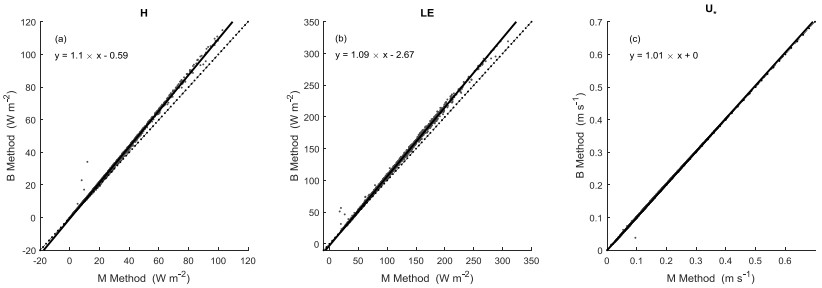

Figure 3.3 Scatterplots of (a) *H*, (b) *LE* and (c) $\boldsymbol{u_*}$ between the B method and the M method; the 1:1 and linear-fitting lines are shown by the dashed and solid lines, respectively, with fitting equations marked.

Roughness lengths are important parameters in turbulent flux modeling. Uncertainty in the roughness length can result in an overestimation or underestimation of the simulated fluxes. We performed a numerical experiment to analyze the sensitivity of turbulent flux simulations to z_{0m} and z_{0h} in the B method. One hundred groups of z_{0m} and z_{0h} (10 increased z_{0m} × 10 increased z_{0h}) were used to calculate the experimental *H*, *LE*, and u_*, with the original z_{0m} and z_{0h} used as reference values. Compared with the reference, the experimental *H*, *LE*, and u_* all increased as a result of the larger z_{0m} and z_{0h} (Figures (3.4c – 3.4e)). As z_{0m} will cause a nonlinear change in z_{0h} based on eq. (3.6), the increased ratio of z_{0h} is expressed as a natural logarithm in Figure (3.4). For example, if both z_{0m} and z_{0h} are multiplied by 6, the experimental z_{0m}, $\ln(z_{0h})$, *H*, *LE*, and u_* will increase, respectively, by factors of 9, 3.38, 1.56, 1.59, and 1.28 compared to the original settings. In contrast, a decrease in z_{0m} and z_{0h}, relative to the reference, will also lead to a decrease in *H*, *LE*, and u_* in the B method simulations (figure is not shown).

A similar experiment was performed for T_0 and T with variations of ±1 K. Variations in T_0 and T may change the sign of ΔT and thus influence the sign of the simulated *H* and *LE*. The simulation results with observed ΔT >2 K were used for the analysis. The results show that increased (decreased) ΔT can increase (decrease) *H* and *LE*, as in Figure (3.5). For example, the experimental *H* and *LE*, relative to the original simulations, increased, respectively, by 13% and 9% when

T_0 increased by 0.4 K and *T* decreased by 0.4 K. Moreover, variations of ±1 K in T_0 and *T* can result in a variation of ± 33% of *H* and ± 21% of *LE*.

3.4.2 Bias in roughness lengths and fluxes

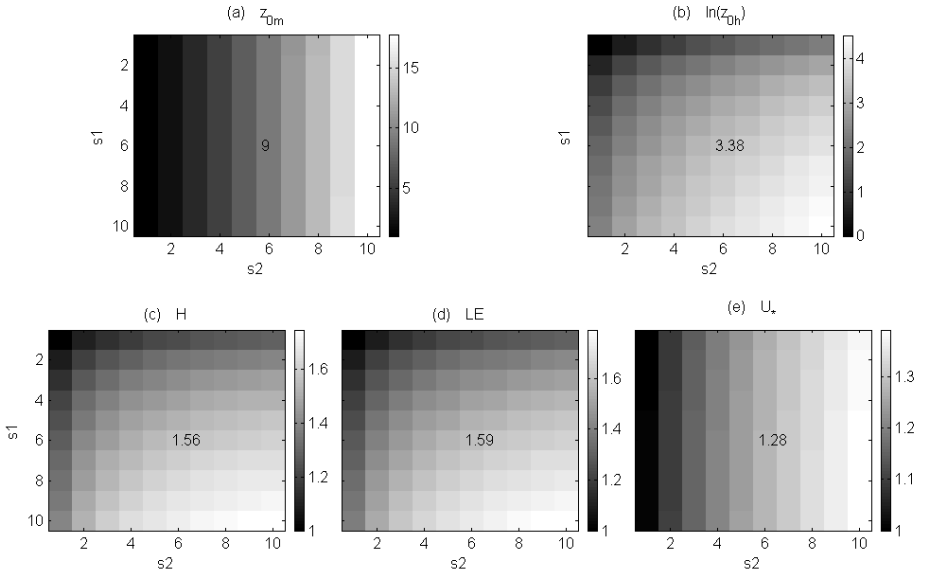

Figure 3.4 The increased ratios of experimental (a) $\mathbf{z_{0m}}$, (b) $\boldsymbol{ln(z_{0h})}$, (c) *H*, (d) *LE* and (e) $\mathbf{u}_*$ using increased $\mathbf{z_{0m}}$ and increased $\mathbf{z_{0h}}$ with original simulations as reference; s1 and s2 indicate the multipliers (1 to 10) of $\mathbf{z_{0m}}$ and $\mathbf{z_{0h}}$. The increased ratios in Figure (3.4a-3.4f) represent the slope values of linear-fitting (passing through the origin) between experimental $\mathbf{z_{0m}}$, $\mathbf{z_{0h}}$, *H*, *LE*, $\boldsymbol{u}_*$ and those from reference simulations; the number in each figure is an example for s1 = s2 = 6.

The above sensitivity analysis showed that z_{0m} and z_{0h}&z_{0q} are important for accurate modeling of water and heat fluxes. The roughness lengths estimated in the method by using "sea parameters" ($\alpha = 0.013, R_r = 0.11$) of z_{0m} were compared to observed values (Figure (3.5)). The observed z_{0m} shows a peak-frequency value of 3.35×10^{-4} m (Figure (3.5a)), while the highest-frequency values of the observed z_{0h} and z_{0q} are also at the peak value of 3.35×10^{-4} m (Figure (3.5b)). However, the z_{0m} and z_{0h} derived using sea parameters in the B method peak at 4.1×10^{-5} m and 9.1×10^{-5} m, respectively. The observed z_{0m} is approximately 8 times larger than the value simulated using sea parameters, and the observed z_{0h} and z_{0q} are almost 4 times higher than those derived using sea parameters in the B method. Additionally, even though the peak values of the observed z_{0h} and z_{0q} are the same (Figure (3.5b)), z_{0q} is larger than the corresponding z_{0h} in most of the observations (Figure (3.5c)). Thus, the models'

assumption that z_{0h} and z_{0q} are the same is inappropriate. The fluxes simulated using sea parameters in the B method and the M method were also validated with EC observations. We found that the B method and the M method underestimate *H*, *LE*, and u_* (Figure (3.6)). The smaller roughness lengths can lead to lower transfer coefficients and thus reduce the heat flux transport. Statistically, the bias in z_{0m} and z_{0h} means that underestimating z_{0m} and z_{0h} can in turn lead to a 23% underestimation of the simulated *H* and *LE* based on sensitivity analysis of the B method. The underestimated roughness lengths in the sea parameters simulations can explain the underestimation of the simulated *H* and *LE*. To resolve the problem of underestimating z_{0m}, we use the EC observations to optimize z_{0m} by calibrating the Charnock number (α) for rough flow and roughness Reynolds number for smooth flow (R_r) for the "small lake".

3.4.3 Optimization of roughness length for momentum

Respectively, α and R_r are often used to represent the variation in z_{0m} for rough seawater flow and smooth seawater flow (Charnock 1955; Fairall et al. 1996b; Smith 1988). The methods used to determine α can be divided into three categories (Gao et al. 2006): (1) constant value or simple wind speed dependence, (2) wave age dependence, and (3) wave steepness dependence. Assuming that the wave field (including wave age and wave steepness) cannot fully develop in the "small lake" and thus will have limited influence on z_{0m}, we assume that α is constant in the "small lake".

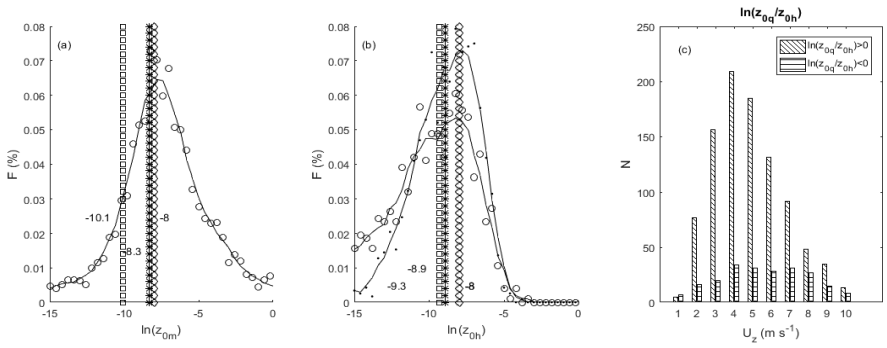

Figure 3.5 Statistical distribution for (a) $\boldsymbol{ln(z_{0m})}$ and (b) $\boldsymbol{ln(z_{0h})}$ and $\boldsymbol{ln(z_{0q})}$; dots are $\boldsymbol{ln(z_{0q})}$ and circles are $\boldsymbol{ln(z_{0h})}$; (c) $\boldsymbol{ln(z_{0q}/z_{0h})}$ at each bin of wind speed. The vertical line of squares indicates the peak value of sea parameters simulation in B method ($\mathbf{ln(z_{0m}) = -10.1}$, $\mathbf{ln(z_{0h}) = -9.3}$); the vertical line of stars indicate the improved parameter simulation in B method ($\mathbf{ln(z_{0m}) = -8.3}$, $\mathbf{ln(z_{0h}) = -8.9}$); the vertical line of diamonds indicate the peak values of observations ($\mathbf{ln(z_{0m}) = ln(z_{0h}) = ln(z_{0q}) = -8}$); "F" and "N" represent frequency and numbers, respectively.

For rough flow, α is estimated to be 0.011 in open sea conditions and 0.03 in coastal areas (Huang 2012; Sempreviva et al. 1990; Smith 1988). As most of these studies focused on the sea-atmosphere interaction, we performed a numerical simulation with the B method in which we used observations to optimize the most appropriate α for the "small lake". We set α to change from 0.001 to 0.1 with a bin size of 0.001. We compared the simulation results with the EC observations, and the normalized RMSE values for each binned α are shown in Figure (3.7a): the smallest RMSE values for *H* and *LE* are achieved when α is 0.012 and 0.036, respectively, with the smallest RMSE value for u_* at 0.031. As z_{0m} is closely related to u_* (the determined momentum flux), we suggest that the optimal value of α for water and heat flux simulation on the "small lake" is 0.031, which is in the range of 0.013 – 0.035 suggested by Fairall et al. (1996a). For smooth flow, a "constant" roughness Reynolds number of R_r= 0.11 is used for sea-atmosphere simulations (Smith 1988). However, for the high-elevation "small lake", which has a distinct lake environment and atmospheric conditions, we performed a similar numerical simulation with the B method (with R_r changing from 0.1 to 1.5 with a bin size of 0.001 and α = 0.031) to determine its proper value. The simulated results show that the smallest RMSE value for *H*+*LE* is achieved when R_r= 0.54 (Figure (3.7b)).

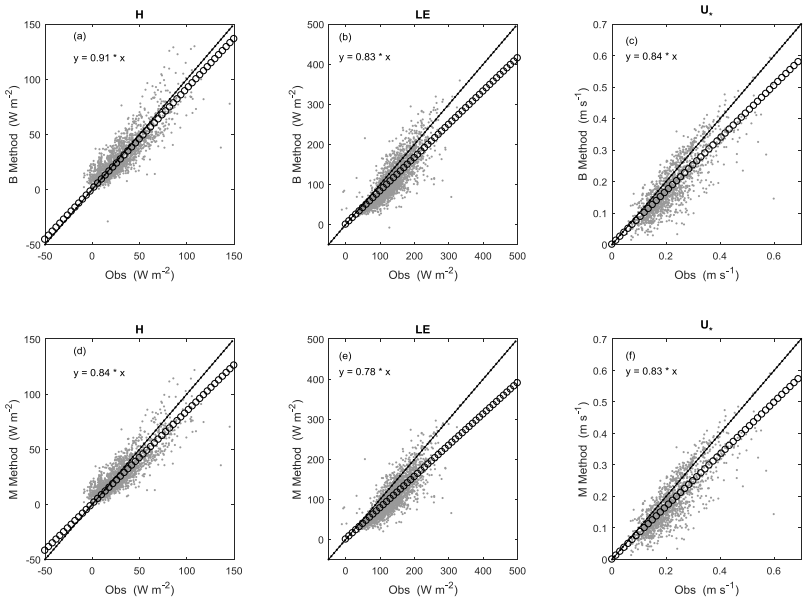

Figure 3.6 Scatterplots of *H*, *LE*, and $\boldsymbol{u}_*$ between simulation using sea parameters (the (a-c) B method and the (d-f) M method) and observations (Obs). The 1:1 linear-fitting lines are shown by the dot and circle lines, respectively, with fitting equations marked.

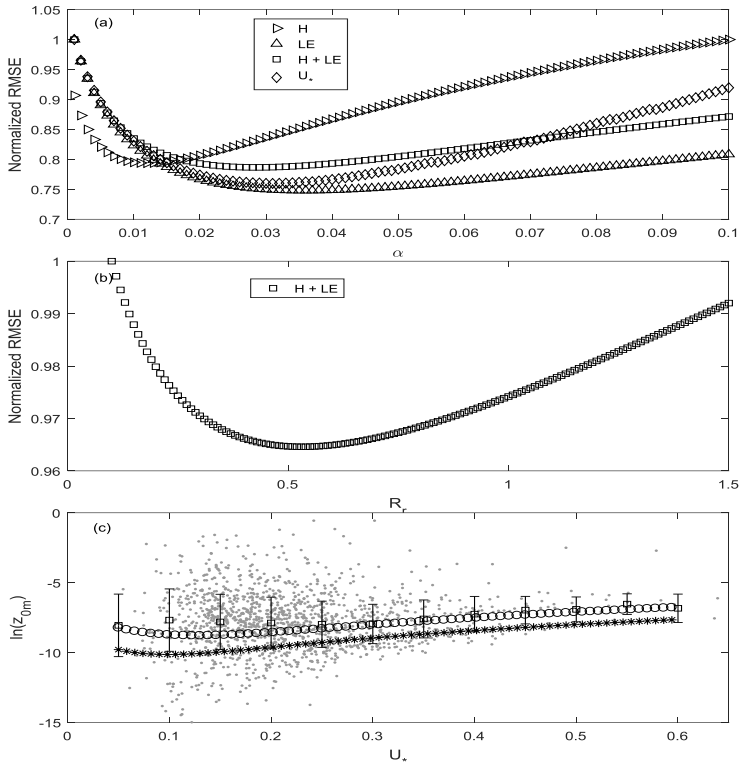

Figure 3.7 Optimization of $\mathbf{z_{0m}}$; (a) the normalized RMSE for $\boldsymbol{\alpha}$, normalized values: *H*, 14.3 $\mathbf{W\,m^{-2}}$; *LE* 47.5 $\mathbf{W\,m^{-2}}$; *H+LE*, 60.5 $\mathbf{W\,m^{-2}}$; $\boldsymbol{u_*}$, 0.0736; (b) the normalized RMSE for $\boldsymbol{R_r}$, normalized value: *H+LE*, 47.74 $\mathbf{W\,m^{-2}}$; (c) the relationships between $\mathbf{ln(z_{0m})}$ and $\boldsymbol{u_*}$. The dots are observations; the squares are the mean of observations for each binned $\boldsymbol{u_*}$ (from 0.05 to 0.6 with a bin size of 0.05, error bars are marked); the star and circle lines are fitting lines of $\boldsymbol{ln(z_{0m})}$ using the sea parameters and the improved parameters, respectively.

After parameter optimization, the "improved parameters" (α = 0.031 and R_r = 0.54) z_{0m} result in a much better fit with the observations than the results obtained using the original sea parameters z_{0m} (Figure (3.7c)). Particularly, compared with the results using the original sea parameters z_{0m}, the results obtained using the improved parameters show that z_{0m} increases with a larger α in rough flow (large u_* in Figure (3.7c)) and with a larger R_r in smooth flow (small u_* in Figure (3.7c)). The increase in α is likely related to the larger roughness length for momentum of the shallow water basin where water surface is much rougher due to short wavelength or short wave period (Gao et al. 2009). Apparently, the effect of short wavelength is dominant over the effect of smaller wave height, while the increase in R_r may be attributed to the geometry of capillary waves and surface tension (Bourassa et al. 1999; Wu 1994). In addition,

the z_{0m} (2.49×10^{-4} m) simulated using the improved parameters is much closer to the peak frequency of observations (Figure (3.5a)), and the simulated z_{0h} and z_{0q} (1.36×10^{-4} m) also increased with the increased z_{0m} (Figure (3.5b)). Finally, the error metrics of *H*, *LE*, and u_* with different parameter combinations are shown in Table (3.1): the RMSE on *LE* improves from 37.99 W m^{-2} to 33.49 W m^{-2} and the RMSE of u_* also decreases from 0.059 to 0.052; however, the RMSE on *H* increases slightly.

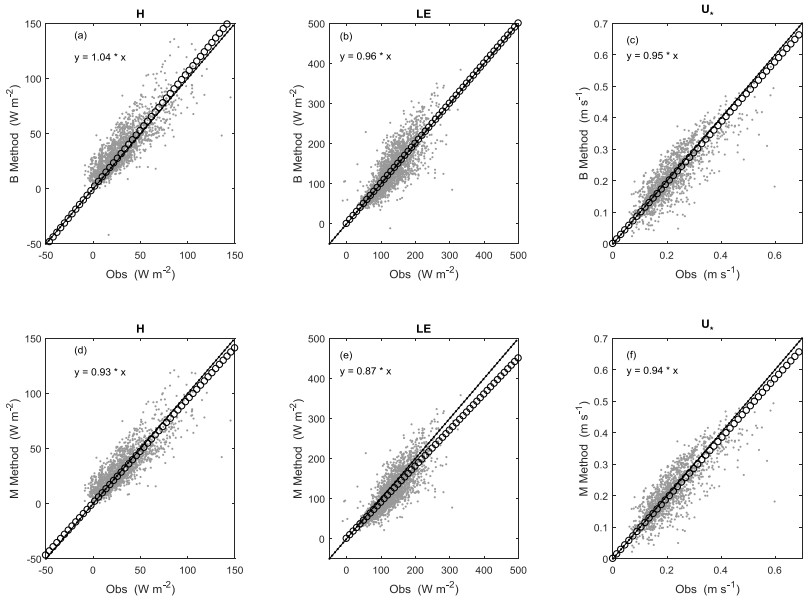

Figure 3.8 Scatterplots of *H*, *LE*, and $\boldsymbol{u_*}$ between simulation using improved parameters (the (a-c)) B method and the (d-f) M method) and observations (Obs); the 1:1 and linear-fitting lines are shown by the dot and circle lines, respectively, with fitting equations marked.

Table 3.1 RMSE of *H*, *LE*, and $\boldsymbol{u_*}$ with different parameters in $\boldsymbol{z_{0m}}$

Parameters	RMSE(*H*, W m^{-2})	RMSE(*LE*, W m^{-2})	RMSE (u_*)
α = 0.013, R_r= 0.11	11.36	37.99	0.059
α = 0.031, R_r= 0.11	11.87	35.72	0.056
α = 0.031, R_r= 0.54	12.31	33.49	0.052

Comparing the model simulations with the EC measurements shows that the linear slopes for the B method are 1.04 and 0.96 for *H* and *LE*, respectively, while those for the M method are 0.93 and 0.87 (Figure (3.8)). Relative to the M method, the better performance of the B method can be attributed to the optimization of z_{0m}. Moreover, the slope values using the improved parameters (Figure (3.8))

versus the sea parameters (Figure (3.6)) show that *H*, *LE*, and u_* are all significantly improved after optimization of z_{0m}. Moreover, the residual underestimation of the M method can be further explained by the model parameters that were kept constant in the fitting. These results indicate that model simulation using the sea parameters of z_{0m} greatly underestimates *H*, *LE*, and u_*, while a proper parameterization of z_{0m} is vital for accurate heat and water exchange modeling on the high elevation shallow small lakes. Statistical evaluations of model performance using improved parameters for z_{0m} are analyzed, where various data quality indicators (1–5) are considered. In general, the R, MAE, and RMSE improve when good quality data are used. The correlation coefficients (R) for *H* (with quality indicators less than 4) for the B method and the M method are 0.85 and 0.86, respectively. Both values represent an improvement on the results of the variational method (0.72) from Cao et al. [2006]. The best values of R, MAE, and RMSE for *LE* are 0.84, 24.2 W m^{-2} and 31 W m^{-2} for the B method, and 0.85, 26.5 W m^{-2}, and 32.7 W m^{-2} for the M method. The determination coefficient (R^2) and MAE for *LE* in both methods are better than those (0.64 and 30.3 W m^{-2}) from Biermann et al. (2013). As for *H*, the MAE and RMSE values do not show large variations for either model and the differences with the results of Biermann et al. (2013) may be caused by observational uncertainty.

3.5 Discussion

3.5.1 Limitations of the models

The relationships between u_*, C_H, and z_m/L in the B method simulations, observations, and the "observations with FCCs removed" are shown in Figure (3.9). It is well known that u_* has a high positive correlation with wind speed (Gao et al. 2006). As indicated in Figures (3.9a2) and (3.9a3), when the wind speed is low, because of large temperature gradients, the atmosphere is always in an unstable condition. When wind speed increases, the atmosphere can shift from an extremely unstable condition (for example, FCCs) to a nearly neutral state. This can also be simulated by the B method as shown in Figure (3.9a1). Figure (3.9b3) shows a nearly constant mean C_H of approximately 0.00195 for observations with FCCs removed. Simulations with the B method confirm this constant C_H value for $u_* > 0.2$. For $u_* < 0.2$, C_H increases because of FCCs. The increase of C_H in free convection is also shown in Figure (3.9b2). As for C_E, its value is higher than C_H when $u_* < 0.3$ and it also corresponds to a larger z_{0q}

than z_{0h} (Figure (3.5c)). An unstable surface layer will enhance the heat flux transport compared to stable conditions. The average decreasing rate from unstable to near neutral conditions is 0.00048 in the B method simulation (Figure (3.9c1)) and 0.00031 for the observations with FCCs removed (Figure (3.9c3)); a much faster decreasing rate of 0.00073 is associated with the EC observations (Figure (3.9c2)). Therefore, FCCs can significantly enhance the water and heat transfer in the vicinity of the water surface, and the B method can only partially correct these effects through the atmospheric stability correction.

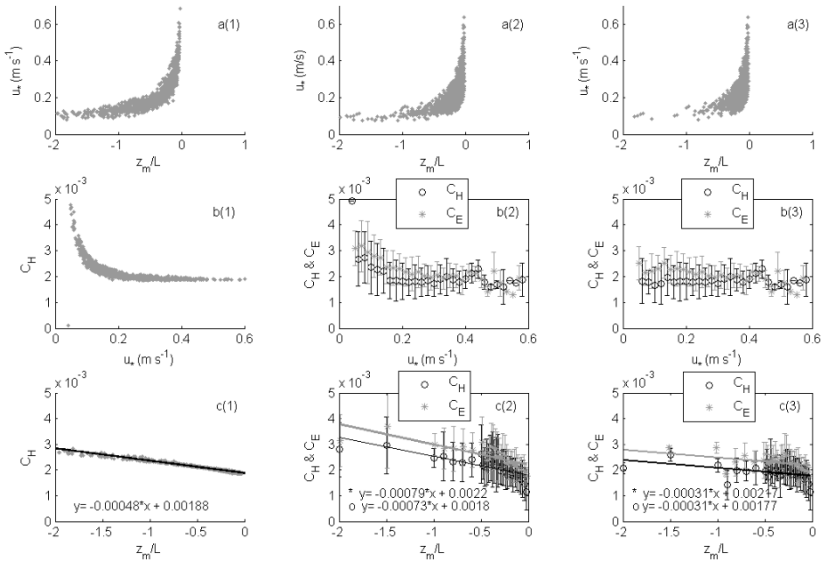

Figure 3.9 The relationships between $\boldsymbol{C_H}$, $\boldsymbol{C_E}$, $\boldsymbol{u_*}$ and $\boldsymbol{Z_m/L}$. (a1, b1, and c1) The B method simulation. (a2, b2 and c2) The observations. (a3, b3 and c3) The FCCs removed observations. The vertical bars in Figure (3.9b2), (3.9b3), (3.9c2) and (3.9c3) indicate the standard deviations. Linear-fitting lines are shown in Figures (3.9c1), (3.9c2) and (3.9c3).

3.5.2 Uncertainties existed in the results

Because of the rapid increase in air temperature influenced by the surrounding land, a stable atmosphere is expected for small lakes during the daytime. However, the "small lake" shows positive values of *H* and persistent unstable and neutral atmosphere conditions, similar to the larger Lake Ngoring studied by Li et al. (2015b). This atmospheric condition together with the observed high wind speeds and large temperature differences may result from the existence of the "large lake" for two reasons: (1) the "large lake" can enhance the wind speed through land-lake breeze circulation; (2) its presence can also reduce air temperatures in the Nam Co Lake basin, as suggested by mesoscale model simulation (Lv et al. 2008). To summarize briefly, because Nam Co Lake's air inflow causes lower air

temperature and higher wind speed, *H* may be enhanced on the "small lake", compared with other small lakes on the TP; and the models' performance under stable conditions needs further validation.

The roughness lengths for heat and water are assumed to be the same in the National Centers for Environmental Prediction (NCEP) medium range forecast model and the algorithm in Goddard Earth Observing Data Assimilation System (Verburg and Antenucci 2010; Zeng et al. 1998). However, Fairall et al. (1996b) gave different values of roughness lengths for temperature and humidity in tropical oceans, and the scalar roughness length ratio (z_{0h}&z_{0q}) was much larger than unity (Vickers and Mahrt 2010). Our results suggest a larger z_{0q} than z_{0h} for the small Nam Co Lake, because (1) values of $\ln(z_{0q}/z_{0h})$ larger than unity are more often observed (Figure (3.5c)); (2) *H* is overestimated while *LE* is underestimated using the optimized α of 0.031 (Figure (3.8)); and (3) the bulk transfer coefficient is larger for water than for heat (Figure (3.9)). Our results show that the roughness length is higher for water than for heat, which agrees with the results of Large and Pond (1982) and the ECMWF model (European Centre for Medium-Range Weather Forecasts) (Zeng et al. 1998). Thus, the assumption that they are the same is inappropriate. Moreover, under FCCs, conventional approaches that use sea-air interactions to determine the roughness length for momentum may also lead to inaccurate results (Fairall et al. 1996b). Adjusting α from 0.013 to 0.031 leads to a limited improvement in model accuracy. However, even without considering factors such as wave age, wave breaking and droplet evaporation effects, lake depth and lake area influence, free convection effects, and cool-skin and warm-layer effects (Fairall et al. 1996b), both models can simulate of heat and water fluxes to an acceptable accuracy.

3.6 Conclusions

Using data collected in the shallow and small Nam Co Lake over the summer ice-free season of 2012, we reached several conclusions concerning lake-atmosphere heat and water transfer processes on this high-elevation "small lake". They can be summarized as follows:

(1) The observed large water-air temperature gradients and strong winds correspond to the prevailing unstable and near-neutral atmospheric conditions. In these conditions, wind speed plays an important role in lake-atmosphere water and heat flux transport; we emphasize the importance of mechanical dynamic effects.

(2) The observed roughness length for momentum is approximately 3.35×10^{-4} m, while the roughness length for water is larger than that for heat. Free convection is associated with higher bulk heat transfer coefficients in conditions of low wind speed and an unstable atmosphere; and it gives a square root dependence of latent heat flux on wind speed. Obviously, parameterization schemes for roughness length for heat and water under FCCs should be further improved.

(3) The simulations of two methods have very high correlation coefficients of 0.99 for *H*, *LE*, and u_*, while the values of *H* and *LE* from the M method are approximately 10% and 9% lower, respectively, than those from the B method. Given the B method's flexible parameters, relative to the experiment-based constants in the M method, the B method is much easier to improve and apply.

(4) Lower estimation in the simulated roughness lengths can lead to underestimation of the bulk transfer coefficients, which in turn causes an underestimation of the simulated heat flux. The proper values of α and R_r in the roughness length for momentum are estimated to be 0.031 and 0.54, respectively, for this high-elevation "small lake". The calibrated models can be applied to estimate fluxes under wind directions from land surface for gap filling, which is important for energy balance analysis of the lake.

Chapter 4 Estimation of evaporation and energy budget

4.1 Introduction

As is well understood, latent heat fluxes (*LE*; with *E* as evaporation, in other words) and sensible heat fluxes (*H*) from lakes are primarily controlled by water vapor and temperature gradients, together with turbulent mixing intensity, which is influenced by surface roughness length, wind speed and atmospheric stability (Assouline et al. 2008; Blanken et al. 2011; Blanken et al. 2000; Granger and Hedstrom 2011; Heikinheimo et al. 1999; Liu et al. 2012; Rouse et al. 2003; Wang et al. 2015; Zhang and Liu 2014). The question of what factors drive turbulent flux exchange between lakes and the atmosphere remains highly relevant. In addition to the widely observed positive correlations between temperature and water vapor gradients on the one hand and sensible and latent heat fluxes on the other (Blanken et al. 2003; Blanken et al. 2000; Liu et al. 2012; Liu et al. 2009a; Liu et al. 2014; Zhang and Liu 2014), net radiation is an important parameter for estimating evaporation over longer periods, such as one day, 10 days, or one month (Rosenberry et al. 2007; Yao 2009). However, no clear positive correlations have been observed between net radiation and turbulent heat flux in deep or large lakes (Blanken et al. 2003; Blanken et al. 2000; Liu et al. 2012; Zhang and Liu 2014). This result contrasts with the positive correlations from shallow lakes over periods longer than a week (Granger and Hedstrom 2011; Nordbo et al. 2011). The reason may be that water surface temperatures in small and shallow lakes respond much faster than those of large or deep lakes to penetration and absorption of solar radiation (Granger and Hedstrom 2011). For small lakes, a positive correlation is found between wind speed and latent heat flux* (Assouline et al. 2008; Granger and Hedstrom 2011), while a poor correlation between these factors has been observed for a 0.041 km^2 boreal lake (Nordbo et al. 2011). For large lakes, wind speed has no relationship with latent heat flux at Ross Barnett Reservoir (Liu et al. 2012; Liu et al. 2009a; Zhang and Liu 2014); however, a positive correlation has been observed for the Great Slave Lake for wind speeds greater than a particular threshold value (Blanken et al. 2003). It has also been found that the presence of unstable (stable)

*** This Chapter is based on the paper:** Wang, B., Y. Ma, W. Ma, and Z. Su (2017), Physical controls on half-hourly, daily and monthly turbulent flux and energy budget over a high-altitude small lake on the Tibetan Plateau, Journal of Geophysical Research: Atmospheres, 122,2289-2303, doi:10.1002/2016JD026109.

atmosphere boundary layers causes *H* and *LE* to increase (decrease) (Brutsaert 1982). Another study found that a large upward *LE* persists during periods when the atmosphere is stable (Heikinheimo et al. 1999). Furthermore, Zhang and Liu (2014) found that, for Ross Barnett Reservoir, water vapor gradient plays a dominant role in determining energy fluxes under conditions involving large water vapor gradients, while atmospheric stability becomes significant under small water vapor gradients. Therefore, the processes controlling turbulent fluxes between lakes and the atmosphere are likely nonlinear and could be affected by many environmental factors (e.g., temperature and water vapor gradients, wind speed, net radiation, and atmospheric stability) (Liu et al. 2012; Zhang and Liu 2014). There is evidence that large latent heat fluxes (evaporation pulses) could be caused by entrainment of warm, dry air into synoptic weather systems (Blanken et al. 2003) or by high-wind events associated with cold fronts (Liu et al. 2012; Liu et al. 2009a), and such pulses have been observed in Lake Ngoring on the TP (Li et al. 2015b). Relative to other low-elevation lakes at the same latitude, the solar radiation is high because of a shorter traveling length in the atmosphere and a smaller air density. A predominantly unstable atmosphere is observed in the Nam Co basin (Biermann et al. 2013; Wang et al. 2015) and Lake Ngoring (Li et al. 2015b). Thorough understanding of the physical controls on turbulent flux over high-elevation lakes on the TP is urgently needed.

Evaporation from lakes is a fundamental component of catchment-scale water balance and energy budget analyses (Rouse et al. 2005; Venalainen et al. 1999; Zhu et al. 2010). Given that they have a lower Bowen ratio (a ratio between *H* and *LE*) and a larger thermal inertia than the surrounding land, lakes favor a lower boundary layer height and increased humidity, which can influence local-scale weather, as well as large-scale circulation patterns (Nordbo et al. 2011). Thus, the responses of lakes to global climate change could be reflected in changes in lake evaporation, which could accelerate climate warming due to increased amounts of water vapor in the atmosphere. Moreover, given that the climate of the TP is changing from cold and dry to warm and wet (Yang et al. 2014), precise estimation of evaporation is significant for clarifying the relative importance of local vertical processes and regional horizontal advection as atmospheric moisture sources (Chen et al. 2012). Further, although energy balance is one of the foundations of evaporation simulation and process modeling (Rosenberry et al. 2007; Yao 2009), studies of energy budget closure are still scarce (Gianniou and Antonopoulos 2007; Nordbo et al. 2011; Sugita et al. 2014; Tanny et al. 2008), especially on the TP. Estimation of evaporation and the energy budget of high-

elevation lakes could provide important information for improving existing models and building new models for simulating these processes.

Lakes, especially small lakes, are sensitive indicators of climate change. The high-elevation lakes of the TP are natural study sites because they have experienced less interference from human activities. In this Chapter, based on long-term EC monitoring systems in the "small lake" and the "large lake", our research has two objectives: 1, to determine the relative significance of several environmental variables (temperature and water vapor gradients, wind speed, net radiation, and atmospheric stability) on turbulent heat fluxes over temporal scales of half-hourly, daily and monthly in the two water bodies; and 2, to obtain an assessment of the evaporation and energy balance closure ratios of the two water bodies.

4.2 Energy budget components

The energy budget of a lake indicates that the incoming energy is balanced by outgoing energy and energy stored in water (Gianniou and Antonopoulos 2007; Tanny et al. 2008), and it can be expressed as eq. (4.1)

$$R_n = H + LE + G_s + G_b + G_a \tag{4.1}$$

where net radiation (R_n, W m^{-2}) is the sum of $R_{s\downarrow}$, $R_{l\downarrow}$, $R_{s\uparrow}$ reflected by the water surface, and $R_{l\uparrow}$ reflected and emitted by the water surface. R_n is balanced by the sensible heat flux (H, W m^{-2}), the latent heat flux (LE, W m^{-2}), the heat storage change in the water (G_s, W m^{-2}), the heat transfer between water and the bottom sediments (G_b, W m^{-2}) and the net energy (G_a, W m^{-2}) gained or lost by the lake due to the exchange of water masses resulting from the inflow-outflow balance. For both lakes, G_a and G_b are omitted in energy budget analysis due to limitations in observations.

Heat storage change in the water can be obtained from lake temperature profiles (Blanken et al. 2000; Nordbo et al. 2011). The heat storage change (G_s) of a lake at a given depth (z, m) over a given time interval (Δt, s) can be calculated using eq. (4.2)

$$G_s = \rho_w c_{pw} \frac{\Delta \overline{T_w}}{\Delta t} \mathrm{z} \tag{4.2}$$

$$\overline{T_w} = \frac{1}{z} \sum_{i=1}^{n} T_{wi} \Delta z_i \tag{4.3}$$

$$G_c = \rho_w c_{pw} (\overline{T_w} - T_r) \mathrm{z} \times 10^{-6} \tag{4.4}$$

where ρ_w (g m^{-3}) and c_{pw} (J kg^{-1} K^{-1}) are the density and specific heat of water, respectively; $\overline{T_w}$ (K) is the mean water temperature; and T_{wi} (K) and Δz_i (m) are the water temperature and the representative thickness of layer i (from 1 to n). When the reference temperature (T_r, K) is taken to represent an ice-water mixture with a value of 0°C and is used as the origin, the cumulative water heat storage (G_c, MJ m^{-2}) can be expressed through eq. (4.4). For the "small lake" in this Chapter, considering the wave effects, lake level variations (less than 20 cm), and strong mixing in the water surface layer, two representative temperatures, one close to the water surface and one at a depth of 60 cm, are chosen to represent the shallow mixing layer and "deep layer", with thicknesses of 0.3 m and 0.7 m, respectively. If the temperature at 60 cm was not available, only the temperature close to the water surface was used, representing a thicknesses of 1 m. The total calculated depth is 1 m if no further information is given.

4.3 Heat flux simulation in the two lakes

4.3.1 Turbulent heat flux simulation in the "small lake"

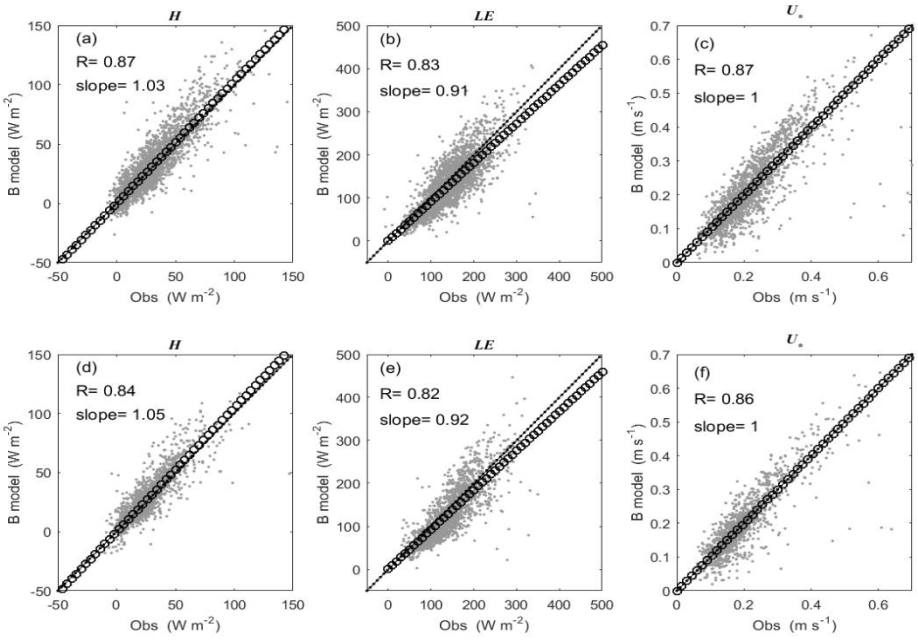

Figure 4.1 Scatterplots of *H*, *LE* and $\boldsymbol{U}_*$ between B method simulations and observations (Obs) in 2012 (a-c) and in 2013 (d-f). Lines drawn with dots and circles represent the 1:1 line and the line of best fit, respectively. Correlation coefficients (R) and the slope of the line of best fit (passing through the origin) are indicated.

The B method, which is optimized for the specific wave pattern of the "small lake" (Wang et al. 2015), is chosen for half-hourly data interpolation to fill gaps due to instrument failure or inadequate footprint and quality. The B method was optimized using observations from 2012 (Figure (4.1a-c)) and was further validated independently for observations from 2013 (Figure (4.1d-f)). The correlation coefficients (0.87 and 0.83) and the slopes of lines of best fit that pass through the origin (1.03 and 0.91) in 2012, which could describe the relationship between simulated and observed *H* and *LE* values, are very close to those (0.84 and 0.82; 1.05 and 0.92) from data in 2013. Therefore, the B method with tuned parameters is appropriate for data interpolation over periods with low-quality or missing observations. However, overestimation in simulated *H* (for which the slope of the line of best fit is larger than 1) and underestimation in simulated LE (for which the slope of the line of best fit is smaller than 1) are found and they result from the differences in observed roughness lengths for heat and for water, which are considered same in the B method simulations (Wang et al. 2015). The MB values are corresponding to the overestimation of simulated *H* and underestimation of simulated *LE* at monthly scales (Table (4.1)). The monthly averaged heat flux could be corrected by mean MB values, which were -2.2 ± 1.1 W m^{-2} for simulated *H* and 11.2 ± 3.7 W m^{-2} for simulated *LE*, respectively. In addition, the simulated monthly *H* and *LE* values follow the observations well, and the values with MB corrections are much closer to the observations.

Table 4.1 MB values of monthly average *H* and *LE* between observations and simulations in 2012 and 2013. SD: standard deviation; unit: W m^{-2}.

Year		Apr	May	Jun	Jul	Aug	Mean	SD
2012	*H*	-3.4	-2.6	-0.9	-1.9	-1.1	-2.0	1
	LE	14.2	7.3	7.7	14.4	11.1	10.9	3.4
2013	*H*	----	-2.2	-2.7	-3.5	-0.7	-2.3	1.2
	LE	----	10.5	15.5	6.2	13.4	11.4	4.0

4.3.2 Turbulent heat flux simulation in the "large lake"

The bulk transfer method with optimized roughness lengths (z_{0m}, z_{0h}, z_{0q}) is also used for simulation of lake-air turbulent heat flux in the "large lake" and the optimized roughness lengths could be found in Section 5.3 of Chapter 5 for more details. The simulations show quite similar results compared with EC observations chosen by criteria of footprint and data quality control (Figure (4.2 a-c)). The RMSE values of *H* and *LE* are only about 10 W m^{-2} and 30.2 W m^{-2} and the correlation coefficients are 0.90 and 0.91, both as good as those in the "small lake" (Wang et al. 2017; Wang et al. 2015). The seasonal variations of

monthly averaged *H*, *LE* and U_* between simulations and observations are quite consistent, with small bias of monthly averaged MB values (Figure (4.2d-f)). The relatively higher MB values of *H* appear in November during period when the *H* is larger. The averaged MB values of *H* and *LE* during the observational periods are only 3.7 W m^{-2} and -2.8 W m^{-2}, respectively, corresponding to a small overestimation of *H* and a minor underestimation of *LE*. The friction velocity (U_*) between simulation and observation has also quite high correlation coefficient (R = 0.87) and good slope values of close to the 1:1 line (Figure (4.2c-f)). Thus, bulk transfer method could simulate lake-air turbulent flux at temporal resolution of half-hourly, and EC observations with bad quality and inadequate footprint could be substituted by B method simulations. The constructed continuous data set is further used for comparative analysis of seasonal variation of turbulent heat flux, evaporation and energy budget in the "small lake" (Wang et al. 2017) and in the "large lake".

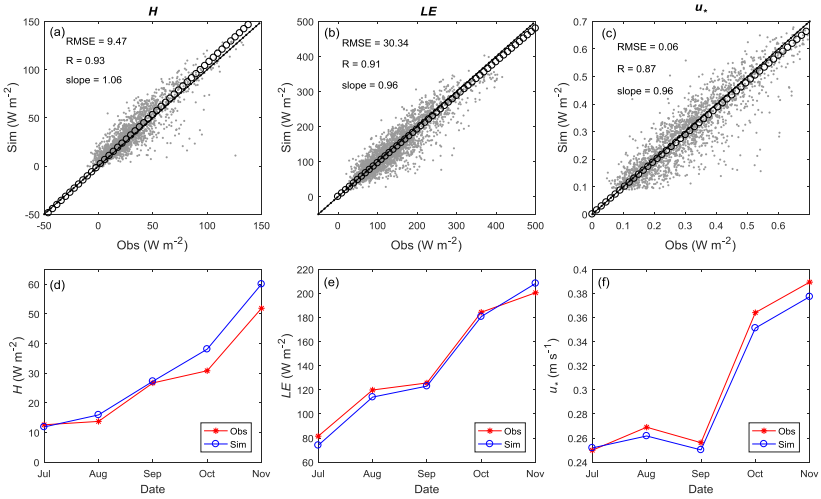

Figure 4.2 Scatterplots of (a) *H*; (b) *LE*; and (c) $\boldsymbol{U}_*$ between bulk transfer method simulations (Sim) and observations (Obs) in 2016 (lines drawn with dots and circles represent the1:1 line and the line of best fit, respectively. Correlation coefficients (R) and the slope of the line of best fit (passing through the origin) are marked) and the monthly average values of (d) *H*; (e) *LE*; and (f) $\boldsymbol{U}_*$ between simulated and observed results over each month.

4.4 Environmental controls on H and LE over different temporal scales

The data used for analysis are mainly from in-situ observations in the "small lake" in section 4.4.1 to section 4.4.3 and the analysis for the "large lake" are shown in section 4.4.4.

4.4.1 Diurnal variation of turbulent flux and environmental variables

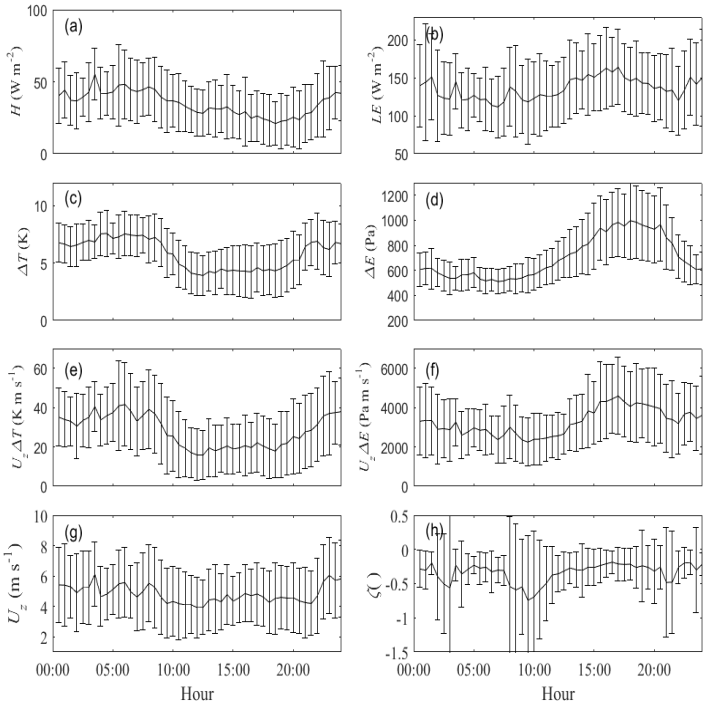

Figure 4.3 Averaged diurnal variation of (a) H, (b) LE, (c) $\Delta \boldsymbol{T}$, (d) $\Delta \boldsymbol{E}$, (e) $\boldsymbol{U_z \Delta T}$, (f) $\boldsymbol{U_z \Delta E}$, (g) $\boldsymbol{U_z}$, and (h) $\boldsymbol{\zeta}$ during the ice-free period in 2012 of the "small lake". Error bars are shown.

H has relatively higher values at night than during the day, similar to the diurnal variation in ΔT (Figure (4.3a) and (4.3c)). LE has relatively high values in the afternoon, which is similar to the variation in the ΔE (Figure (4.3b) and (4.3d)). As shown in Figure (4.3), U_z has a clear influence on the average diurnal variation in H and LE, where 2 peak values are clearly observed at 3:30 and 8:00 in $U_z, U_z \Delta E$, $U_z \Delta T$, H and LE. We deduce that the large latent heat fluxes are caused by coupling effect between U_z and ΔE, with a higher contribution from U_z at night and a higher contribution from ΔE during the day. Moreover, ΔT and

ΔE determine the average diurnal variation in H and LE while U_z adjusted the magnitudes of these fluctuations. Fréchet distances and RMSE values calculated for normalized H, LE and all the environmental variables over diurnal, daily and monthly scales are shown in Table (4.2). Similar as the previous results, the variation of diurnal, daily and monthly values of $U_z\Delta T$ and $U_z\Delta E$ have the smallest Fréchet distances and RMSE values with H and LE, respectively. The variation in ΔE is much more similar to the variation in LE than that in U_z at diurnal, daily and monthly scales. Similarly, the variation in ΔT has a closer similarity with H than that in U_z at daily and monthly scales, with an opposite result at diurnal variations, which may indicate the effect of lake-land breeze circulation. Moreover, atmospheric stability has the least similarity for H and LE with only an exception with LE on monthly scales.

Table 4.2 The Fréchet distances (FD) and RMSE values between important environmental variables and H & LE. All the variables are normalized to the range [0 1].

	Diurnal		Daily		Monthly	
	FD	RMSE	FD	RMSE	FD	RMSE
$H \sim U_z\Delta T$	1.2	0.17	1.4	0.07	0.23	0.11
$H \sim \Delta T$	1.6	0.23	2.2	0.11	0.30	0.15
$H \sim U_z$	1.3	0.19	4.1	0.21	0.46	0.33
$H \sim \zeta$	3.4	0.49	8.0	0.41	0.77	0.45
$LE \sim U_z\Delta E$	1.1	0.16	1.3	0.07	0.17	0.09
$LE \sim \Delta E$	1.8	0.26	2.6	0.13	0.40	0.16
$LE \sim U_z$	2.4	0.35	3.7	0.19	0.54	0.46
$LE \sim \zeta$	2.5	0.49	4.9	0.25	0.48	0.39

4.4.2 Environmental controls on turbulent flux over half-hourly scales

Relative to other single environmental variables, wind speed (U_z) has the most significant contribution to variation of half-hourly H (R^2 = 0.4) and LE (R^2 = 0.48), as shown in Figure (4.4) and Table (4.3). With a relatively high correlation value of ΔT (R^2 = 0.38), the product ($U_z\Delta T$, R^2 = 0.77) of ΔT and U_z determines the variation in H. Even though the correlation between ΔE and LE is weak (R^2 = 0.1), the product of ΔE and U_z enhance the correlations between LE and $U_z\Delta E$ (R^2 = 0.67) significantly. Due to the penetrating and absorbing of solar radiation in the water, R_n is considered to have no obvious correlations with half-hourly H and LE (Zhang and Liu 2014), and this hypothesis is also supported by our observations ($H \sim R_n, R^2 = 0.06$; $LE \sim R_n, R^2 = 0.03$). The atmospheric stability (ζ, R^2 = 0.005) has no correlation with H, while its correlation (R^2 = 0.17) with

LE is even higher than that of ΔE. The strong correlations between ζ and *LE* corresponds to the fact that *LE* increase from "extremely unstable" conditions and achieve its largest value at "neutral" conditions (Figure (4.5e)).

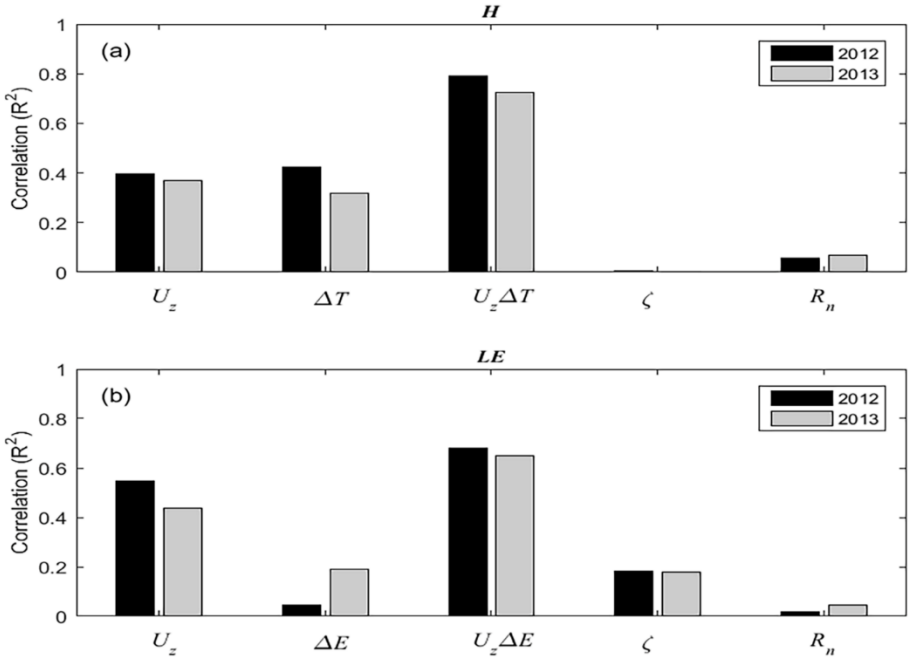

Figure 4.4 The coefficients of determination (R^2) between half-hourly (a) *H*, (b) *LE* and meteorological variables in 2012 and 2013, respectively.

As the correlations between ζ and *H* & *LE* are highly nonlinear (Zhang and Liu 2014), variations of *H*, *LE* and environmental variables are grouped at different atmospheric stability bins ("extremely unstable", [-10 -1]; "unstable", [-1 -0.5]; "weakly unstable", [-0.5 -0.1]; "near neutral", [-0.1 -0.05]; "neutral", [-0.05 0.05]) in Figure (4.5), with coefficients of determination calculated at each bin. Obviously, *H* increases from "extremely unstable" atmosphere, peaks at "near neutral" conditions and then decreases in "neutral" conditions (Figure (4.5a)). And it is near zero or negative under stable conditions (only a few observations were obtained, which are not shown). $U_z\Delta T$ has the largest correlation with *H* in different atmospheric stability bins (Figure (4.5d)). ΔT has relatively higher coefficients of determination than U_z under "extremely unstable" and "unstable" conditions, while under "weakly unstable" to "neutral" conditions, U_z, rather than ΔT, is more strongly correlated with *H* (Figure (4.5b-c)). Additionally, ΔT shows relatively stable correlations with *H* (R^2 = 0.4), while the correlations between U_z and *H* increase from "extremely unstable" condition to "neutral" conditions (R^2

changes from 0.32 to approximately 0.6). Therefore, we conclude that the transport mechanism of H at half-hourly scales has a stable effect through ΔT, while the transport efficiency (U_z) shows increasing significance with increased U_z. For LE, $U_z \Delta E$ describes such variations and has the best correlations under all atmospheric conditions (Figure (4.5h)). The coefficients of determination for U_z are all larger than 0.25 (Figure (4.5f)), while ΔE displays relatively larger correlations under "unstable" conditions but has values close to 0 at "near neutral" and "neutral" conditions (Figure (4.5g)). Thus, it is concluded that U_z makes a relatively significant contribution to LE while ΔE is only important under unstable atmospheric conditions (with smaller wind speeds and larger temperature gradients).

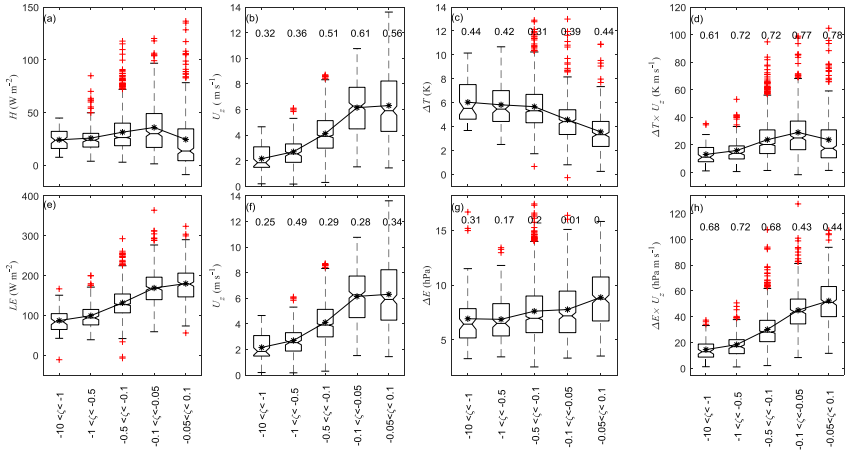

Figure 4.5 Box plots of (a) H, (b) $\boldsymbol{U_z}$, (c) $\boldsymbol{\Delta T}$, (d) $\boldsymbol{U_z \Delta T}$, (e) LE, (f) $\boldsymbol{U_z}$, (g) $\boldsymbol{\Delta E}$, and (h) $\boldsymbol{U_z \Delta E}$ in different stability bins. The average value of each variable in each stability bin is plotted as an asterisk, and the coefficients of determination (R^2) for the stability bins are given in (b-d) and (f-h), respectively.

Table 4.3 Coefficients of determination (R^2) between H & LE and environmental variables for 2012, 2013 and both years together.

(R^2)		2012	2013	All	(R^2)		2012	2013	all
$H \sim U_z$	30 M	0.40	0.37	0.40	$LE \sim U_z$	30 M	0.55	0.44	0.48
	Daily	0.11	0.04	0.06		Daily	0.34	0.14	0.24
	Monthly	0.17	0.58	0.20		Monthly	0.51	0.33	0.18
$H \sim \Delta T$	30 M	0.42	0.32	0.38	$LE \sim \Delta E$	30 M	0.04	0.19	0.10
	Daily	0.56	0.74	0.66		Daily	0.48	0.66	0.56
	Monthly	0.61	0.95	0.71		Monthly	0.85	0.95	0.88
$H \sim U_z \Delta T$	30 M	0.79	0.72	0.77	$LE \sim U_z \Delta E$	30 M	0.67	0.66	0.67
	Daily	0.86	0.90	0.87		Daily	0.92	0.92	0.92
	Monthly	0.94	0.93	0.91		Monthly	0.97	0.99	0.97
$H \sim \zeta$	30 M	0.005	0.002	0.005	$LE \sim \zeta$	30 M	0.18	0.18	0.17
	Daily	0.002	0.01	0.005		Daily	0.39	0.15	0.27
	Monthly	0.06	0.21	0.05		Monthly	0.77	0.22	0.59
$H \sim R_n$	30 M	0.06	0.07	0.06	$LE \sim R_n$	30 M	0.02	0.04	0.03
	Daily	0.09	0.23	0.17		Daily	0.08	0.34	0.19
	Monthly	0.27	0.97	0.58		Monthly	0.08	0.68	0.36

4.4.3 Environmental controls on turbulent flux over daily and monthly scales

On daily scales, the daily average T_s and vapor pressure (E_s) at the water surface are larger than the daily average T_a and vapor pressure (E_a) in the air (Figure (4.6g-h)). Thus, the positive daily average ΔT (6.31 K) and ΔE (686.9 Pa) indicate that large amounts of heat are released through H and LE, and the average values of H and LE are 33.3 W m^{-2} and 112.8 W m^{-2}, respectively, for the summer ice-free period. H is largest during periods with larger ΔT while LE is larger during the months when ΔE is larger (Figure (4.6a-d)). The most obvious evidence for the influence of ΔT on H is seen around November 2013, when large values of H coincide with large ΔT values; while in both June 2012 and June 2013, the variations in LE clearly parallels similar variations in ΔE. Meanwhile, there also exists an average wind speed of 3.46 m s^{-1} (Figure (4.6e)) and the atmosphere is always in an unstable condition (Figure (4.6f)) due to the large ΔT and ΔE.

Of all the single meteorological variables as shown in Table (4.3), ΔT and ΔE show the best correlations with H and LE for daily and monthly scales. In contrast, U_z has relatively small correlations with H & LE at daily and monthly scales, however the contribution from U_z cannot be ignored. It could increase the correlations of both H & $U_z \Delta T$ and LE & $U_z \Delta E$ significantly, so that they are all

larger than 0.87. In addition, ΔE in November of 2012 is larger than that in 2013, however, larger values of *LE* are observed in 2013 with greater contributions from U_z, as shown in Table (4.3). Thus, cold fronts (Liu et al. 2009a) and entrainment of dry air (Blanken et al. 2003), together with the effects of high winds, are considered to be evaporation pulse events, which are thought to increase evaporation through large U_z and large ΔE. Atmosphere stability is almost uncorrelated with *H*, while the coefficient of determination between *LE* and atmospheric stability is 0.27 for daily scale and 0.59 for monthly scale. R_n has a negative correlation with *H* (R^2 = 0.17), which reflects the phenomenon of observed larger temperature gradient during low temperature periods (i.e., at night or during cool seasons). And R_n has a weak positive correlation with *LE* ,similar as in (Granger and Hedstrom 2011; Nordbo et al. 2011). Moreover, U_z shows relatively larger correlations at half-hourly scale than at daily and monthly scales. Meanwhile, the correlation coefficients increase from half-hourly scales to monthly scales for ΔT ($U_z \Delta T$) and ΔE ($U_z \Delta E$). Atmospheric stability and net radiation have better correlations for *H* and *LE*, respectively, at daily and monthly scales than at half-hourly scales.

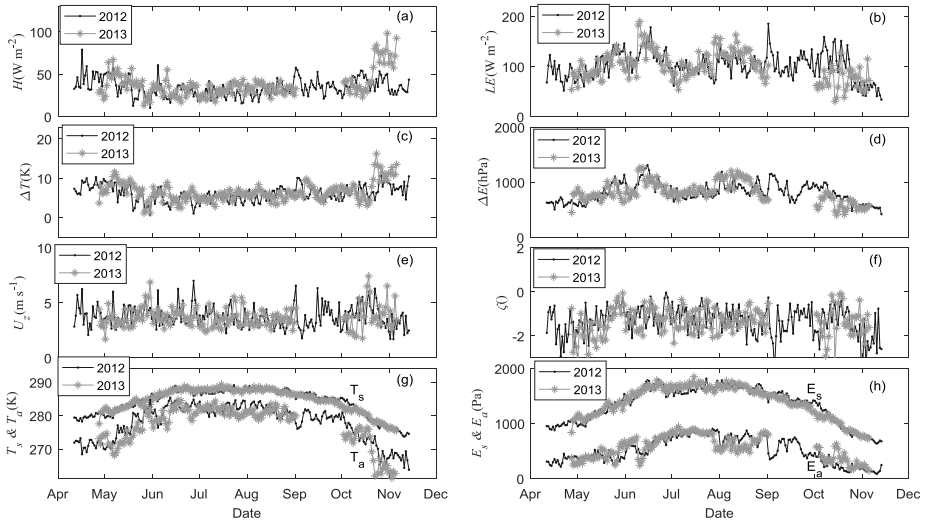

Figure 4.6 Variation of daily (a) *H*, (b) *LE*, (c) $\Delta \boldsymbol{T}$, (d) $\Delta \boldsymbol{E}$, (e) $\boldsymbol{U_z}$, (f) $\boldsymbol{\zeta}$, (g) $\boldsymbol{T_s}$&$\boldsymbol{T_a}$ and (h) $\boldsymbol{E_s}$&$\boldsymbol{E_a}$ in ice-free periods of 2012 and 2013.

4.4.4 Environmental controls on turbulent flux in the "large lake"

Table 4.4 Correlation coefficients (R) between *H* & *LE* and environmental variables of the "large lake" from July to November in 2016.

Variables	Temporal scales	(R)	Variables	Temporal	(R)
$H \sim U_z$	30 Minutes	0.23	$LE \sim U_z$	30 Minutes	0.81
	Daily	0.48		Daily	0.81
$H \sim \Delta T$	30 Minutes	0.66	$LE \sim \Delta E$	30 Minutes	0.34
	Daily	0.84		Daily	0.66
$H \sim U_z \Delta T$	30 Minutes	0.77	$LE \sim U_z \Delta E$	30 Minutes	0.93
	Daily	0.99		Daily	0.98
$H \sim \zeta$	30 Minutes	-0.15	$LE \sim \zeta$	30 Minutes	0.22
	Daily	0.18		Daily	0.43

The environmental controls on turbulent heat flux in the "large lake" are listed in Table (4.4). Quite similar as in the "small lake", the correlation coefficients at half-hourly scale are 0.93 ($\Delta E \times U_z$), 0.81 (U_z) and 0.34 (ΔE) for LE and 0.77 ($\Delta T \times U_z$), 0.66 (ΔT) and 0.23 (U_z) respectively for H in the "large lake". Atmosphere stability (ζ) show weak correlations. Thus, it could be inferred that U_z is the most significant factor in simulation of half-hourly evaporation over lakes on the TP, and it has also been confirmed by high elevation lakes of Qinghai lake (Li et al. 2016) and Serling lake (Guo et al. 2016). When the relative contribution of environmental factors are analyzed over temporal scale of daily, all the correlation coefficients increased, especially for ΔE (0.34 to 0.66 in Table (4.4)). However, much higher correlation coefficients between LE and U_z should result from the monotonically increasing trends of U_z and LE in the "large lake", compared with no significant variation of U_z in the "small lake".

4.5 Energy budget and evaporation of the two lakes

4.5.1 Energy budget and evaporation in the "small lake"

4.5.1.1 Energy budget in the "small lake"

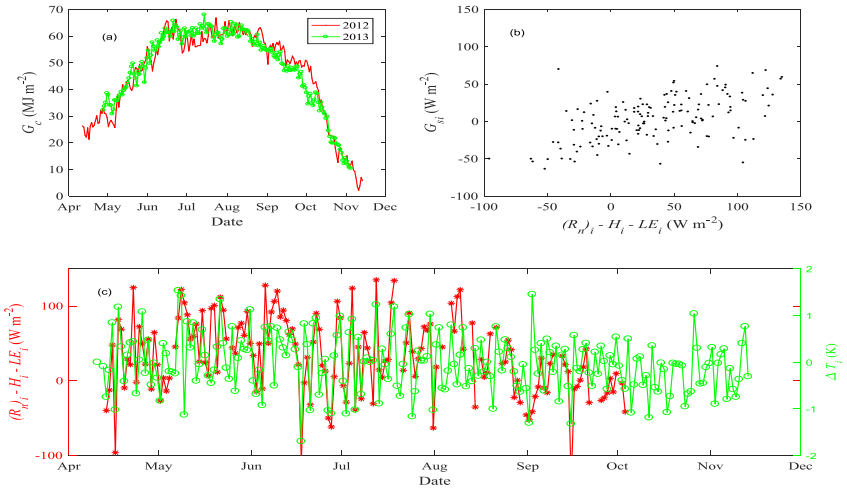

Figure 4.7 (a) Variation in $\boldsymbol{G_c}$ in 2012 and in 2013; (b) relationship between daily water heat flux ($\boldsymbol{G_{si}}$) and $\boldsymbol{(R_n)_i - H_i - LE_i}$ at day i over the ice-free period of 2012; (c) variation in $\boldsymbol{(R_n)_i - H_i - LE_i}$ and $\boldsymbol{\Delta T_i}$ in 2012.

During the ice-melt period, water and ice are mixed with all the energy used for phase transition, and the temperature at 0°C is considered as a reference for the cumulative heat storage (G_c) calculation. The variation in G_c, the relationship between "daily residual heat" (defined as $(R_n)_i - H_i - LE_i$ here) and daily water heat storage (G_{si}), and the variation in "daily residual heat" and temperature difference of pairs of consecutive days (ΔT_i) are shown in Figure (4.7). Generally, lake gains heat from April to June and releases it mainly through October (Figure (4.7a)), when turnover may speeds up the heat release process as in Nordbo et al. (2011). G_c achieves a maximum value of approximately 65 MJ m^{-2} in both 2012 and 2013. This value is smaller than that from a 0.041 km^2 lake Valkea-Kotinen (Nordbo et al. 2011), which has a higher average temperature at 1 m depth. The "daily residual heat" has a positive correlation coefficient (R = 0.6) with the total G_{si} (Figure (4.7b)). However, it should be noted that daily residual heat are calculated by averaged half hourly data while G_{si} is the daily total stored heat at 1 m depth in the water. Moreover, the variation in "daily residual heat" corresponds well with the variation in ΔT_i (Figure (4.7c)), and the observation that positive (negative) residual heat corresponds to lake temperature increase

(decrease) justifies our observations. The variation in G_c also indicates that heat release (accumulation) could also occur during periods when heat is stored (released). The average energy balance closure (EBC) ratio, considering temporal scales of daily, from the 10th of April 2012 to the end of September 2012 is approximately 0.836.

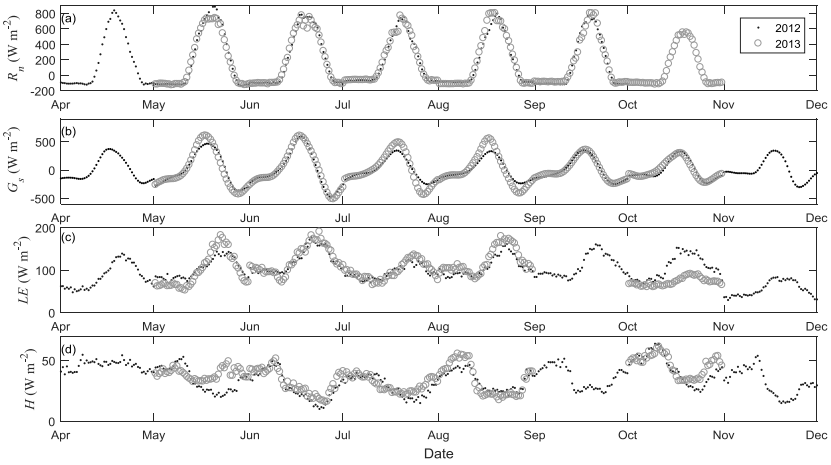

Figure 4.8 Monthly averaged diurnal cycles of (a) net radiation ($\boldsymbol{R_n}$); (b) water heat storage ($\boldsymbol{G_s}$); (c) latent heat flux (*LE*); and (d) sensible heat flux (*H*) in 2012 and 2013.

The diurnal cycle of monthly average R_n peaks at solar noon (approximately 14:00 GMT+8) and is negative at night, with values ranging from 800 W m^{-2} to -130 W m^{-2} (Figure (4.8a)). R_n is generally larger than that from a low-elevation lake (Liu et al. 2012) at a similar latitude. The diurnal cycles of G_s behaved similarly to net radiation, with earlier peaks due to the occurrence of the largest temperature increases at approximately 12:00 (GMT+8) in Figure (4.8b). The values, with "deep layer" included, ranged from approximately 370 W m^{-2} (in April) to -300.0 W m^{-2} (in November), and most of the energy gained during the day was released at night. Moreover, G_s obtained through surface temperature (one close to the water surface) has a much larger amplitude than that through two temperatures (one close to the water surface and one at 60 cm), i.e. July and August in 2012 and 2013. However, this difference is quite small during heat releasing period in September and October. G_s fuels the nighttime turbulent fluxes, where significant nocturnal *LE* and *H* are present. *H* generally reaches its minimum value in the afternoon and its maximum value in the early morning (Figure (4.8d)), with similar diurnal variations as in the temperature gradient (Liu et al. 2012). The different shape of *H* in April was influenced by U_z, with relatively small values at night and relatively large values during the day; these values ranged from 15 W m^{-2} to 55 W m^{-2}. Diurnal cycles of *LE* achieve their

maximum values in the afternoon (18:00 (GMT+8)) while the minimum values occur at night (Figure (4.8c)).

Table 4.5 Monthly averaged environmental variables and heat fluxes during the open-water period in 2012 and 2013 and averages of the 2012 and 2013 values (Ave). A lake depth of 2 m is assumed for $\boldsymbol{G_s}$ here.

Variables	Year	Apr	May	Jun	Jul	Aug	Sep	Oct	Nov
ΔT (K)	2012	8.09	5.95	4.60	5.04	5.89	6.19	7.24	7.54
	2013	------	7.27	5.59	5.35	5.65	6.54	7.96	11.61
	Ave	8.09	6.61	5.10	5.20	5.77	6.37	7.6	9.58
ΔE (Pa)	2012	498.7	669.6	830.7	645.0	778.5	760.1	628.5	430.6
	2013	------	648.0	815.0	707.7	844.2	548.6	482.0	396.1
	Ave	498.7	658.8	822.9	676.4	811.4	654.4	555.3	413.4
U (m s^{-1})	2012	3.59	3.64	3.65	3.43	3.21	3.41	3.79	2.79
	2013	------	3.53	3.50	3.32	3.24	3.95	3.62	3.14
	Ave	3.59	3.59	3.58	3.38	3.23	3.68	3.71	2.96
ζ ()	2012	-1.65	-1.16	-1.06	-1.06	-1.35	-1.37	-1.38	-2.25
	2013	------	-1.54	-1.18	-1.31	-1.24	-0.52	-1.34	-1.81
	Ave	-1.65	-1.35	-1.12	-1.19	-1.30	-0.95	-1.36	-2.03
H (W m^{-2})	2012	43.6	32.3	26.6	26.6	31.2	33.9	41.2	29.6
	2013	------	36.6	29.7	28.3	31.5	----	44	----
	Ave	43.6	34.5	28.2	27.5	31.4	33.9	42.6	29.6
LE (W m^{-2})	2012	96	114	132.9	105.6	119.1	119.9	116.6	64.9
	2013	------	109.3	134.8	107.8	132.1	----	83.4	66.5
	Ave	96	111.7	133.9	106.7	125.6	119.9	100	65.7
G_s (W m^{-2})	2012	10.6	4.9	6.9	0.6	0.6	-3.3	-8.8	-8.2
	2013	10.6	5.3	6.8	1.1	-0.7	-4.0	-8.2	-5.9
	Ave	10.6	5.1	6.9	0.8	-0.04	-3.7	-8.5	-7.0
R_n (W m^{-2})	2012	161.8	202.1	200.5	167.8	167.4	143.3	----	----
	2013	----	182.4	193.0	170.3	177.6	----	82.1	----
	Ave	161.8	192.3	196.8	169.1	172.5	143.3	82.1	----
EBC	Ave	0.92	0.78	0.85	0.80	0.91	1.05	1.57	----

The average energy balance closure (EBC) ratio is 0.93 during part of the whole open-water period (from the 10th of April to the 31st of October) with values falling between a minimum of 0.78 in May and a maximum of 1.57 in October (Table (4.5)). Most of the energy absorbed in April to June is released during September to November, whereas the water storage in July and August is relatively small. If the unavailable net radiation in November were to have a value of 50 W m^{-2}, the EBC value would be much closer to one (0.97).

4.5.1.2 Evaporation in the "small lake"

Evaporation from the "small lake" during the ice-free period (from 10th April through 10th November) is approximately 812 mm, which is larger than the simulated evaporation value (627 mm) of the "large lake", which are derived using the Flake model (Lazhu et al. 2016), the CRLE method (Ma et al. 2016) and bulk methods (Shigenori et al. 2009; Xu et al. 2009). The evaporation from the "small lake" is much larger than that of lake Ngoring (Li et al. 2015b), which has a value of 440 mm from June to November. In addition to lake Ngoring's large area and great depth, it also experiences smaller net radiation, which may be the main factor explaining why it experiences relatively small evaporation compared with our results. Our result is much closer to the evaporation determined by EC and artificial neural network (ANN) methods in Erhai Lake, which has an evaporation value of 874 mm (Liu et al. 2014), Bulk method-derived evaporation estimates from Yamdrok Yum Co, which has an evaporation value of 830 mm (Yu et al. 2011) and Penman method-derived evaporation from Zige Tang Co, which has an evaporation value of 747 mm (Li et al. 2001) over the same period. The differences in intensity of wind-induced mixing, mixed-layer depth, duration of ice-cover periods, climatic backgrounds (radiation, cloud cover, etc.), morphological characteristics (shape, depth, area, etc.), surrounding environments and the type of simulation methods used (bulk methods, Penman methods, etc.) will introduce uncertainties into the reported evaporation values.

Table 4.6 Evaporation from high-altitude lakes on the Tibetan Plateau. $\bar{E}$ is the total evaporation over the whole year; E indicates evaporation over specified months. Superscript "*" indicates average value of 2012-2013 in (Lazhu et al. 2016).

	Area; Dep.; Alt.; Ice free period	Year	Methods	$\bar{E}$ (mm)	E (mm)	*Ref.*
Nam Co	2000 km^2; 40 m; 4730 m; Jun-Jan	1979-2012	CRLE	----	635 Jun-Jan	(Ma et al. 2016)
Nam Co	Ibid	1979-2014	Flake model	832	642* Jun-Jan	(Lazhu et al. 2016)
Nam Co	Ibid	1961-2005	Bulk method	621	----	(Xu et al. 2009)
Nam Co	Ibid	2006-2008	Bulk method	658	603 Jun-Jan	(Shigenori et al. 2009)
Yamdrok Yum Co	638 km^2; 20-40 m; 4441.5 m; Apr-Nov	1961-2005	Bulk method	1252	830 Apr-Nov	(Yu et al. 2011)
Ngoring	610 km^2; 17 m; 4274 m; Apr-Nov	2011-2012	EC	----	436 Jun-Nov	(Li et al. 2015b)
Erhai	256.5 km^2; 10 m; 1978 m; whole year	2012	EC and ANN	1165	874 Apr-Nov	(Liu et al. 2014)
Zige Tang Co	187 km^2; 38.9 m; 4560 m; ----	1958-1998	Penman method	925	747 Apr-Nov	(Li et al. 2001)
Small lake adjacent to Nam Co	1 km^2; 7 m; 4730 m; Apr - Nov	2012-2013	EC and Bulk method	----	812 10th Apr-10th Nov	[*Wang et al., 2017*]

4.5.2 Energy budget and evaporation in the "large lake"

Table 4.7 Monthly averaged environmental variables and heat fluxes during the open-water period of the "large lake" in 2015 and 2016. "$\overline{Ave}$" indicates averages of variables from July to November (August to November in 2015).

Variables	Year	July	August	September	October	November	$\overline{\text{Ave}}$
T_s (℃)	2015	----	11.8	12.0	9.9	7.2	10.2
	2016	11.5	12.1	12.1	9.4	6.8	10.4
	Ave	11.5	12.0	12.1	9.7	7.0	**10.4**
$\overline{T_w}$ (℃)	2015	----	9.9	10.4	9.2	7.1	9.2
	2016	8.3	9.7	10.4	8.8	6.7	8.8
	Ave	8.3	9.8	10.4	9.0	6.9	8.9
ΔT (K)	2015	----	2.41	1.87	6.14	7.04	5.68
	2016	1.36	1.81	4.91	5.44	6.69	6.27
	Ave	1.36	2.11	3.39	5.79	6.87	**6.42**
ΔE (Pa)	2015	----	633.4	711.2	894.6	765.2	751.1
	2016	523.8	626.2	711.7	777.1	796.5	687.0
	Ave	523.8	629.8	711.4	835.8	780.8	**696.3**
U_z (m s^{-1})	2015	----	4.3	5.4	4.9	6.5	5.3
	2016	4.7	4.7	4.6	5.6	6.4	5.2
	Ave	4.7	4.5	5.0	5.3	6.4	**5.2**
H (W m^{-2})	2015	----	19.4	21.2	39.6	52.8	33.2
	2016	10.5	13.8	27.3	35.2	48.0	27.0
	Ave	10.5	16.6	24.2	37.4	50.4	**27.8**
LE (W m^{-2})	2015	----	95.0	127.2	153.0	168.4	135.9
	2016	75.7	94.3	109.8	146.1	170.3	119.2
	Ave	75.7	94.7	118.5	149.5	169.4	**121.6**
R_n (W m^{-2})	2015	----	186.0	178.8	97.3	36.6	124.7
	2016	207.6	221.7	140.1	91.8	40.0	140.3
	Ave	207.6	203.9	159.5	94.6	38.3	**140.8**
G (W m^{-2})	2015	----	115.6	1.5	-134.4	-218.0	-58.8
	2016	74.4	121.9	-31.6	-168.0	-167.0	-34.1
	Ave	74.4	118.8	-15.1	-151.2	-192.5	**-33.1**
Bo ( )	2015	----	0.204	0.166	0.259	0.313	0.236
	2016	0.139	0.146	0.248	0.241	0.282	0.211
	Ave	0.139	0.175	0.204	0.250	0.298	**0.229**
EBC	2015	----	1.625	0.837	0.831	0.869	1.041
	2016	0.647	1.083	0.798	0.698	1.055	0.856
	Ave	0.647	1.308	0.817	0.761	0.952	**0.859**

The radiation budget components and net radiation during the EC observational periods of the "large lake" are shown in Figure (4.9) and the energy budget components including the meteorological variables are summarized in Table (4.7). R_n peak in July while *LE* peak in November, thus *LE* show about 4 months lag of R_n. Mean temperature of the whole water column ($\overline{T_w}$) shows largest value in September which is also the turning point from heat storage to heat release in the "large lake" while it is around August in the "small lake" (Wang et al. 2017). The seasonal variation of *LE* in the "large lake" by Flake simulations (Lazhu et al. 2016) also shows an increasing trend from summer to Autumn, but the largest value appears in October, which is one month earlier than the observations. During July through November, the Bowen ratio ($Bo = \frac{H}{LE}$) in the "large lake" shows an increasing trend from 0.139 to 0.298, with an average value of around 0.21, which is generally smaller than the average value (Bo = 0.333) in the "small lake" during the same months (Wang et al. 2017). When assuming the heat budget is balanced during July to November, The sum of R_n minus *LE* and *H* at temporal scale of monthly is -8.6 W m^{-2}, which corresponds to the heat release of the "large lake" with $\overline{T_w}$ decreasing from 8.3 ℃ to 6.9 ℃. The higher Bowen ratios ($Bo = \gamma \frac{(T_s - T_a)}{(E_s - E_a)}$) could also be explained by the meteorological observations of higher temperature gradients and nearly similar water vapor gradients in the "small lake" than in the "large lake". The energy budget closure ratio ($EBC = \frac{H+LE}{R_n - G}$) ranges from 0.647 in July to 1.308 in August, with an average value of 0.859 during July to November.

Table 4.8 Radiation components (downward shortwave radiation ($\boldsymbol{R_{s\downarrow}}$), downward longwave radiation ($\boldsymbol{R_{l\downarrow}}$), upward longwave radiation ($\boldsymbol{R_{l\uparrow}}$), net radiation ($\boldsymbol{R_n}$)) of the "large lake" in 2016, units: $\boldsymbol{W\ m^{-2}}$.

Months	$R_{s\downarrow}$	$R_{l\downarrow}$	$R_{l\uparrow}$	R_n
Jan	158.3	178.2	311.7	16.1
Feb	214.2	182.6	308.5	76.5
Mar	245.0	211.0	310.0	132.5
Apr	277.1	233.0	316.5	178.4
May	310.0	252.2	328.3	216.9
Jun	294.8	296.2	347.7	227.1
Jul	282.6	302.4	362.8	206.7
Aug	317.5	289.7	371.4	218.3
Sep	230.6	290.3	366.5	141.7
Oct	220.5	237.5	352.3	93.6
Nov	191.1	191.5	337.4	34.7
Dec	154.8	189.0	326.4	8.9

The observed evaporation in the "large lake" is smaller than those in the "small lake" during July to September, but are larger during October and November. The observed total evaporation from July to November in the "large lake" is around 630 mm. The total evaporation over the ice-free season of the "small lake" is around 812 mm (Wang et al. 2017). More details about the comparison of the two water bodies could be found in Chapter 5. To obtain the total evaporation of the "large lake", we made a reasonable hypothesis that the heat stored in the water after ice-out could all be released before ice-formation, thus the evaporation could be determined by R_n and Bo. Table (4.8) shows the radiation budget components of the "large lake" in 2016. Where $R_{s\downarrow}$ and $R_{l\downarrow}$ come from radiation observation in the island while $R_{l\uparrow}$ is estimated by lake zone average of 8-day composition of lake surface temperature from MODIS products (MOD11A2 and MYD11A2), which contain both day and night products at a spatial resolution 1 km × 1 km. Firstly, R_n is highest in June and lowest in December, with all the values being positive. The positive R_n is corresponding to the observed positive *LE* and *H*, even during the ice-covered period. Secondly, the $R_{l\uparrow}$ estimated by MODIS land surface temperature products has a mean bias of -5 W m^{-2} compared with $R_{l\uparrow}$ derived using water surface temperature. The $R_{l\uparrow}$ is quite close after bias correction as shown in figure (4.9c). Lastly, the total R_n from May to January is

1164 W m^{-2}, thus, the evaporation during open water period of the "large lake" is around 981 $\pm$ 18 mm, assuming a Bo of 0.229 with an uncertainty of 10%.

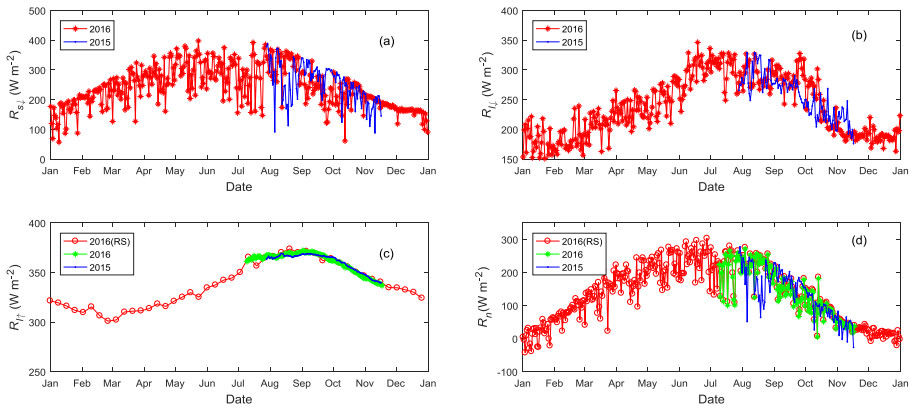

Figure 4.9 Variation of daily (a) downward short wave radiation ($\boldsymbol{R_{s\downarrow}}$); (b) downward longwave radiation ($\boldsymbol{R_{l\downarrow}}$); (c) upward longwave radiation ($\boldsymbol{R_{l\uparrow}}$); (d) net radiation ($\boldsymbol{R_n}$) in 2015 and 2016. "2016 (RS)" indicates the MODIS products.

4.6 Discussions

4.6.1 Water balance analysis in the "small lake"

Precipitation, evaporation and water level changes are the dominant factors of the water budget in the "small lake" (Figure (4.10)), ignoring the unobserved subsurface inflow and outflow. The lake level dropped from early April (ice-melt period) to the end of June in both years, at which time the precipitation minus evaporation was generally smaller than 0 (Figures (4.10a) and (4.10b)). Afterwards, the lake level rose approximately 80 mm in 2012 and approximately 200 mm in 2013 due to monsoon precipitation extending into October. The total amounts of precipitation were 436.7 mm and 487.9 mm in 2012 and in 2013, respectively (Figure (4.10c)). The changes in the lake level closely tracked the precipitation minus evaporation ($Prec_i - E_i$) as shown in Figure (4.10b); thus, precipitation is the main source of water supply in the "small lake". The level of Nam Co lake increases every year until the end of September and then decreases afterwards. Because the rate of lake level change is much lower in the "small lake" than in the "large lake" (Figure (4.10a)), no direct water exchange exists between the two water bodies.

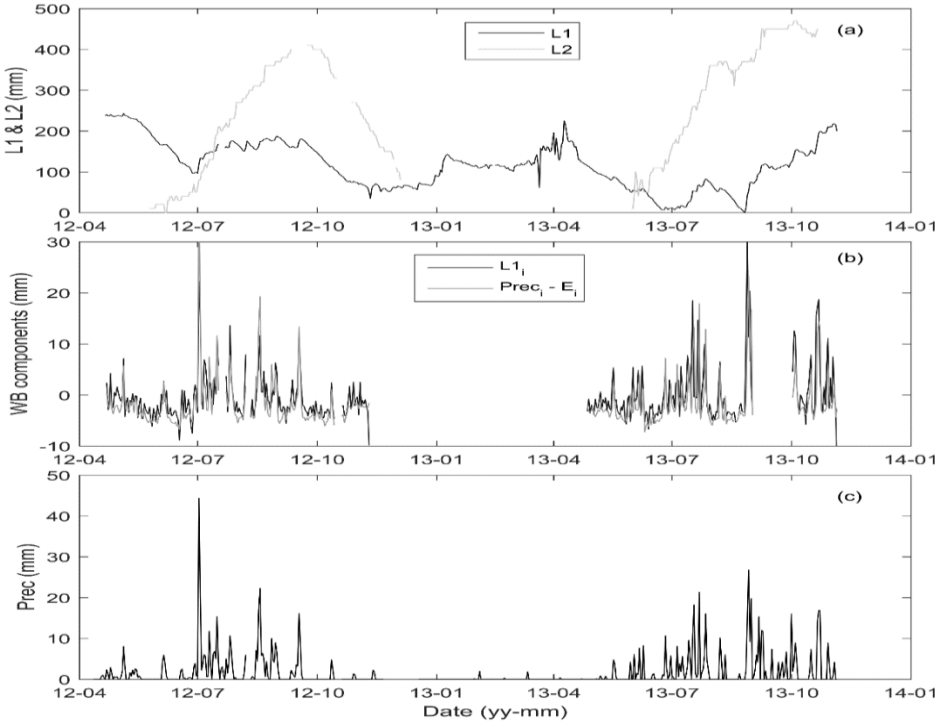

Figure 4.10 (a) Variations in daily water level changes in the small Nam Co lake ("L1") and Nam Co lake ("L2"); note that the reference water levels are different; (b) variations in water balance ("WB") components in small Nam Co lake: daily water level ("$\boldsymbol{L1_i}$") and difference between daily precipitation ("$\boldsymbol{Prec_i}$") and daily evaporation ("$\boldsymbol{E_i}$"); (c) variations in daily precipitation ("Prec").

The changes in the water level of Nam Co lake differ markedly from the changes in precipitation due to the large amount of water supplied through surface inflows by melting glaciers. Nevertheless, a significant influence of precipitation on the water levels of the "large lake" could be observed in the period with low precipitation (July 27th to August 26th in 2013 in Figure (4.10a)), when a slight drop in the water level (20 mm) occurred in the "large lake" while a significant drop (80 mm) in the water level was observed in the "small lake". Furthermore, the average evaporation (812 mm, (Wang et al. 2017)) during the open-water period of the "small lake" in 2012 and 2013 was much larger than the average precipitation (approximately 462 mm), while the water level changes were only approximately -190 mm and 20 mm during the two years. Strict data quality checking and cross-validation of the observations indicate that there exists groundwater supply from the surrounding water tables. Moreover, when considering the water budget over a complete year, the influence of groundwater supply is minor, and the summer water imbalance could be partly compensated

for by winter snowfall. Evidence of an distinct lake level rise (approximately 100 mm) during the winter of 2012 (Figure (4.10a)) was observed, although part of this rise was caused by volume increase through water-ice phase change. Therefore, the lake level rise in winter suggests a higher closure ratio of the water budget over a complete year. In addition, the phenomenon in which the water level rose in the "large lake" but fell in the "small lake" in June indicates a strong contribution of surface water inflow to the "large lake" from glacial melt (Zhu et al. 2010).

4.6.2 The uncertainties in energy budget of the "small lake"

The EBC value is generally high compared with the results of other energy budget studies (Nordbo et al. 2011). The EBC value is supported by the following reasons: the turbulent fluxes are based on eddy covariance measurements; observations that are contaminated by inadequate footprint, bad data quality or instrument errors are suitably interpolated over by optimized models and then validated through observations; and the observations of energy budget components are relatively complete over the two ice-free periods. Even so, several uncertainties still exist. 1) Due to the lake's environment and complex underwater bathymetry, the heat storage in the water and heat transfer between water and sediments is heterogeneous. For example, the heat storage estimated from shallow observations does not represent the heat storage of the whole lake. The imbalance of the energy budget on daily and monthly scales reflected by our observations suggests heat transfer through mixing or vertical heat exchange through the water-sediment interface. Further, the footprints of our measurements of eddy fluxes, radiation and water storage are not identical, and mismatches in these footprints will result in an apparent imbalance among energy budget components. However, such effects could be partly ameliorated for the whole ice-free period. 2) The eddy fluxes may be generally underestimated due to undetected large eddies (Foken et al. 2006). Vertical and horizontal advection may exist in the lake-land circulation, and this advection cannot be captured by EC instruments. Such effects may be strong for lakes with complex surrounding environments as in Nordbo et al. (2011), but should be relatively small for the homogeneous area surrounding the small lake examined in this study. 3) The "small lake", which has no inflow and no outflow, should dry out given that evaporation exceeds precipitation. Therefore, some water must be supplied by groundwater. Such an influx of water will lead to an energy budget imbalance, and it needs quantified by further water balance analysis. 4) The B method will overestimate *LE* when stable atmospheric conditions dominate over the water

surface (Wang et al. 2015). Although unstable and neutral atmospheric conditions dominate over the "small lake", stable atmospheric conditions may occur occasionally.

4.6.3 The uncertainties in energy budget of the "large lake"

The energy budget closure could reach 0.97 during the open water period of the "small lake" [*Wang et al.*, 2017] while it could be 0.859 during July to November with the observations of radiation budget, turbulent heat flux and heat storage with a water depth of 35 m. The EBC value is quite high compared with the results of other energy budget studies [*Nordbo et al.*, 2011; *Mammarella et al., 2015*]. The turbulent heat flux, solar radiation and water temperature observations have quite different footprints and these mismatches will introduce uncertainty in these energy budget components. In addition, the distribution of solar radiation, the latent heat flux and sensible heat flux should be horizontally heterogeneous [*Spence et al.*, 2011; *Wang et al.*, 2014]. Furthermore, the heat storage measured at a depth of 35 m in our study could only represent a good approximation. Water temperature at a depth of 35 m has obvious diurnal variations (with maximum amplitude of approximately 6 ℃ in its diurnal variation) and seasonal variations (to a maximum value of approximately 10 ℃), the heat transfer from water inflow, the heat stored in much deeper water, the heat transfer through horizontal advection and between water and sediment will all introduce uncertainty. In addition, sublimation during the winter period is none-zero over the "large lake", as a clear high *LE* during the ice-covered period could be observed by EC observation. Thus, the assumption of close to zero evaporation during the ice-covered period may not be the case.

4.7 Conclusions

The environmental factors controlling turbulent flux and energy budget over temporal scales of half-hourly, daily, and monthly were analyzed over the ice-free periods of the "small lake" and the "large lake" on the Tibetan Plateau. The bulk aerodynamic transfer method (in Chapter 3) is calibrated and used to interpolate turbulent heat flux values over periods when the measurements are inadequate or missing. Thus, continuous measurements over the ice-free periods are obtained for further evaporation and energy budget analysis. The main results are summarized as follows:

(1) The optimized parameters from observations collected in 2012 are adequate for observations in 2013, and it suggests adequate of B method for interpolating over missing or inadequate data, with monthly mean biases of

-2.2 ± 1.1 W m^{-2} in *H* and 11.2 ± 3.7 W m^{-2} in *LE* of the "small lake". Quite similarly, the turbulent heat flux simulation by B method in the "large lake" are as good as that in the "small lake", with a much lower MB values of 3.7 W m^{-2} and -2.8 W m^{-2}.

(2) The diurnal variations of *H* and *LE* have quite different patterns, with the former peaking in the early morning and the latter peaking in the afternoon. At half-hourly scales, wind speed shows an increasing trend in correlations with *H* from "extremely unstable" to "neutral" atmospheric conditions, while the contribution from temperature gradient is relatively stable ($R^2 = 0.4$). For *LE*, wind speed generally has a higher contribution while water vapor gradient shows almost no correlation under "near neutral" and "neutral" conditions. Generally, wind speed is most important at half-hourly scales, while temperature gradient and water vapor gradient are most important at daily and monthly scales.

(3) The evaporation over the "small lake" is approximately 812 mm, and the energy budget over the entire ice-free period is generally closed, with an estimated EBC value of approximately 0.97. For the "large lake", the evaporation over the ice-free season is around 981 ± 18 mm and the energy budget closure ratio during the observational period of July to November is 0.859.

(4) The water balance analysis with a much higher evaporation than precipitation with no inflow and outflow indicates that the "small lake" needs water supply by subsurface inflows.

Chapter 5 Comparison of boundary layer processes

5.1 Introduction

As the heat capacity in lakes with different areas, depths, meteorological and environmental conditions differ between small and large water bodies, they may lead to quite different phase shift of seasonal changes in meteorological variables and turbulent heat fluxes, and thus impacts on regional climate differently. Gao et al. (2009) found that momentum roughness lengths differ between coastal shallow water and open sea, and these coefficients should be parameterized differently. Wang et al. (2015) have also found that the Charnock number (see definition in Charnock (1955)) for deriving momentum roughness length is much higher in a small lake than the widely-used values in oceanic research. Panin et al. (2006) suggest that shallower lake depths could result in higher bulk transfer coefficients, and then larger lake-air turbulent heat flux. However, Venalainen et al. (1999) has found a larger evaporation rate for a larger water body due to its higher wind speed. Except the above issues, the thermal effect of sediments on water temperature in small and shallow lakes is appreciable while such effect could be neglected in large and deep lakes (Fang and Stefan 1996). Thus, how is the differences of lake-atmosphere transfer parameters, meteorological variables and turbulent heat flux between small and large water bodies, especially those locating closely and lying in same climatic background? Such related research and publications are quite limited world widely, and none exists over the high-elevation lakes of the Tibetan Plateau (TP).

Eddy covariance systems (listed in Nordbo et al. (2011)) have been applied over all kinds of lakes around the world (Granger and Hedstrom 2011; Liu et al. 2012; Tanny et al. 2008; Zhang and Liu 2014), and recently on several high-elevation lakes of the TP (Biermann et al. 2013; Li et al. 2016; Li et al. 2015a; Liu et al. 2014; Wang et al. 2017a; Wang et al. 2015; Wen et al. 2016). However, none[*] of the above papers have focused on the differences existing between small and large lakes due to the difficulty in measurements of these water bodies. In this Chapter, using EC observations in adjacent two lakes of the "small lake" (Wang et al. 2017; Wang et al. 2015) and the "large lake", we aim at two specific

[*] **This Chapter is based on the submitted manuscript:** Wang, B., Y. Ma, W. Ma, and Z. Su, Significant differences exist in lake-atmosphere interaction and evaporation in high-elevation of small and large lakes, Journal of Hydrology, **accepted**

objectives: (i) to illustrate clearly the differences existing in boundary layer parameters, meteorological conditions and turbulent heat fluxes of the two water bodies; (ii) to explain clearly why the evaporation in the "large lake" is larger than that in the "small lake". The objectives could address for the following general questions: (1) what differences exist between small and large water bodies in lake-atmosphere boundary layer processes; (2) whether evaporation estimated in smaller water bodies (i.e. Pan evaporation) are appropriate for evaluation of that in larger water bodies (i.e. lakes). Our conclusions could benefit the scientific research on catchment-scale energy budget and water balance analysis and lake modeling.

5.2 Materials and methods

5.2.1 Obtaining boundary layer parameters

The meteorological variables and bulk transfer coefficients have a height dependency. For example, a logarithm relationship between wind speed and height exists. Thus, after deriving z_{0m}, z_{0h} and z_{0q} using observations, U_z (m s^{-1}), T_z (℃) and q_z (kg kg^{-1}) should be corrected to a reference height of 10 m and neutral atmosphere for comparison. Further, the C_{Dz}, C_{Hz} and C_{Ez} obtained in the "small lake" and "large lake" should also be adjusted to conditions of neutral conditions and at a reference height of 10 m (C_{DN10}, C_{HN10}, C_{EN10}) (Andreas and Murphy 1986) using eq. (5.1 - 5.3):

$$C_{DN10} = \frac{k^2}{[kC_{Dz}^{-0.5} - \ln\left(\frac{z}{10}\right) + \Psi_m(\zeta)]^2} \tag{5.1}$$

$$C_{HN10} = \frac{kC_{DN10}^{0.5}}{kC_{Dz}^{0.5}C_{Hz}^{-1} - \ln\left(\frac{z}{10}\right) + \Psi_h(\zeta)} \tag{5.2}$$

$$C_{EN10} = \frac{kC_{DN10}^{0.5}}{kC_{Dz}^{0.5}C_{Ez}^{-1} - \ln\left(\frac{z}{10}\right) + \Psi_q(\zeta)} \tag{5.3}$$

Further, as roughness lengths show high sensitivity to measurement errors at small *H* and *LE*, turbulent heat flux smaller than 10 W m^{-2} are ignored to ensure data qualities of EC observations. Additionally, the following criteria are considered as abnormal range of roughness lengths: $\ln(z_{om}) < -15$ or $\ln(z_{om}) > -5$; $\ln(z_{oh}) < -15$ or $\ln(z_{oh}) > -3$; $\ln(z_{oq}) < -15$ or $\ln(z_{oq}) > -3$. Moreover, we emphasize that the EC observation after quality control are used in boundary layer parameters analysis in section 5.3.1 and the contaminated

EC values are substituted by simulations from bulk transfer method as in Chapter 4.

5.2.2 Parameterization schemes of roughness lengths

Table 5.1 Studied parameterization schemes for $\boldsymbol{z_{0m}}$, $\boldsymbol{z_{0h}}$ and $\boldsymbol{z_{0q}}$.

Methods	z_{0m}	z_{0h}	z_{0q}	Reference
UA	$z_{0m} = \alpha\frac{u_*^2}{g} + R_r\frac{v}{u_*}$	$ln\frac{z_{0m}}{z_{0h}} = 2.67Re_*^{0.25} - 2.57$	$z_{0q} = z_{0h}$	(Brutsaert 1982; Zeng et al. 1998)
CCM3	----	$z_{0h} = 2.2\times10^{-9}, \zeta > 0$ $z_{0h} = 4.9\times10^{-5}, \zeta < 0$	$z_{0q} = 9.5 * 10^{-5}$	(Large and Pond 1982; Zeng et al. 1998)
ECMWF	$z_{0m} = 0.018\frac{u_*^2}{g} + \frac{1.65\times10^{-6}}{u_*}$	$z_{0h} = \frac{6\times10^{-6}}{u_*}$	$z_{0q} = \frac{9.3\times10^{-6}}{u_*}$	*(Beljaars 1995; Zeng et al. 1998)*
NCEP	$z_{0m} = 0.014\frac{u_*^2}{g}$	$\ln\frac{z_{0m}}{z_{0h}} = \ln\frac{z_{0m}}{z_{0q}} = \frac{-1.076 + 0.7045\ln(Re_*) - 0.05808(lnRe_*)^2}{1 - 0.1954\ln(Re_*) + 0.009999(lnRe_*)^2}$		*(Zeng et al. 1998)*
GEOS	----	$\ln\frac{z_{0m}}{z_{0h}} = \ln\frac{z_{0m}}{z_{0q}} = 0.72(Re_* - 0.135)^{0.25}$		*(Zeng et al. 1998)*
VM	$\log_{10}(z_{0m}) = a_m + b_m\log_{10}(u_*^2/g)$, $a_m = -1.52;\ b_m = 1.4$	$z_{0h} = \frac{z_{0m}}{\exp\{a_h + b_h\log_{10}(Re_*)\}}$, $a_h = 0.38;\ b_h = 2.99$ $z_{0q} = \frac{z_{0m}}{\exp\{a_q + b_q\log_{10}(Re_*)\}}$, $a_q = 2.67;\ b_q = 2.6$		(Vickers and Mahrt 2010)
Notes: P1: $\alpha = 0.013$; $R_r = 0.11$ is "oceanic parameters"; P2: $\alpha = 0.031$; $R_r = 0.54$ is "optimized parameters".				

Roughness lengths for momentum, heat and water are important parameters in water-atmosphere turbulent transfer process and having reliable parameterization schemes of roughness lengths is still an open question for lakes on the TP. During the past several decades, various forms of roughness lengths parameterization schemes over water surface have been developed (Fairall et al. 1996b; Liu et al. 1979; Smith 1988; Vickers and Mahrt 2010). Parameterization schemes of momentum roughness length usually considers two situations: wind stress related rough flow (Charnock 1955; Smith 1988) and the viscosity related smooth flow. Right now, the most common used form is $z_{0m} = \alpha\frac{U_*^2}{g} + Rr\frac{v}{U_*}$. Where ν is kinematic viscosity of air ($m^2\ s^{-1}$), with a value of about 1.5×10^{-5} $m^2\ s^{-1}$ for atmosphere at the sea level and around 2.4×10^{-5} $m^2\ s^{-1}$ in the high-elevation Nam Co. The Charnock number (α) and roughness Reynolds number (R_r) are optimized considering the specific wave effect of the "small lake" (Wang et al. 2015). In this study, P1: $\alpha = 0.013;\ R_r = 0.11$ is considered as "optimized

parameters" while P2: $\alpha = 0.031$; $R_r = 0.54$ is "oceanic parameters". As the sensitivity of lake-air turbulent heat fluxes to the choice of roughness lengths' algorithms has been widely recognized (Webster and Lukas 1992), the different forms of roughness lengths in Table (5.1) (mainly from appendix of Zeng et al. (1998)) will be evaluated by our observations.

5.3 The differences existed in small and large lakes

5.3.1 Comparison of boundary layer parameters

5.3.1.1 Comparison of roughness lengths

The typical value of momentum roughness length (z_{0m}) in the "small lake" has been reported to be 3.35×10^{-4} m (Wang et al. 2015) while the value in the "large lake" is 80% higher (6.11×10^{-4} m) (Figure (5.1a)). z_{0m} in the "large lake" is quite close to the reported value (6.17×10^{-4} m) in another high-elevation lake of Ngoring (Li et al. 2015a), with an area of 610 km^2. The relatively higher z_{0m} in the "large lake" than in the "small lake" results from the higher wind speed and larger wind-induced waves. However, as the differences of z_{0m} in the two lakes are relatively minor that the optimized parameters (P2, $\alpha = 0.031$ & $\mathrm{Rr} = 0.54$ in UA method in Table (5.1)) of z_{0m} in the "small lake" (Wang et al. 2015) are also suitable to the "large lake", relative to the oceanic parameters (P1, $\alpha = 0.013$ & $\mathrm{Rr} = 0.11$) as in Figure (5.1a-b). The parameterization scheme with a combination of rough flow (α) and smooth flow (Rr) could improve z_{0m} at large U_* and small U_*, respectively. Thus, the combination form with optimized parameters (P2) not only shows better performance than the ones (e.g. UA and ECMWF) with oceanic parameters, but also perform better than the ones with only single item (e.g. NCEP, not shown in Figure (5.1)). The scheme of VM shows significant underestimation. Thus, the parameter scheme of combination form with optimized parameters will be used for z_{0m} simulation in the "large lake".

The peak of distribution of z_{0h} is much larger in the "small lake" than that in the "large lake", especially during the range of strong wind (Figure (5.1c-d) and Figure (5.2b)). The typical value of z_{0h}, 3.35×10^{-4} m in the "small lake", is one order of magnitude higher than the typical value (1.67×10^{-5} m) in the "large lake" (Figure (5.1b)). z_{0h} in the "large lake" is at same order of magnitude as the value (7.59×10^{-5} m) in lake Ngoring (Li et al. 2015a) and it is also close to the values from CCM3 and ECMWF (Table (5.1)). The parameterization

scheme of UA for z_{0h} is more suitable for the "small lake" than for the "large lake". The parameterization schemes of GEOS and VM are quite similar to UA, with a little lower value of GEOS scheme in small U_* and a little lower value of VM scheme in large U_*. The parameterization scheme of NCEP shows an overestimation of z_{0h}. All these parameterization schemes of z_{0h} are much suitable in the "small lake", but have an obvious overestimation in the "large lake". As parameterization scheme of UA shows similar shape as the observations, the UA form is optimized (constant value changing from -2.57 to -0.57) for sensible heat flux simulation in the "large lake".

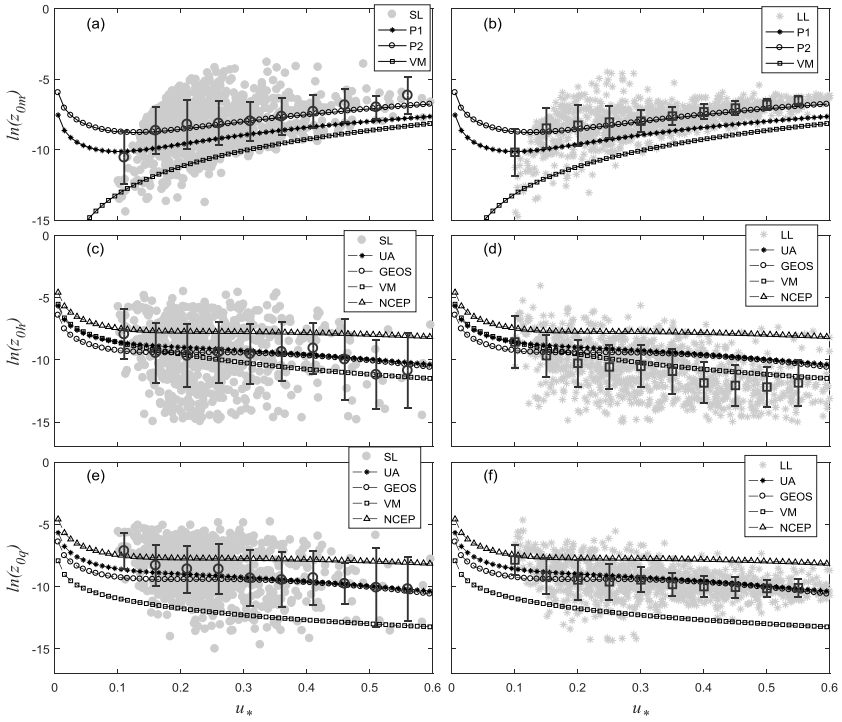

Figure 5.1 Comparison of roughness lengths for (a)-(b) momentum, (c)-(d) heat and (e)-(f) water and evaluation of the parameterization schemes in the "small lake" and the "large lake" respectively. "SL" indicates the observed roughness lengths in the "small lake", "LL" indicates the observed roughness lengths in the "large lake", the circles and the squares are the mean of observations for each binned $\boldsymbol{U}_*$ in the "small lake" and the "large lake", respectively (from 0.05 to 0.6 with a bin size of 0.05, error bas are marked), the lines indicates all kinds of parameterization schemes.

Similarly, the typical z_{0q} are 3.35×10^{-4} m in the "small lake" and 5.54×10^{-5} m in the "large lake"(Figure (5.1c)). And the latter is quite close to the observed value (6.73×10^{-5} m) in lake Ngoring (Li et al. 2015a). The parameterization schemes of UA and GEOS are quite similar, with the latter one

a little lower than the former at range of small U_*. The parameterization scheme of NCEP is overestimated while the parameterization scheme of VM is underestimated compared to the observations (Figure (5.1e-f)). Without optimization, the good performance of parameterization scheme of UA could be used for latent heat flux simulation in the "large lake". In a brief conclusion, the parameterization schemes of roughness lengths for momentum, heat and water should be evaluated before applied to the high-elevation lakes of TP and our results could provide reference values.

5.3.1.2 Comparison of bulk transfer coefficients

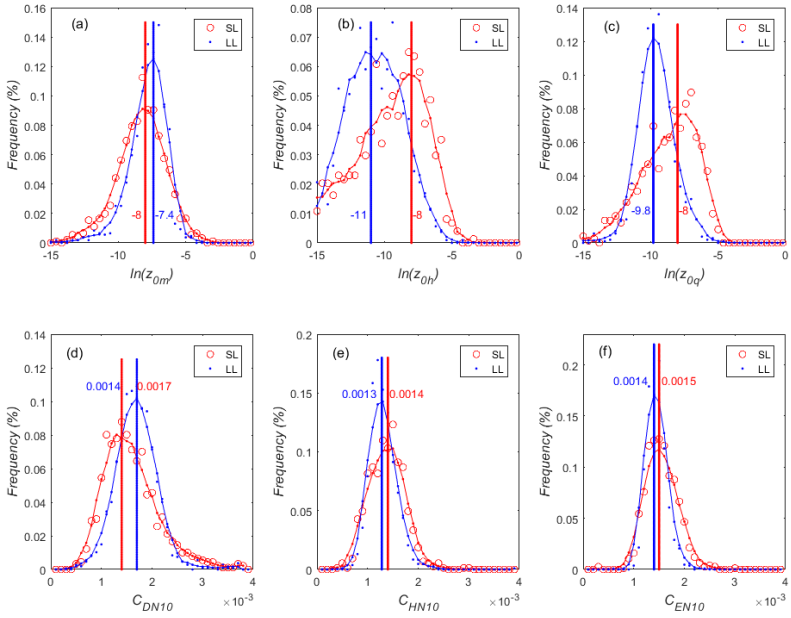

Figure 5.2 Statistical distributions of logarithm forms of (a) roughness length for momentum ($ln(z_{0m})$), (b) roughness length for heat ($ln(z_{0h})$), (c) roughness length for water vapor ($ln(z_{0q})$), (d) bulk transfer coefficients for momentum, (e) bulk transfer coefficient for heat, and (f) bulk transfer coefficient for water vapor, respectively. "SL" indicates the smoothed values in the "small lake", "LL" indicates the smoothed values in the "large lake". The values are also marked on each figures.

The bulk transfer coefficients for momentum (C_{Dz}) at observational heights of 2.75 m and 6 m are same (0.002) in the "small lake" and the "large lake", while the coefficients (C_{DN10}) corrected to a reference height of 10 m and neutral conditions are 0.0014 and 0.0017, respectively (Figure (5.2d)). The larger C_{DN10} in the "large lake" may result from the combined effects of larger wind-induced waves and complex basin environments (i.e. huge stones in the water). The C_{DN10}

in the "small lake" (0.0014) is quite close to the value (0.00149) in the leads and polynyas of polar oceans (Andreas and Murphy 1986), with both higher than the reported open-ocean values of around 0.0012 at medium range of wind speed (Large and Pond 1981). Because of the limited wind fetch, the upwind edges of grassland and the growing wave field in the "small lake" may attribute to the larger form drag than the open oceans. However, the even larger C_{DN10} (0.0017) in the "large lake" could only be ascribed to the large wind induced waves (Wu 1980).

The bulk transfer coefficients for heat (C_{HN10}) at a height of 10 m and neutral conditions are 0.0014 and 0.0013 (Figure (5.2e)) in the "small lake" and the "large lake" while the bulk transfer coefficients for water (C_{EN10}) are 0.0015 and 0.0014, respectively (Figure (5.2f)). These coefficients are about 7% lower in the "large lake". And these estimated C_{HN10} and C_{EN10} are all larger than the published typical oceanic value of 0.0012 (Smith 1989; Zeng et al. 1998). The larger scatter in the range of small U_* in the "small lake" than in the "large lake" may result from the relative higher measurement uncertainties under free convection events (Figure (5.1)).

5.3.2 Comparison of meteorological variables and turbulent heat flux

The seasonal variations of meteorological variables and turbulent heat flux during observational periods of 2015 and 2016 in the "large lake" are shown in Figure (5.3) and details of those in the "small lake" could be found in Chapter 4. Further, all the above observations have been summarized in Figure (5.4) for comparison. Similar to the "small lake", daily T_a and E_a are generally smaller than daily T_s and E_s in the "large lake", especially during the cooling period (Figure (5.3a-b)). Daily water surface temperature (T_s) could be about 13℃ at the beginning of September in the "large lake" (12.3 ℃ during September 9, 2015 and 12.9 ℃ during September 2, 2016 in Figure (6a)) while it could reach to approximately 16℃ during the middle of June (15.7 ℃ during June 15, 2012 and 15.9 ℃ during June 21, 2013) in the "small lake". The average wind speed (corrected to a reference height of 10 m) is about 3.65 m s^{-1} during July through November in the "small lake" while it is 4.71 m s^{-1} (corrected at a reference height of 10 m) in the "large lake" (Figure (5.3c)). Thus, clearly higher wind speeds in the "large lake" than those in the "small lake" could be observed (Figure (5.4c)). Similar as in the "small lake", unstable atmosphere also dominates in the "large lake" (Figure (5.3d)). The vapor pressures of air in both lakes reach their highest values in July and then decrease afterwards (Figure (5.4d)). Because of the relatively

higher wind speed and lower T_s in the "large lake", the atmosphere shows less unstable compared with that in the "small lake". Moreover, because of the strong "warm lake effect" in the "large lake" (Lv 2008), the annual average air temperature (1.9 ℃, in 2016) is obviously higher in the "large lake", compared with multiple year average of air temperature (0 ℃) in the Nam Co station. Moreover, monthly average air temperature (T_a) is clearly higher in the "large lake" than that in the "small lake" (Figure (5.4b)). Relative to the "small lake", the large thermal capacity in the "large lake" could also lead to late date of peak value of monthly T_s, slow decreasing rate of T_s (Figure (5.4a)) and thus late dates of ice frozen and ice melt. In addition, monthly average T_a decrease much slower in the "large lake".

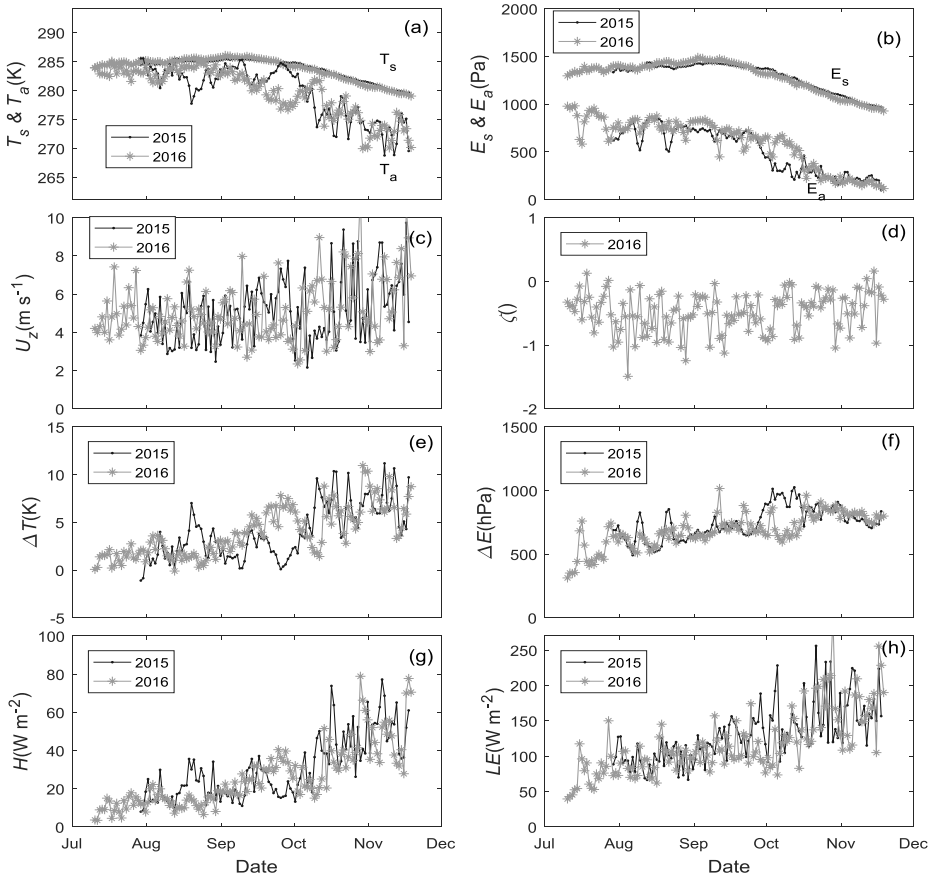

Figure 5.3 Variation of daily (a) $\boldsymbol{T_s}$ & $\boldsymbol{T_a}$; (b) $\boldsymbol{E_s}$ & $\boldsymbol{E_a}$; (c) $\boldsymbol{U_z}$; (d) $\boldsymbol{\zeta}$; (e) $\boldsymbol{\Delta T}$; (f) $\boldsymbol{\Delta E}$, (g) *H*, (h) *LE* during July to November in 2015 and 2016.

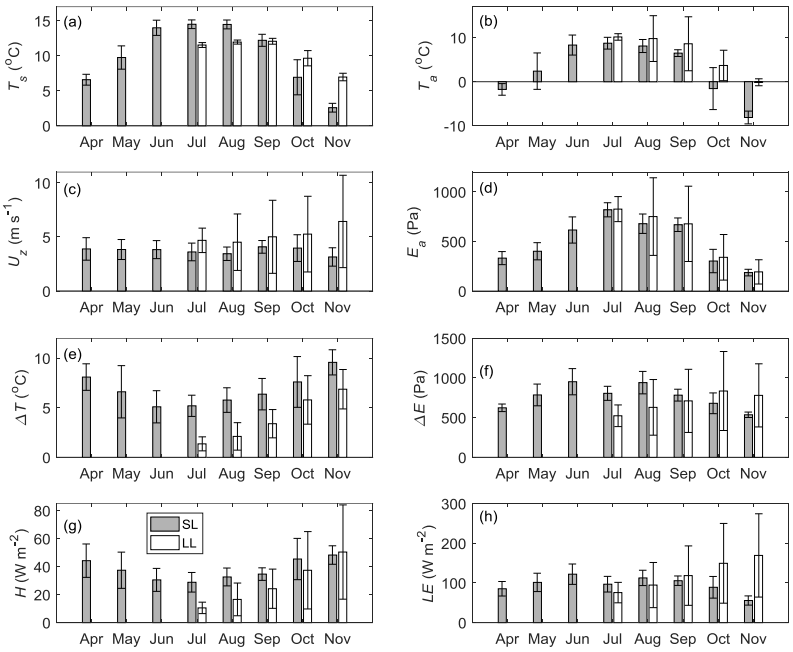

Figure 5.4 Comparison of (a) water surface temperature (T_s), (b) air temperature (T_a), (c) wind speed (U_z), (d) vapor pressure of the air (E_a), (e) temperature gradients (ΔT), (f) water vapor gradients (ΔE), (g) sensible heat flux (H), (h) latent heat flux (LE) between the "small lake" (SL) and the "large lake"(LL).

Daily H and LE in the "large lake" both show increasing trends from July to November (Figure (5.4g-h)), during when daily ΔT and daily ΔE between water and air also show increasing trends (Figure (5.4e-f)), besides the clearly increasing trend of daily U_z from September to November (Figure (5.4c)). The variation of daily H are similar to that of daily ΔT while the variation of daily LE is more similar to daily U_z than daily ΔE. For example, in October 2015, high daily ΔE and low daily LE exist (Figure (5.3f-h)). The relative contributions of meteorological variables to turbulent heat flux could resort to Chapter 4. Influenced by the large thermal capacity of the "large lake" and the strong land-lake breeze circulation, the monthly averaged ΔT is much higher in the "small lake" than in the "large lake" (Figure (5.4e)). Thus, the monthly averaged H are generally higher in the "small lake" than those in the "large lake", except in November, during when the significantly high U_z in the "large lake" play a dominant contribution (Figure (5.4c-g)). Variations of monthly LE and ΔE show quite different patterns in the two lakes, and they are higher for July and August

and lower for October and November in the "small lake", compared to those in the "large lake" (Figure (5.4f-h)).

5.4 Discussions

5.4.1 The reasons for the observed differences in meteorological variables

The inherent attributes and environmental backgrounds of the two adjacent water bodies could explain most of the observed differences. (i) The higher wind speed in the "large lake" may result from the smooth water surface compared with the land-dominated "small lake" area (Granger and Hedstrom 2011). In addition, the bowl shaped terrain in the "small lake" area may form a specific internal boundary layer conditions different from the flat area of the "large lake". (ii) Daily T_s could be approximately 3 ℃ smaller in the "large lake" than that in the "small lake", because of the facts that solar heating could be distributed in deeper depth of the "large lake" than that in the "small lake". More specifically, the "large lake" has the characteristics of (1) a larger Secchi depth, and thus more transparent to solar radiation and more solar radiation stored in the water; (2) a stronger turbulence exchange intensity and thus much easier to transfer heat into deep water; (3) a deeper depth and thus a higher potential for storing heat. (iii) Because of the larger heat capacity in the "large lake", phenomenon of warm air temperature, slow decreasing rate of air temperature, and delayed peak value of *H* and *LE* exist. (iv) The precipitation in the lake-dominated environment with a value of around 300 mm in 2016 is much smaller than the climatic average over the land-dominated environment of "small lake", which is mainly driven by the land breeze and land surface interaction, thus has higher precipitation than that over the lake-dominated environment (Gerken et al. 2015). (v) The ice-free period of the "small lake" lasts from April to November while it is from May to January in the "large lake" according to satellite observations (Kropáček et al. 2013). We have also observed large values of *H* and *LE* in January 2017 and this phenomenon corresponds to the observed large water-air temperature gradients in leads and polynyas of the polar oceans (Andreas and Murphy 1986). Thus, even in the same climatic area, the meteorological variables and turbulent heat flux show significant differences in its seasonal variations. (vi) Similar as those low-latitude tropical lakes (*Verburg and Antenucci, 2010*), high-elevation lakes show dominance in unstable and neutral atmospheric conditions in these two lakes and some other lakes, i.e., Lake Qinghai (*Li et al., 2016*), Lake Serling Co (Guo et al., 2016), and Lake Ngoring (Li et al., 2015). The unstable atmosphere

conditions in high-elevation lakes and tropical lakes result from the higher solar radiation and radiation-induced positive water-air temperature gradients compared to the temperate low-elevation lakes. More discussion on influences of these characteristics to turbulent heat fluxes could resort to *Verburg and Antenucci,* (*2010*).

5.4.2 The uncertainties in evaporations and its influence

The EC-based evaporation in the "large lake" (630 mm during July to November) is much higher than the reported value (392 mm) in Lake Ngoring during July to November [Li et al., 2015a], and the amounts of R_n, 169.5 W m^{-2} higher in the "large lake", could explain most of the differences. The estimated evaporation during May to January (approximately 981 ± 18 mm) of the "large lake" is also higher than the simulated results from the Flake model [Lazhu et al., 2016] and the CRLE model [Ma et al., 2016]. Both the uncertainties in the input meteorological data and the unsuitable parameterization schemes of the models could lead to such bias, and our results could provide valuable data for future validation and evaluation of these models. The ratio of evaporation (981 ± 18) to rainfall (505 mm) is 1.9 in this study, while they are 3.5 (with evaporation and precipitation values of 1430 mm and 420 mm, respectively) in Zhu et al., [2010] and 1.2 (with evaporation and precipitation values of 603 mm and 505 mm, respectively) in Zhou et al., [2013]. Zhu et al.[2010] conclude that underground water or other sources are needed to complement the huge evaporation, while Zhou et al.[2013] suggest that water seepage exists. Except for the other differences in their estimated precipitation and runoff values and runoff coefficients, the EC-based evaporation value of 981 ± 18 mm could improve the understanding of their conclusions in a water imbalance analysis.

The uncertainties in the estimated evaporation of 981 ± 18 mm should result from the uncertainties existing in Bo and R_n. First, assuming the heat stored in the water after ice-melt will all be released before ice-frozen, LE could be expressed as $LE = \frac{R_n}{(1+Bo)}$. Thus, lake evaporation is positive correlated with R_n and negative correlated with *Bo*. The sum of R_n during the open water period of the "small lake" (with a value of 1167.9 W m^{-2} in Table 4 of Wang et.al. [2017]) is quite close to the sum of R_n during the open water period of the "large lake" (1164 W m^{-2} in Table 6). The estimated lower *Bo* in the "large lake" than in the "small lake" indicate a higher evaporation value in the former. Average Bo without consideration of its seasonal variation in this study may introduce some uncertainties. For example, a warmer air temperature than water surface

temperature in the "large lake" may form during May and June according to satellite and AWS observations, similar to the observations in Lake Serling [Guo et al., 2016], and smaller Bo in May and June and larger Bo in December and January may exist. The estimated evaporation through EC-based Bo value of 0.229 (close to the Bo value in September) could only repreesnt a rough estimation.

Further, we used ice phenology to estimate the lower and upper boundaries of the open water evaporation in the "large lake". The average dates of freeze onset (FO, the date when detectable ice appears), freeze-up (FU, the date when the surface is fully ice covered), break-up (BU, the date when detectable ice-free water appears) and water clean of ice (WCI, the date when ice all disappears) are 4th January, 13th February, 4th April and 15th May, respectively by satellite observations [Kropáček et al., 2013]. The duration from FU to BU is longer in three adjacent small lakes (Lake Ringco Ogma, Lake Npen Co and Lake Bam Co) relative to Lake Nam-Co. The estimated evaporation values through R_n and Bo are 885 $\pm$17 mm during FU to BU and 1137$\pm$21 mm during FO to WCI, and our estimation during May to January is just in between.

5.5 Conclusions

Using eddy covariance observations in the "small lake" and the "large lake" over the TP, significant differences of lake-atmosphere boundary layer parameters, meteorological variables and turbulent heat fluxes are reported.

(1) Relative to the "small lake", the "large lake" has larger depth and area, thus a larger thermal capacity, which could further lead to delayed ice-formation and ice-melt dates, postponed peaks of seasonal variation of water surface temperature, air temperature, sensible heat flux and latent heat flux. In addition, the "large lake" has a lower water surface temperature, because of its more transparent to solar radiation, larger mixing layer depth and stronger turbulent mixing intensity in the water.

(2) The roughness length and bulk transfer coefficients for momentum are 80% and 7% higher in the "large lake" than those in the "small lake" because of its larger wind speed and higher wind-induced waves. The roughness lengths for heat and water of the "large lake" are about one order of magnitude lower than those in the "small lake" while the bulk transfer coefficients for heat and water at a height of 10 m and neutral condition show 7% lower value in the

"large lake". Thus, parameterization schemes for these coefficients should differ between small lakes and large lakes in numerical climate modeling.

(3) The total evaporation during ice-free period of the "large lake" is estimated to be around 981 ± 18 mm during May to January, which is higher than the value of 812 mm from April to November in the "small lake". The much higher evaporation in the "large lake" is mainly related to the observed lower Bowen ratio in the "large lake". The large discrepancy between our results and published model simulations suggest the need for an thorough evaluation of models' parameterization schemes over the high-elevation lakes.

Chapter 6 Evaluation of lakes' response to climate change

6.1 Introduction

Under global climate warming, trends of increasing numbers of lakes, growing lakes and rising lake levels are widely observed in the central TP due to increased precipitation, accelerated glacial melt and permafrost ablation (Lei et al. 2013; Yang et al. 2014; Yao et al. 2004; Zhang et al. 2011b). The climate of the TP has also shown warming and moistening of the air, solar dimming, and wind stilling since the 1980s (Yang et al. 2014), and a generally decreasing trend in Pan evaporation (Liu et al. 2004). Evaporation from Nam Co lake has shown an increase in simulations based on the Flake (Fresh water lake) model (Lazhu et al. 2016), but a slight decrease in estimations with the Complementary Relationship Lake Evaporation (CRLE) method (Ma et al. 2016). Lake warming over Nam Co during 1979-2012 has recently been reported by General Lake Model simulations (Huang et al. 2017). However, by Flake simulation over two lakes of Ngoring and Gyaring in the northern plateau, Kirillin et al. (2017) found no clear trends in modeled mean lake temperatures and concluded no significant warming trends in this area. Thus, before application of these models to the lakes on the TP, the parameterization schemes and simulation results need a thorough evaluation using in-situ observations, for which we have found that the constants for parameterizing momentum roughness length are different from the values in oceanic research (Wang et al. 2015).

Further, amongst all the physical-based lake models (Perroud et al. 2009; Stepanenko et al. 2014b; Thiery et al. 2014b), Flake* has advantages of physically sound and computational efficient, thus shows high potential to be integrated in numerical weather prediction models (Mironov 2008). The Flake model has been applied over all kinds of different environments (Dutra et al. 2010; Kirillin et al. 2017; Lazhu et al. 2016; Stepanenko et al. 2014a; Thiery et al. 2014a; Thiery et al. 2014b; Zolfaghari et al. 2017). It could reproduce the observed mixed layer seasonality and has also shown capability of reproducing the temperature

---

* **This chapter is based on the paper and the submitted manuscript:**
Wang, B., Y. Ma, W. Ma, Z. Su, and X. Dong, Evaluation of ten methods for estimating evaporation in a small high-elevation lake on the Tibetan Plateau, Theor Appl Climatol, 2018, NaN(NaN-NaN), DOI: 10.1007/s00704-018-2539-9;
Wang, B., Y. Ma, Y. Wang, W. Ma, and Z. Su, Driving forces behind lakes' response to climate change by Flake simulation in Nam Co, In preparation for submission.

distribution with acceptable accuracy (Kirillin et al. 2017; Lazhu et al. 2016; Perroud et al. 2009; Thiery et al. 2014a; Vörös et al. 2010). However, most of the above mentioned research value the surrounding land-dominated meteorological observations and mainly focus on the evaluations of water surface temperature at temporal scales of daily and longer.

In this Chapter, to evaluate lakes' responses to climate change in this data scant area of the vast high-elevation lake zone, we evaluated the trends of evaporation through two ways of lake modeling using in-situ observations: 1) traditional evaporation methods in the "small lake"; 2) Flake modeling in the "small lake" and in the "large lake".

In the 1) part, 10 traditional evaporation estimation methods (including 2 radiation-based methods, 2 Dalton type methods and 6 energy-budget-based methods) were evaluated by the validation dataset. And the objectives of the study were (1) to evaluate the performance of these traditional evaporation methods at a temporal resolution of 10 days over the "small lake" and (2) to obtain inter-annual variations in lake evaporation during the open-water period of 1979-2015. The data and methods are briefly introduced in section 6.2.1 and the results are given in section 6.3.

In the 2) part, we attribute our efforts to the following questions: 1, How are the performances of Flake model on the simulated thermal structure, water surface temperature and turbulent heat flux in the "small lake" and the "large lake", not only at temporal resolutions of daily and longer, but also at shorter temporal resolution of diurnal? 2, Whether significant differences exist in the simulations between land-dominant forcing and lake-dominant forcing in the "large lake"? 3, What are the driving forces for the long-term trends of simulated water surface temperature and turbulent heat flux in the "large lake"? To investigate the aforementioned questions, we combine in-situ observations (including: water surface temperature, meteorological variables and eddy covariance (EC) observations in the "small lake" (Wang et al. 2015); water temperature profiles, meteorological variables and EC observations in the "large lake"; land-dominated meteorological variables in the Nam Co station (Ma et al. 2009)), long term ITP forcing data during 1979-2015 (He and Yang 2011) and one-dimensional Flake model (Mironov 2008). The Flake model is illustrated in section 6.2.2 and the results are shown in section 6.4.

6.2 Materials and methods

6.2.1 Traditional evaporation method

Ten evaporation methods were evaluated and ranked using observations at a temporal resolution of 10 days (Table (6.1)). The Penman (1948) method (**PE**) has been widely used for estimation of evaporation. It combines equilibrium evaporation (a lower limit evaporation from moist surfaces) and a measure of the departure from equilibrium in the atmosphere (in other words, the drying power of the air). When the air over a moist surface is vapor-saturated and the variations in temperature and vapor pressure with height and time are small, the Priestley and Taylor (1972) method (**PT**) is used to take the equilibrium evaporation for estimating potential evaporation under a condition of minimal advection; the Priestley-Taylor constant is $\alpha_1 = 1.26$. The Brutsaert and Stricker (1979) method (**BS**) is based on Bouchet's hypothesis ($E = 2E_w - E_p$), with E_w estimated by the **PT** method and E_p estimated by the **PE** method. Similarly, the De Bruin (1978) method (**de**) eliminates the energy budget part in the **PT** and **PE** methods and relates evaporation to the drying power of the air. The Bowen-ratio-energy-budget method (**BREB**) was first presented by Bowen (1926) and has been widely used for estimation and validation of evaporation over wet surfaces (Brutsaert 1982; Drexler et al. 2004; Rosenberry et al. 2007; Winter et al. 1995). The Bowen ratio (*Bo*) is expressed as $Bo = \gamma \frac{(T_s - T_a)}{(E_s - E_a)}$ through observations of temperature and vapor pressure at two heights. Noted that the energy due to subsurface inflow and outflow and heat transfer in the sediment are ignored in our study due to limitations in the observational data. The DeBruin and Keijman (1979) method (**DK**) introduces an observational relationship between $\frac{\gamma}{s}$ and *Bo* from Hicks and Hess (1977), where γ is a psychrometric constant and s is the slope of the saturated vapor pressure-temperature curve at mean air temperature (Allen et al. 1998). Many other formulas exist for estimation of evaporation based on only air and water parameters (MaGuinness and Bordne 1972; Singh and Xu 1997). These methods have various forms and constants that are site-dependent and require calibration. Because model complexity cannot improve simulation performance (Singh and Xu 1997; Xu and Singh 2001), two solar-radiation-based methods (the Jensen-Haise and Makkink methods, **JH** and **Mak** for short) and two Dalton-type methods (the Ryan-Harleman and Dalton methods, **RH** and **DM** for short) were chosen in our study. The input meteorological variables for the methods are average values over ten days, and the outputs of the evaporation

simulations were converted to mm d^{-1} using relevant constants. All the equations and variables are listed and explained in Table 6.1.

Table 6.1 Methods for estimating evaporation (E in **mm d^{-1}**).

Method	Equation
PE	$E = \frac{s}{s+\gamma}\frac{(R_n - G_s)}{L_e\rho_w} \times 86.4 + \frac{\gamma}{s+\gamma}(0.26(0.5 + 0.54U_z)(E_{as} - E_a))$
PT	$E = \alpha\frac{s}{s+\gamma}\frac{R_n - G_s}{L_e\rho_w} \times 86.4$
BS	$E = (2\alpha_1 - 1)\left(\frac{s}{s+\gamma}\right)\left(\frac{R_n - G_s}{L_e\rho_w}\right) \times 86.4 - \frac{\gamma}{s+\gamma}0.26(0.5 + 0.54U_z)(E_{as} - E_a)$
De	$E = \left(\frac{\alpha}{\alpha - 1}\right)\left(\frac{\gamma}{s+\gamma}\right)\frac{(de_1 + de_2U_z)(E_{as} - E_a)}{L_e\rho_w} \times 86.4$
BREB	$E = \frac{R_n - G_s}{(1+Bo)L_e\rho_w} \times 86.4$
DK	$E = \frac{s}{0.85s + 0.63\gamma}\frac{R_n - G_s}{L_e\rho_w} \times 86.4$
JH	$E = (JH_1T_a + JH_2)(R_{s\downarrow} \times 3.523 \times 10^{-2})$
Mak	$E = (\left(Mak_1\frac{s}{s+\gamma}\frac{R_{s\downarrow}}{L_e\rho_w}\right) - 0.12)$
RH	$E = RH_1\frac{(2.7(T_s - T_a)^{0.333} + 3.1U_z)(E_s - E_a)}{L_e\rho_w} \times 86.4$
DM	$E = \left(NU_2(E_s - E_a)\right) \times 10$

E, evaporation mm d^{-1};
$Bo = \gamma\frac{(T_s - T_a)}{(E_s - E_a)}$ is the Bowen ratio; γ, psychrometric constant (depends on temperature and atmosphere pressure) (Pa ℃) and $\gamma = \frac{C_pP}{\varepsilon_1 L_v}$, where C_p is specific heat at constant pressure (1.013 MJ kg^{-1}℃$^{-1}$), P is atmospheric pressure (kPa), $\varepsilon_1 = 0.622$ is the ratio of molecular weight of water vapour to that of dry air, and L_v is the latent heat of vaporization (2.45 MJ kg^{-1}); T_s, water surface temperature, ℃; T_a, air temperature (℃, with unit of °F in JH method);
s, slope of the saturated vapour pressure-temperature curve at mean air temperature (kPa ℃) and $s = \frac{4098[0.6108exp(\frac{17.27T_a}{T_a + 273.15})]}{(T_a + 273.15)^2}$;

R_n, net radiation (equal to $R_{s\downarrow} - R_{s\uparrow} + R_{l\downarrow} - R_{l\uparrow}$, W m^{-2}), $R_{s\downarrow}$, incoming solar shortwave radiation (W m^{-2}), $R_{s\uparrow}$, reflected solar shortwave radiation (W m^{-2}), $R_{l\downarrow}$, incoming atmospheric longwave radiation (W m^{-2}), $R_{l\uparrow}$, longwave radiation emitted from the water surface (W m^{-2});
G_s, heat storage in the water body (W m^{-2});
ρ_w, density of water (998 kg m^{-3} at 20 ℃);
E_{as} and E_a are saturated vapour pressure (hPa) and actual vapour pressure (hPa), respectively;
α_1, Priestley-Taylor empirically derived constant, dimensionless, $\alpha_1 = 1.26$;
N, mass-transfer coefficients; *N* is 0.0164 as in *Rosenberry* et al.[2007] and it is 0.0133 after calibration;
$de_1 = 2.9$ and $de_2 = 2.1$ in the original equation, and they are 21 and -0.47, respectively, after calibration;
$JH_1 = 0.014$ and $JH_2 = -0.37$ in the original equation, and they are 0.0045 and 0.2, respectively, after calibration;
$Mak_1 = 52.6$ in the original equation and is 56.5 after calibration;
RH_1 are 1 in the original equation and 0.856 after calibration.
The multipliers of 86.4 and 10 that appear in equations are used to convert the output into mm d^{-1}.

6.2.1.1 Methods for calibration and validation

The constants in several methods of Table (6.1) can be calibrated using observations, including de_1 and de_2 in the **de** method, JH_1 and JH_2 in the **JH** method, Mak_1 in the **Mak** method, RH_1 in the **RH** method, and N in the **DM** method. Eddy-covariance based reference datasets and meteorological observations are used to optimize these constants. The **PE**, **PT** and **BS** methods were developed gradually and are widely applied to all types of environments. In addition, the contribution to evaporation from the wind function in the **PE** and **BS** methods is small (approximately 21%). Thus, the constants in the **PE** and **BS** methods and the well-known Priestley-Taylor constant in the **PT** method remain unchanged. Similar situations exist for the **BREB** and **DK** methods. To quantitatively analyze the difference between model simulations and observations, we used the correlation coefficient (R), the mean absolute error (MAE), the relative error (RE) and the root-mean-square error (RMSE) defined in section 2.4.

6.2.1.2 Validation datasets at a temporal resolution of 10 days

The latent heat flux (*LE*) and sensible heat flux (*H*) were obtained through standard processing of eddy covariance data, and a bulk aerodynamic transfer model was optimized for interpolation of *LE* and *H* in case of an inadequate footprint and malfunctioning of the instruments (Wang et al. 2017; Wang et al.

2015). The meteorological variables and energy budget components were subject to strict selection. The heat storage in the water is assumed to be the residual of the energy budget components ($G_s = R_n - LE - H$). The temperature and vapor pressure over the water surface were higher than those in the air (Figure (6.1a-b)) and the average wind speed was 3.46 m s^{-1} (Figure (6.1c)). An unstable and neutral atmosphere, which has been reported at several high-elevation lakes (Li et al. 2015b; Liu et al. 2014; Wang et al. 2015; Wen et al. 2016), dominates the small Nam Co lake. The solar radiation in May and June of 2013 was disregarded because of stringent quality criteria (Figure (6.1d)). The evaporation throughout the ice-free period was approximately 812 mm, and the energy budget was generally closed with a closure ratio of 0.97 (Wang et al. 2017).

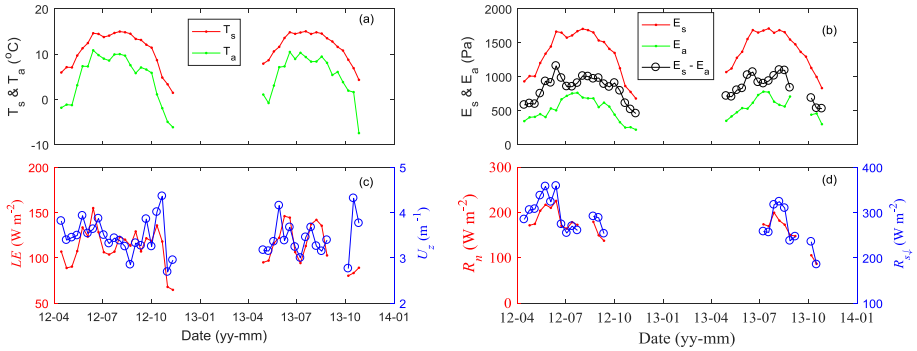

Figure 6.1 Variations in (a) temperature at the water surface ($\boldsymbol{T_s}$) and in the air ($\boldsymbol{T_a}$); (b) vapour pressure at the water surface ($\boldsymbol{E_s}$) and in the air ($\boldsymbol{E_a}$), and vapour pressure difference ($\boldsymbol{E_s - E_a}$); (c) *LE* and wind speed ($\boldsymbol{U_z}$); (d) net radiation ($\boldsymbol{R_n}$) and downward shortwave radiation ($\boldsymbol{R_{s\downarrow}}$) at a temporal resolution of 10 days.

6.2.2 Flake modeling

Flake model is a one-dimensional bulk model and divides the water column into two layers, a mixed layer with a uniform temperature distribution near the upper surface and a thermocline layer for describing the lower stratified water down to the lake bottom, in which "self-similarity" concept of the non-dimensional temperature-depth curve is used (Kirillin et al. 2017; Mironov 2008). Under this concept, the vertical temperature profile described by the shape factor of thermocline should satisfy the specific heat transfer equation of the water, where heat flux due to solar radiation could penetrate into the water following the Beer-Lambert law (Stepanenko et al. 2014a). Mixed-layer depth resulting from convection entrainment and wind-driven mixing are solved through an entrainment equation and a diagnostic equation respectively (Mironov 2008; Zilitinkevich and Mironov 1996). The surface scheme of turbulent heat flux

follows the classic Monin-Obukhov similarity theory, where the constants for momentum roughness length are set to be 0.031 and 0.54, respectively (Wang et al. 2015). In addition, the temperature profiles in the snow, ice and bottom sediment are all solved following the same concept, with different parameterization schemes of shape factor used. The detailed illustration of the Flake model could be found in Mironov (2008).

6.2.2.1 Mixed-layer depth and its variations

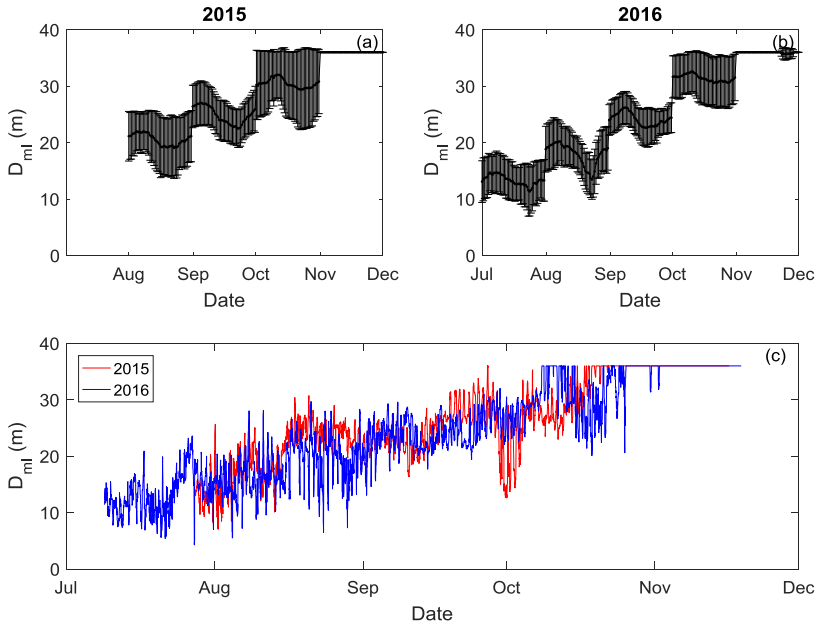

Figure 6.2 The diurnal variation of monthly average mixed layer depth in 2015 (a) and in 2016 (b); the seasonal variation of half-hourly mixed layer depth for 2015 and 2016.

The mixed-layer depth in the "large lake" is estimated by threshold method using temperature profile observations. Firstly, the temperature observations are interpolated at a spatial resolution of 0.1 m to a depth of 36 m (T_i) using spline method. After that, to remove the strong warm layer and cool layer effect at the surface, the average value of interpolated temperature to a depth of 4 m is permanently considered as mixed-layer temperature (T_{ml}) during observation period of July to November. Lastly, the depth, where the temperature gradient between T_{ml} and T_i is larger than 1 ℃, is considered as the base of the mixed-layer. In addition, if the temperature gradient at all depths are smaller than 1 ℃, the mixed-layer depth will be 35 m.

Firstly, we test the estimated mixed-layer depth with that by the published Optimal Linear Fitting Method (OLFM, (Chu and Fan 2011)), and the seasonal variations of mixed-layer depth are quite similar. The threshold method approaches more close to the observed mixed-layer depth relative to that by OLFM method, which shows a slightly overestimation due to the course spatial resolution of observations (Thomson and Fine 2003). The diurnal and seasonal variations of observed mixed layer depth are shown in Figure (6.2). The diurnal variations of mixed-layer depth are quite obvious during July to October while the whole water column is fully mixed in November. The mixed-layer depth decreases after sunrise, reach to its smallest value before sunset and then increase afterwards. The diurnal variations of mixed-layer depth result from the characteristics of solar heating during the day and surface cooling at night, which will inhibit/promote variations of mixed-layer depth respectively. On its seasonal variation, the mixed-layer depth increase from around 10 m in July to the deepest observation depth of 35 m in the middle of October. The largest amplitude of diurnal mixed-layer depth could be around 18 m on August 2 2015 and around 19 m on July 27th 2016. The average values of mixed layer amplitude are 7.2 m and 8.8 m in 2015 and 2016 respectively and its seasonal variations provide good validation dataset for the mixing process in Flake modeling.

6.3 Evaluation of traditional evaporation methods

6.3.1 Evaluation of parameters

The Bowen ratio (*Bo*) has high significance among the energy budget methods for estimation of evaporation and it has also been related to $\frac{\gamma}{s}$ using the equations (a) $Bo = 0.79\,\gamma/s - 0.21$ (**PT** and **BREB**) and (b) $Bo = 0.63\,\gamma/s - 0.15$ (**DK** and **BREB**) (Hicks and Hess 1977). *Bo* from eddy covariance observations (*H*/*LE*) and traditional meteorological observations ($\gamma \frac{(T_s - T_a)}{(E_s - E_a)}$) at a temporal resolution of 30 minutes is quite close to the 1:1 line (Figure (6.3a)), which supports the similarity of eddy transfer coefficients for heat and water in atmosphere boundary layer. Furthermore, it shows good consistency using reconstructed heat fluxes and meteorological variables at a temporal resolution of 10 days (Figure (6.3b)). Thus, energy budget methods based on *Bo* perform well (Table (6.2)), whereas the **DK** method yields higher values of RMSE, RE and MB than does the **PT** method under condition S1 (condition S1 is explained in section 6.3.2). The **PT** method (equation (a)) is more suitable for estimation of evaporation over high-elevation lakes than the **DK** method (equation (b)); the latter was developed from

sea-level environments. When using meteorological observations at the "small lake" to develop the relationships between $Bo = \gamma \frac{(T_s - T_a)}{(E_s - E_a)}$ and $\frac{\gamma}{s}$ (Figure (6.3c)), due to the elevation-dependent variable γ, equation (a) is consistent at the actual air pressure above the lake, whereas equation (b) is more suitable for air pressure at sea level (1013 hPa). Thus, equation (a) in the **PT** method is more applicable over high-elevation lakes, whereas equation (b) in the **DK** method is elevation-dependent.

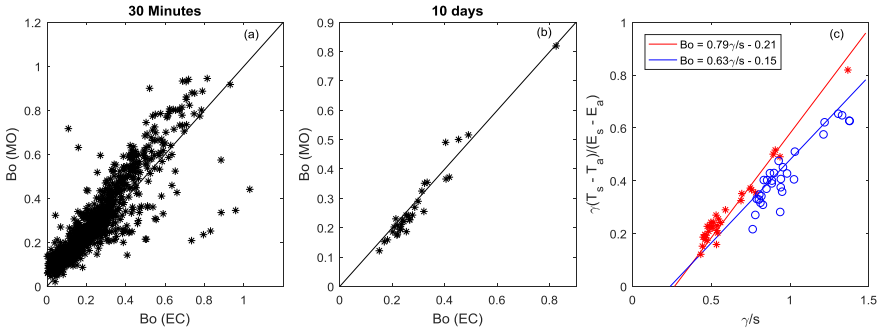

Figure 6.3 Scatter of *Bo* derived from eddy covariance (EC) observations and meteorological observations (MO) at temporal resolutions of (a) 30 minutes and (b) 10 days; (c) relationships between *Bo* and $\frac{\gamma}{s}$ based on actual air pressure (asterisks) and air pressure at sea level (circles).

Due to a lack of long-term observations of temperature gradient in the high-elevation lakes on the TP, heat storage in the water (G_s) needs an alternative expression based on traditional meteorological observations (i.e., net radiation, surface temperature, air temperature). First, G_s could be related to net radiation (R_n): in 22 lakes described by Duan and Bastiaanssen (2015), the hysteresis effect was clearly present in large deep lakes but not small lakes. A high correlation coefficient of 0.82 between G_s and R_n was obtained from our measurements (Figure (6.4a)). Second, increasing/decreasing variations in T_s could describe the accumulation/release of heat storage in the shallow water, and variations in daily surface temperatures over two consecutive days are positively correlated with daily G_s (Wang et al. 2017). Thus, assuming that variations in mixed-layer temperatures (T_s) represent the mean temperature of the entire water column in the "small lake", an adequate correlation coefficient of 0.78 and a linear fitting line (y = 15.91x + 29.22) are obtained between G_s and the variation in water surface temperature ($\Delta T_s = T_s^{i+1} - T_s^i$, with i and i+1 denoting the start and end of a period, for example 10 days) (Figure (6.4b)). Third, considering the strong turbulent mixing between water and air, a correlation coefficient of 0.58 was

found between G_s and ΔT_a (similar to ΔT_s) (Figure (6.4c)), and this high correlation results from their similar seasonal variations. Overall, the RMSE values for G_s with respect to R_n, ΔT_s, and ΔT_a are 15.3 W m^{-2}, 16.7 W m^{-2} and 21.2 W m^{-2}, respectively, which are smaller than the average RMSE values of 22 W m^{-2} from 22 lakes studied by Duan and Bastiaanssen (2015) using remote sensing method. Additionally, a high correlation coefficient (R = 0.72) exists between $R_{s\downarrow}$ and the available energy ($R_n - G_s$), which bridges between the **Mak** method and other energy-budget-based methods.

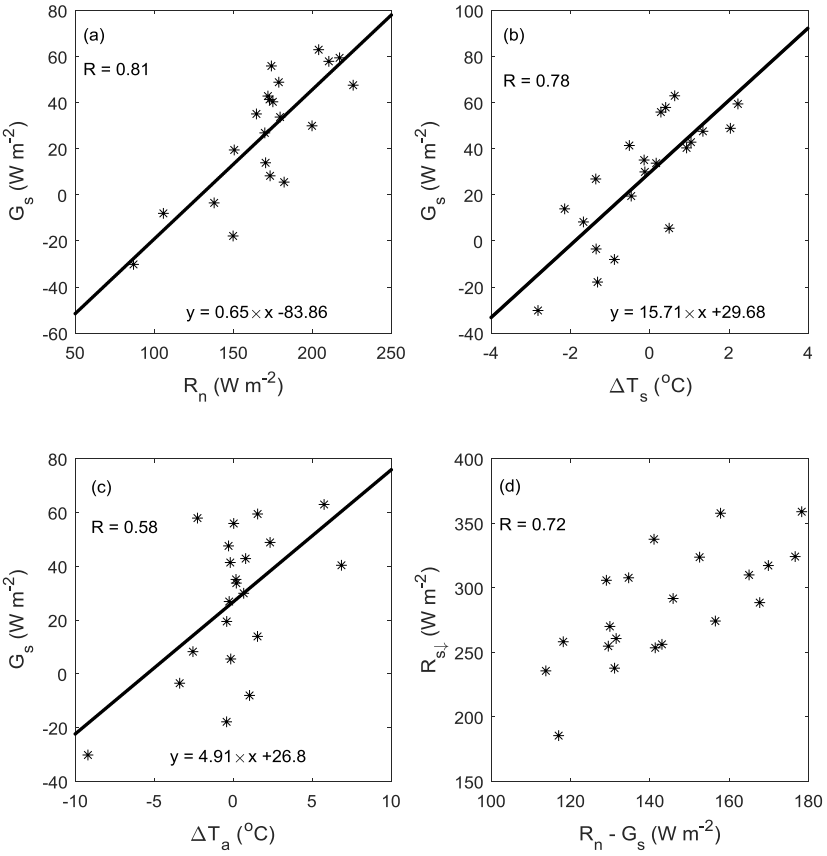

Figure 6.4 Scatterplots of (a) G_s and R_n; (b) G_s and water surface temperature change (ΔT_s); (c) G_s and air temperature change (ΔT_a); (d) $R_{s\downarrow}$ and $R_n - G_s$ at a temporal resolution of 10 days. Correlation coefficients (R) and linear fitting equations are noted.

6.3.2 Rank of evaporation estimation methods

Table 6.2 Root mean square error (RMSE), correlation coefficient (R), relative error (RE) and mean bias (MB) between observed and simulated evaporation in conditions S1 (original parameters), S2 (calibrated parameters), and S3 (the same as condition S2 except that $\boldsymbol{G_s}$ is replaced by $\boldsymbol{R_n}$).

		BREB	PT	PM	BS	DK	Mak	RH	DM	JH	de
RMSE	S1	0.11	0.19	0.26	0.27	0.27	0.37	0.81	1.10	1.57	1.57
	S2	0.11	0.19	0.26	0.27	0.14	0.36	0.22	0.29	0.35	1.02
(mm)	S3	0.42	0.46	0.40	0.59	0.50	0.36	0.22	0.29	0.35	1.02
R	S1	0.99	0.98	0.98	0.94	0.99	0.88	0.96	0.94	0.82	0.84
	S2	0.99	0.98	0.98	0.94	0.99	0.88	0.96	0.94	0.87	0.84
()	S3	0.80	0.78	0.85	0.57	0.78	0.88	0.96	0.94	0.87	0.84
RE	S1	2.6	4.4	5.7	5.7	6.5	7.9	19.7	25.6	39.2	39.4
	S2	2.6	4.4	5.7	5.7	3.1	7.7	4.8	6.9	8.1	18.8
(%)	S3	9.0	9.8	8.2	13.4	11.6	7.7	4.8	6.9	8.1	18.8
MB	S1	0.08	0.14	0.17	0.11	0.25	-0.16	0.77	1.02	-1.46	-1.51
	S2	0.08	0.14	0.17	0.11	0.08	-0.12	0.09	0.08	0.03	0.52
(mm)	S3	0.08	0.13	0.17	0.10	0.25	-0.12	0.09	0.08	0.03	0.52

To rank the performances of the evaporation estimation methods, the evaluations were conducted under 3 conditions (Table (6.2)). In condition S1, the original parameters are used without any optimization and a precisely estimated Q_x (heat storage in the water) is used. In condition S2, the parameters in the **de**, **JH**, **Mak**, **RH**, **DM** methods are optimized based on observations, in addition to a precisely estimated G_s. In condition S3, G_s is substituted based on its relationship with R_n, in addition to parameter optimization. The **BREB** method shows the best performance under condition S1 and S2 due to the observed fact that the Bowen ratios derived from the meteorological observations are consistent with those derived from the eddy covariance data (Figure (6.3)). Among all the methods, the **de** method shows the worst performance, which results from the observed poor correlation between evaporation and the drying power of the air, indicating poor prediction of evaporation without observations of solar radiation and water surface temperature. Moreover, the drying power of the air is only a small modification (21%) to lake evaporation in the **PE** method. Generally, the energy-budget-based group (**BREB**, **PT**, **PE**, **BS** and **DK** methods) under condition S1 performs better compared with the radiation-based group (**Mak** and **JH**) and Dalton type group (**RH** and **DM**). The RMSEs, relative errors (REs) and MBs of the energy-budget-based group are smaller than 0.3 mm, 6% and 0.3 mm, respectively. However, when the parameters in the **de**, **JH**, **Mak**, **RH** and **DM**

methods are optimized based on observations under condition S2, the performances generally improved. The **DK** method with relatively acceptable results from the relationship in Hicks and Hess (1977) improved slightly with a calibrated relationship between the Bowen ratio and $\frac{\gamma}{s}$ due to the dependence of γ on elevation. The **Mak** method shows only a small improvement before and after calibration (with relative errors of 7.9% and 7.7%, respectively). The parameters in the **JH**, **RH** and **DM** methods are site-specific and need calibration before being applied in new environments. Overall, the variation in estimated evaporation after calibration matches the observations quite well, with the largest deviation being that of the **de** method (Figure (6.5)). An approximate ranking of all the methods under condition S2 from best to worst is as follows: energy-budget-based methods > Dalton type methods > radiation-based methods.

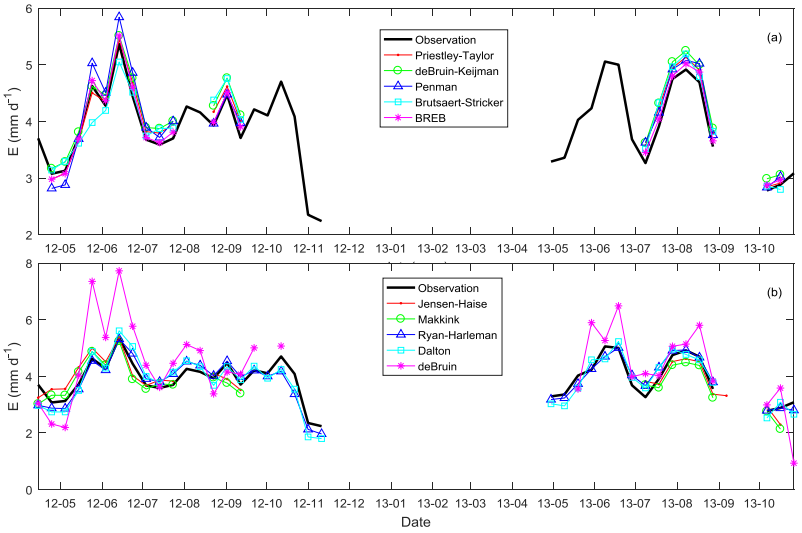

Figure 6.5 Variations in observed and simulated evaporation obtained using the calibrated methods of (a) Priestley-Taylor, deBruin-Keijman, Penman, Brutsaert-Stricker and BREB; (b) Jensen-Haise, Makkink, Ryan-Harleman, Dalton and deBruin in 2012 and 2013.

The energy-budget-based methods and the Dalton type methods after calibration perform better than the radiation-based methods, and the latter show superiority in long-term evaporation analysis due to the difficulty of accessing T_s and G_s. When G_s is determined using empirical formulas (for example, through R_n under conditions S3), the energy-budget-based methods lose their superiority over the calibrated radiation-based methods (Table (6.2)). Moreover, the similar performance of the **Mak** method under all conditions, together with the published good results for a small Canadian lake (Yao 2009) and a small mountain lake in

the U.S. (Rosenberry et al. 2007), suggest good prediction of lake evaporation based on solar radiation and temperature parameters in small and shallow lakes. Thus, the **Mak** method together with ITP forcing data were used to analyze the variation in evaporation of the "small lake" during 1979-2015.

6.3.3 Evaluation of long-term trends of lake evaporation

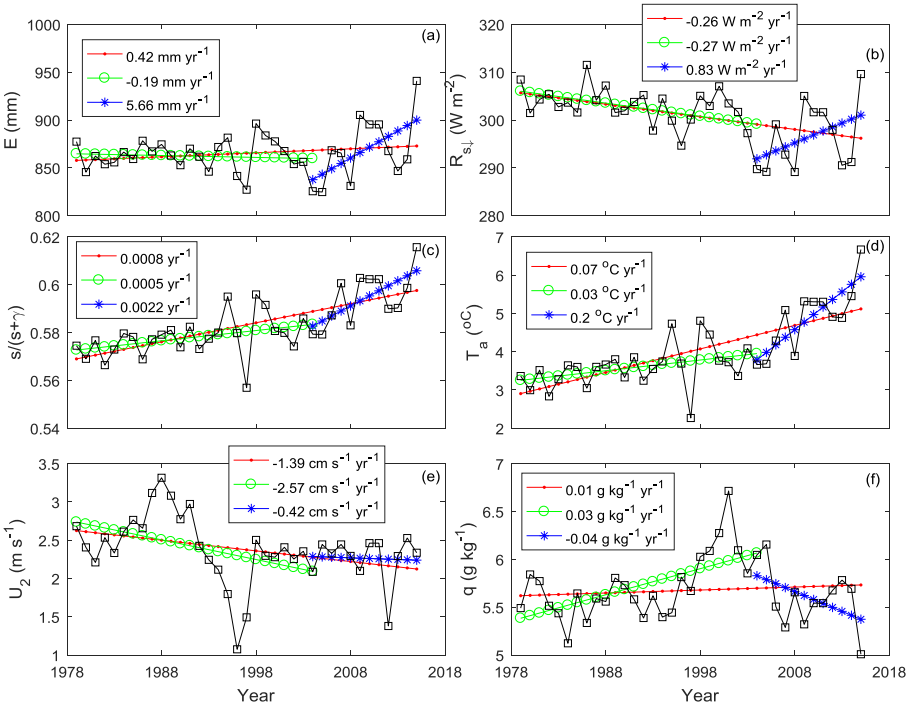

Figure 6.6 Variations in (a) evaporation (E); (b) downward shortwave radiation ($\boldsymbol{R_{s\downarrow}}$); (c) $\boldsymbol{s/(s+\gamma)}$; (d) air temperature ($\boldsymbol{T_a}$); (e) wind speed ($\boldsymbol{U_2}$); and (f) specific humidity (q) at a height of 2 m during the ice-free season from 1979 to 2015. Linear trends of the dotted series, circle series and asterisk series for 1979-2015, 1979-2004 and 2005-2015, respectively, are noted in each panel legend.

The simulated evaporation amounts (867.5 mm in 2012 and 846.7 mm in 2013) over the period of April 11th to November 6th are very close to the observed average evaporation over the 2 years (812 mm), with a slight overestimation of approximately 6%. The smallest evaporation occurred in 2005, and the largest evaporation occurred in 2015 (Figure (6.6a)). The evaporation decreased slightly at a rate of -0.19 mm yr^{-1} during the 1979-2004 period and increased significantly at a rate of 5.66 mm yr^{-1} during the 2004-2015 period; there was an overall increase of 0.42 mm yr^{-1} during the 1979-2015 period. The overall trend coincides with the trend of evaporation from nearby "large lake" based on simulations using

the Flake model (Lazhu et al. 2016). Furthermore, our results support the decreasing-increasing (DI) pattern of reference evapotranspiration since the 1980s over the TP (Xing et al. 2016). Even if there was a rapid decrease from 1998 to 2008, which indicates that lake evaporation may have contributed to the rapid rises in lake water levels during this period (Lei et al. 2013; Ma et al. 2016), lake evaporation has a negative effect on lake expansion in the long run.

Lake evaporation is obtained from the product of a temperature related parameter ($\frac{s}{s+\gamma}$) and solar radiation. And the overall trends of increasing evaporation and decreasing solar radiation contradict the intuitive expectation of a decisive influence of solar radiation on evaporation under conditions of unlimited water. Because a clear decreasing-increasing (DI) trend of evaporation is centered around 2004, the evaporation and climatic variables are separated into two periods: 1979–2004 (period 1) and 2004–2015 (period 2). This DI trend of evaporation is most likely related to the DI trend in solar radiation (Figures (6.6a) and (6.6b)), while the monotonically increase in temperature (or temperature-related parameter) could have accelerated the evaporation (Figures (6.6c) and (6.6d)). In period 1, the decreasing wind speed and increasing specific humidity (Figures (6.6e) and (6.6f)) indicate a smaller advective budget (Hobbins et al. 2004) and could explain the decreasing lake evaporation. The wind speed during period 2 shows a much smaller decrease than that during period 1, and a decrease in specific humidity occurred, which will increase the drying power of the air and increase lake evaporation (Hobbins et al. 2004; Xing et al. 2016).

To quantitatively analyze the contributions of the meteorological variables (air temperature T_a and solar radiation $R_{s\downarrow}$) to the simulated evaporation obtained from the **Mak** method, the "trend removal method" of Xu et al. (2006) was used (Figure (6.7)). The decrease in $R_{s\downarrow}$ and increase in T_a are removed separately, thereby yielding two recovered stationary series for $R_{s\downarrow}$ (Figure (6.7a)) and T_a (Figure (6.7b)). The increasing rate (0.42 mm yr^{-1}) of simulated evaporation based on the original data series can be reduced to much closer to 0 (-0.17 mm yr^{-1}) based on the recovered data series with both trends removed. In addition, the increasing trend can even be enhanced (1.20 mm yr^{-1}) by performing simulations with the recovered $R_{s\downarrow}$ and original T_a and be significantly reduced (-0.93 mm yr^{-1}) by performing simulations with the recovered T_a and original $R_{s\downarrow}$ (Figure (6.7c)). Moreover, both the air temperature and solar radiation show positive correlations with the simulated evaporation. A 5% increase/decrease in $R_{s\downarrow}$ and an 2℃ increase/decrease in T_a will lead to a combined increase/decrease of approximately 10% of the simulated evaporation. Specifically, a $\pm 5\%$ variation

in solar radiation has an effect on evaporation similar to that of a variation of ± 2℃ in air temperature, and both will separately influence the simulated evaporation by $\pm 5\%$.

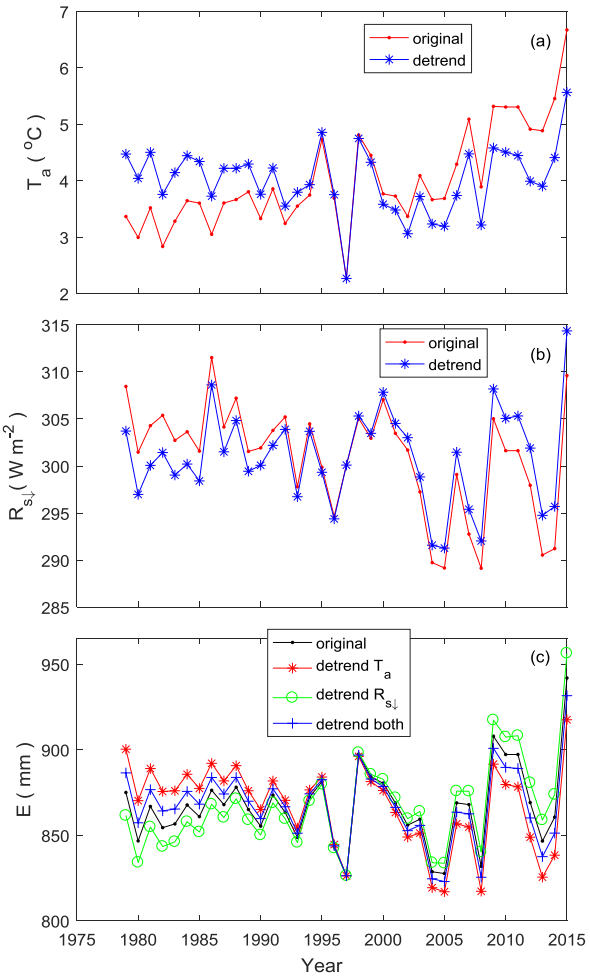

Figure 6.7 Plots of the original series ("original") and the recovered series ("detrend") of (a) air temperature (T_a) and (b) downward shortwave radiation ($R_{s\downarrow}$); (c) comparison of original total evaporation and recalculated total evaporations from April 11th to November 6th. The "original" line is the evaporation estimated using original values of T_a and $R_{s\downarrow}$; the "detrend both" line is the evaporation estimated from detrend values of T_a and $R_{s\downarrow}$; the "detrend T_a" is the evaporation estimated from original values of $R_{s\downarrow}$ and detrend values of T_a; the "detrend $R_{s\downarrow}$" is the evaporation estimated from original values of T_a and detrend values of $R_{s\downarrow}$.

6.4 Evaluation of Flake modeling

6.4.1 Sensitivity analysis of lake depth and extinction coefficient

Lake depth and extinction coefficient are two specific key parameters in Flake modeling (Mironov 2008). Firstly, sensitivity experiments of lake depths (ranging from 1 m to 15 m, increased by 2 m) are conducted by in-situ observations of "small lake" during 2012 to 2013, and the simulation results are evaluated by observations of lake surface temperature (T_s). All simulations with different depths could generally reproduce the seasonal variation of T_s with significant differences existing during periods of shortly after ice-melt and before ice-forming, during when the simulated mixed-layer depth (D_{ml}) show largest discrepancy (Figure (6.8)). Further, it is reasonable that the simulated T_s increases much faster after ice-melt and decreases much earlier before ice-frozen in shallower lake depth. For instance, the simulated date of ice-forming (at a temperature of 0 ℃) was 8th November at 1 m depth simulation and 7th December at 15 m depth simulation. Even though all simulations show a delayed ice-melt date, the simulated ice-frozen date suggest that estimated mean depth of 7 m is reasonable for Flake modeling in the "small lake".

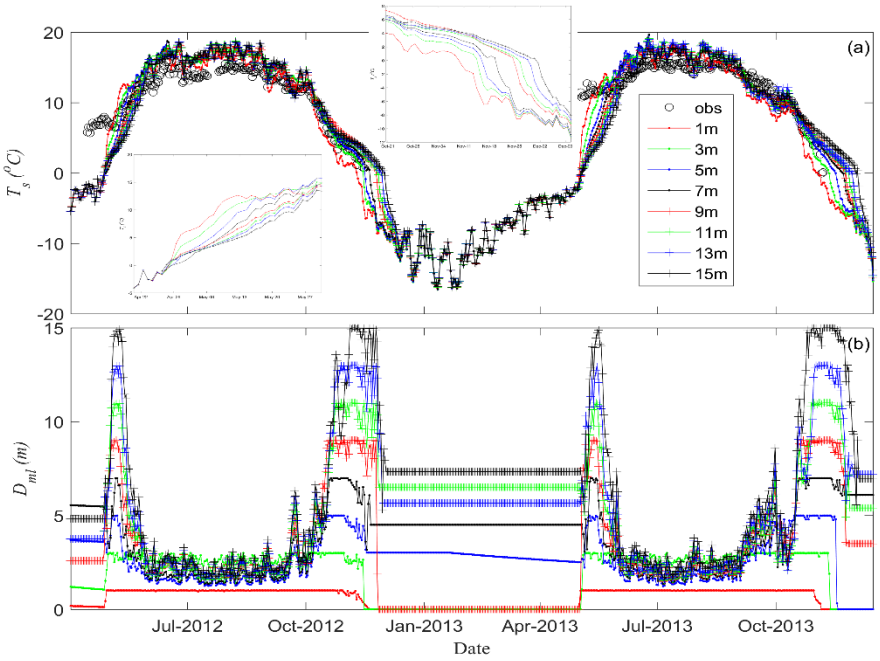

Figure 6.8 (a) The variation of simulated and observed daily T_s; (b) the variation of simulated mixed layer depths with simulation depths of 1 m, 3 m, 5 m, 7 m, 9 m, 11 m, 13 m, 15 m.

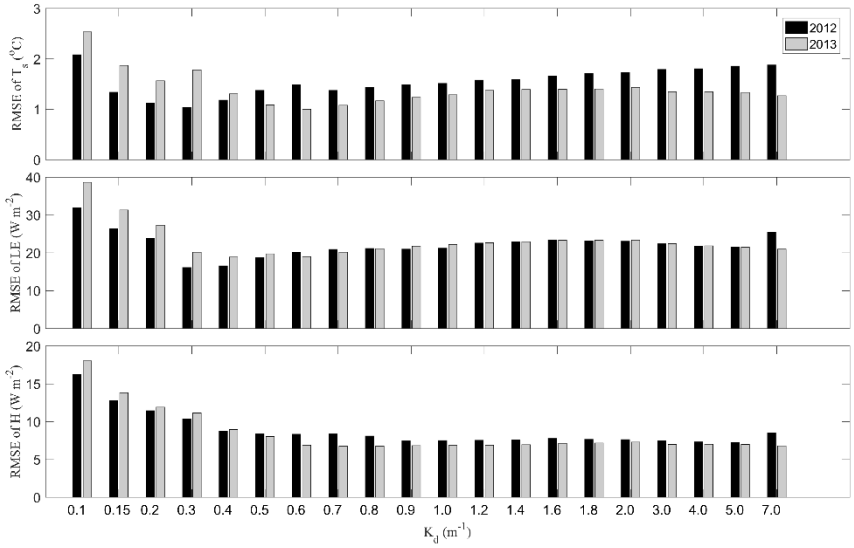

Figure 6.9 RMSE values of $\boldsymbol{T_s}$ (a); *LE* (b) and *H* (c) between observation and simulation for 2012 and 2013.

After that, sensitivity experiments of K_d (ranging from 0.1 m^{-1} to 7.0 m^{-1}, totally 20 experiments) are conducted, and the simulation results are evaluated by in-situ observations of T_s and turbulent heat flux with Root-Mean-Square-Error (RMSE) values shown in Figure (6.9). K_d value could directly determine the distribution of solar radiation in the water column, influence the simulated D_{ml} and then alter the amplitude of diurnal variations of T_s. The RMSE values of T_s show a decreasing trend to a K_d value of 0.4 m^{-1}, and then keep a slightly increasing trend afterwards (Figure (6.9a)) while those for simulated *LE* (Figure 6.9b) and *H* (Figure 6.9c) are quite similar, with decreasing trends to a K_d value of around 0.4 m^{-1} and relatively stable values afterwards. The smallest RMSE values of T_s, *LE* and *H* for 2012 are approximately 1 ℃, 20 W m^{-2} and 8 W m^{-2} respectively. The influence of K_d on the diurnal variation of simulated T_s in the "small lake" and "large lake" will be further discussed in detail in section 6.4.2.

6.4.2 Model performances evaluation

Daily T_s has been used as validation data as in (Kirillin et al. 2017; Lazhu et al. 2016; Thiery et al. 2014b; Zolfaghari et al. 2017); and the simulated daily T_s with smallest RMSE values are always supposed to be "appropriate parameter settings" in model simulation (Dutra et al. 2010). However, diurnal variation of T_s always show much more details for model evaluation, as in Stepanenko et al. (2014a). In this section, model performances in the two water bodies are evaluated by both

in-situ observations of daily and diurnal T_s and turbulent heat flux, in addition with the observed mixed layer depth in the "large lake".

6.4.2.1 Model performance in the "small lake"

Using observed *H*, *LE*, daily T_s and diurnal T_s in the "small lake", model simulations are evaluated for K_d values of 0.4 m^{-1} (the smallest RMSE value of daily T_s), 0.6 m^{-1} (the estimated value by Secchi depth) and 2.0 m^{-1} (close to the amplitude of diurnal variation of T_s), respectively in Figure (6.10). The seasonal variations of daily T_s, *H* and *LE* could all be reproduced by Flake simulations, with clear underestimations existed in April-May. The underestimation of simulated T_s in April-May (Figure 6.10c1-c2-c3) will result in smaller gradients of temperature and water vapor between lake and atmosphere, thus could explain the underestimation of corresponding *LE* (Figure (6.10b1-b2-b3)) and *H* (Figure (6.10a1-a2-a3)). As a higher K_d value can trap solar radiation in a shallower water depth, form a shallower mixed-layer and lead to a larger amplitude of diurnal variation of T_s, the amplitude of diurnal variation of T_s at a K_d value of 2 m^{-1} is more close to observations compared to those of the other two (Figure 6.10d1-d2-d3). Thus, two shortcomings of Flake simulation exists: (1), the simulated date of ice-melt appears one month late relative to observations and clear underestimations of simulated T_s exist during this period (Figure 6.8a and Figure 6.10d1-d2-d3). (2), Even though Flake simulation could generally reproduce the seasonal variation of daily T_s in the "small lake", the amplitude of diurnal variation of T_s could not be attained. Moreover, the simulated D_{ml} is around 2.5 m during June to September in 2012 (similar for 2013, Figure 6.8a), during when the simulated T_s are a little higher than the observations (Figure 6.10c-6.10d). The overestimation of simulated T_s is speculated to be related to the underestimated D_{ml}, and more discussions could be found in section 6.5.1.

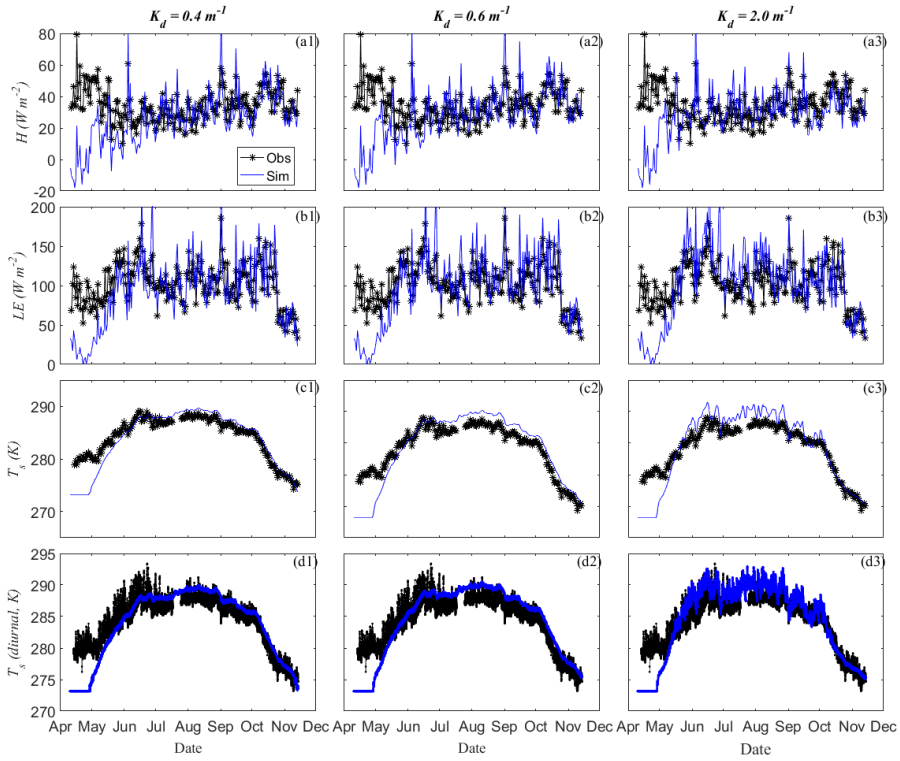

Figure 6.10 The seasonal variation of daily *H*, *LE*, daily $\boldsymbol{T_s}$ and diurnal $\boldsymbol{T_s}$ between observation and simulation at extinction coefficients of 0.4 m^{-1}(a1, b1, c1, d1), 0.6 m^{-1}(a2, b2, c2, d2) and 2.0 m^{-1}(a3, b3, c3, d3), respectively.

6.4.2.2 Model performance in the "large lake"

Similarly, we conducted sensitivity experiments of K_d values for observations in the "large lake". The seasonal variations of daily *H*, daily *LE*, D_{ml} and T_s at K_d values of 0.1 m^{-1} (observed through PAR probe following Huang et al. (2017)), 0.3 m^{-1} (observed through experiment of Secchi depth in Novemer, 2016), and 1.6 m^{-1} (close to the amplitude of diurnal variation of simulated T_s) are evaluated by observation in Figure (6.11). The increasing trends of *H*, *LE* and D_{ml}, together with the seasonal variation of T_s show much good performances at a K_d value of 0.1 m^{-1} rather than the simulations at K_d values of 0.3 m^{-1} and 1.6 m^{-1}. A higher K_d value corresponds to a shallower mixed-layer depth, and then a larger amplitude of diurnal variation of T_s (Figure (6.11c-d)). Thus, the obvious overestimation of simulated *H* and *LE* at K_d values of 0.3 m^{-1} and 1.6 m^{-1} are corresponding to the lower estimated D_{ml} and higher estimated T_s (Figure (6.11a2-d2) and Figure (6.11a3-d3)). Further, the lower estimated amplitude of

D_{ml} could result in underestimated amplitude of diurnal variation of T_s, and the amplitude of diurnal variation of T_s are much close to the observations at a K_d value of 1.6 m^{-1}. We conclude that K_d values could determine the distribution of solar radiation in the water column, influence the simulated D_{ml}, impact on the amplitude of diurnal variation of T_s and finally show effects on the simulated H and LE.

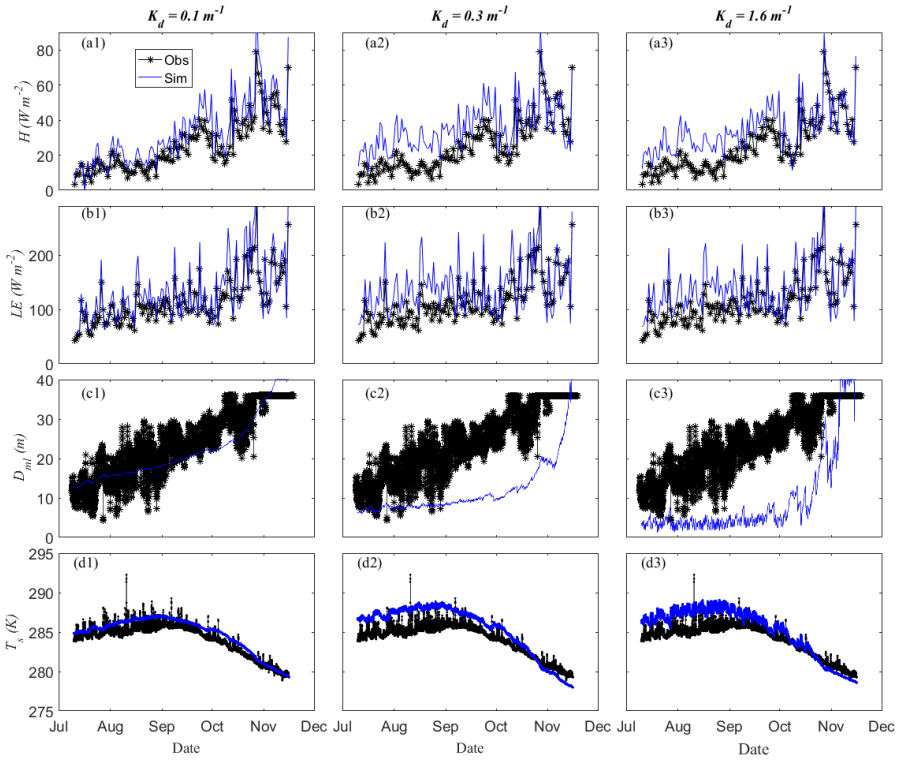

Figure 6.11 The seasonal variation of daily H, LE, mixed-layer depth and diurnal $\boldsymbol{T_s}$ between observation and simulation at extinction coefficients of 0.1 m^{-1}(a1, b1, c1, d1), 0.3 m^{-1}(a2, b2, c2, d2) and 1.6 m^{-1}(a3, b3, c3, d3), respectively.

As Flake simulations at a K_d value of 0.1 m^{-1} could describe heat transfer process much better, the results are used to evaluate the model performances quantitatively. The simulated H and LE show increasing trends from July to November as do the observations, with RMSE values of approximately 9 W m^{-2} and 18 W m^{-2} respectively. As an energy budget closure value of about 0.86 during July to November is obtained by radiation and EC observations, the simulated T_s shows clear overestimation (Figure (6.11d1)). Assuming a closed energy budget in the "large lake" and removing the residual 14% from $R_{s\downarrow}$, the

simulated T_s is much more close to the observations, with RMSE values reducing from 3.15 ℃ to 1.9 ℃. Generally, the Flake model could simulate the seasonal variation of T_s, describe the increasing trend of *H* and *LE*, and catch the seasonal variation of D_{ml}, thus the simulations at a K_d value of 0.1 m^{-1} are further used for long term trend analysis in Section 6.4.4.

6.4.3 Model's performance to forcing variables

To test the model's performance to forcing variables both in the "small lake" and in the "large lake", we combined observation data of ITP-forcing, PBL tower measurements and in-situ data together and formed three long-term forcing data series: "ITP forcing", "tower forcing", "in-situ forcing". (1), The "ITP forcing" comes from the ITP forcing data, which are calibrated by PBL tower observation in Nam Co station; (2) the "tower forcing" uses "ITP forcing" as base and substitute "ITP forcing" with PBL tower observation during observation period of Nam Co station; (3) the "in-situ forcing" use "tower forcing" as base and substitute "tower forcing" with in-situ observations in the "small lake" and in the "large lake" respectively. Thus, the "ITP forcing" and "tower forcing" are considered as observation in land-dominated environment while "in-situ forcing" are considered as observation in lake-dominated environment. The simulation results are inter-compared for the "small lake" in section 6.4.3.1 and for the "large lake" in section 6.4.3.2, respectively.

6.4.3.1 Model's performance to forcing variables in the "small lake"

The performances of simulated *LE* by using "ITP forcing", "tower forcing" and "in-situ forcing" are evaluated with EC observations in Figure (6.12). The scatter-plots of half-hourly *LE* show quite reasonable results by "in-situ forcing" and "tower forcing", with quite close RMSE values of 46.5 W m^{-2} and 44.0 W m^{-2}, respectively (Figure 6.12b-c). However, the simulated results by using "ITP forcing" show a much larger scatter and have a nearly double RMSE value of 82.5 W m^{-2}. It indicates that "ITP forcing" is not appropriate for describing the diurnal variation of *LE*, even though the "ITP forcing" are calibrated by in-situ observations. The largest uncertainty in "ITP forcing" results from the bias in wind speed. For example, when wind speed from "ITP forcing" are substituted by that from "tower forcing", the scatter plot between simulation and observation are much close to the 1:1 line, with a RMSE value of 46.0 W m^{-2}. The monthly values of simulated *LE* show similar seasonal variations for all three forcing, with a peak value in June. The largest bias exist in April and May, during when the simulated T_s are much lower than the observations. In a brief conclusion, the

Flake model shows reasonable seasonal variation of simulated *LE* in the "small lake", with largest errors existing over periods of shortly after ice-melt; and the Flake model driven by reanalysis data are found to be inappropriate for diurnal variation of *LE*, which result from the widely recognized uncertainties in wind speed.

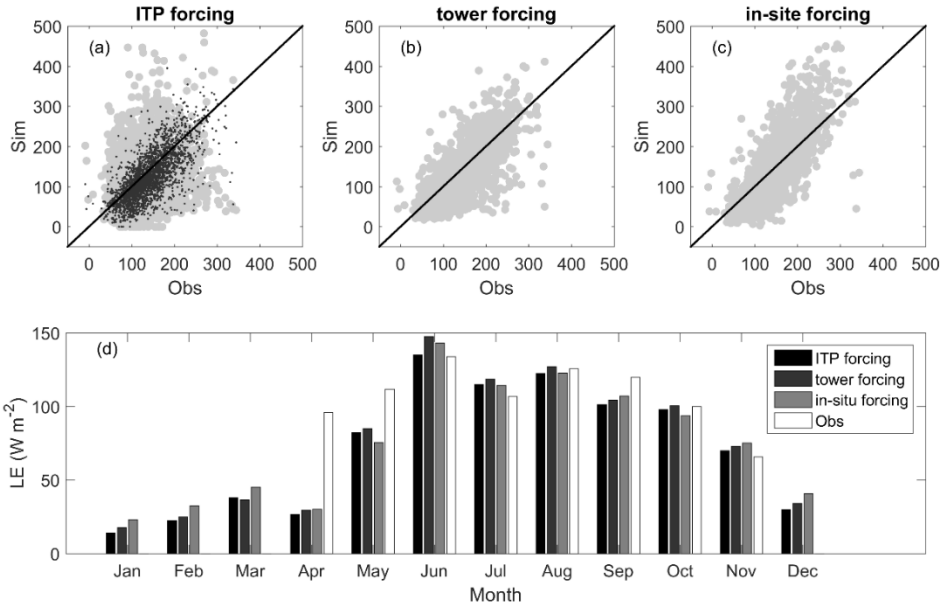

Figure 6.12 The comparison between observation and simulation by (a) ITP forcing; (b) tower forcing; (c) in-situ forcing; (d) the seasonal variations of simulated *LE* and observations.

6.4.3.2 Model's performance to forcing variables in the "large lake"

Similarly, to explore model sensitivity to forcing variables in the "large lake", the seasonal variations of forcing variables and Flake simulations by using "ITP forcing", "tower forcing" and "in-situ forcing" (observations on the island) are inter-compared and also evaluated by in-situ observations of turbulent heat flux and T_s (Figure (6.13)). The input forcing in lake-dominated environment and land-dominated environment are quite different: (1) the wind speed by lake-dominated environment has a much larger value than those from land-dominated observations (Figure 6.13c). The air temperature (T_a) and downward longwave radiation ($R_{l\downarrow}$) in the former are higher than those in the latter, especially during August to December (Figure 6.13e and Figure 6.13h) because of the warm lake effect; the downward shortwave radiation ($R_{s\downarrow}$, Figure 6.13g) during the monsoon season (July-September) is much higher in the lake-dominated environment than

those in the land-dominated environment, which may result from the different pattern of cloud formation around the lake and over the lake.

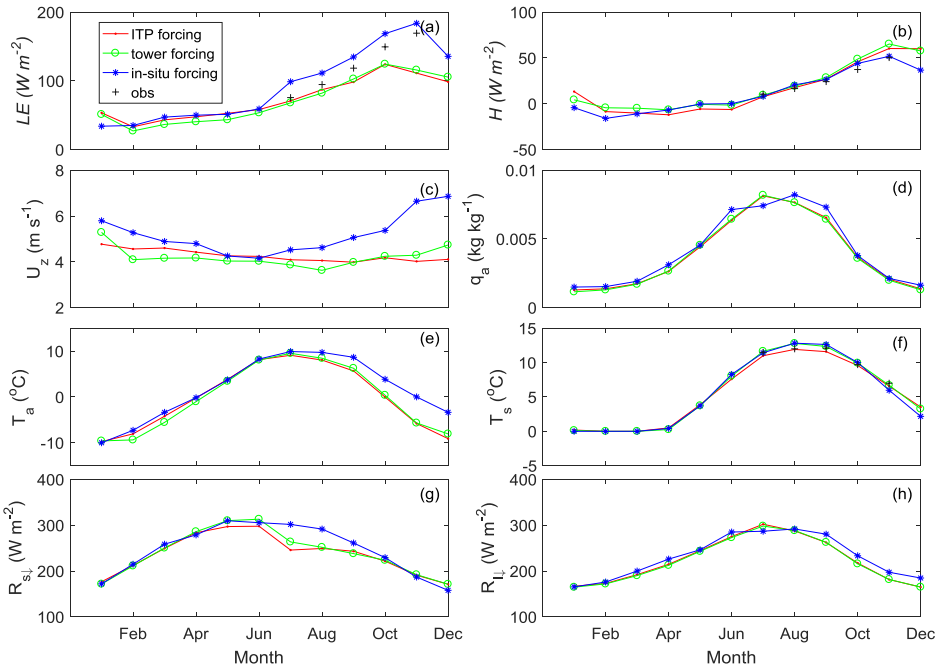

Figure 6.13 The variation of monthly averaged (a) simulated *LE*; (b) simulated *H*; (c) $\boldsymbol{U_z}$; (d)$\boldsymbol{q_a}$; (e) $\boldsymbol{T_a}$; (f) $\boldsymbol{T_s}$; (g) $\boldsymbol{R_{s\downarrow}}$; (h) $\boldsymbol{R_{l\downarrow}}$. Where "plus" indicates observation ('obs'); "dot line" indicates ITP forcing; "circle line" indicates tower forcing; "star line" indicates in-situ forcing.

The simulated difference in *LE* and *H* mainly happens during open water period of July to December, during when the simulated *LE* by using land-dominated forcing show similar seasonal variation and both are much smaller than the simulations by lake-dominated forcing (Figure (6.13a)). Further, the simulated *H* are quite similar by using land-dominated forcing, but they are close to the simulations by using lake-dominated forcing except in November and December. Wang et al. (2017) have shown that the seasonal variations of *LE* and *H* are dominated by wind speed multiply water vapor gradient and wind speed multiply temperature gradient respectively on temporal scale of monthly. As observed specific humidity and simulated monthly water surface temperature are quite similar for all three forcing (Figure (6.13d)), the higher *LE* in lake-dominated environment mainly result from its much higher wind speed (Figure (6.13c)). And the simulated *H* are influenced by a combined effect of much higher wind speed and much lower temperature gradient in lake-dominated observations (Figure

(6.13e-f)). In addition, the peak value of largest *LE* in November could be simulated by lake-dominated forcing while the peak value is in October by simulations using land-dominated forcing, as in Lazhu et al. (2016). The much higher simulated *LE* then in-situ observations during July to November should result from the facts of energy imbalance in observations (with energy balance value of 0.859 during July to November) and the energy balance assumption in Flake modeling.

6.4.4 Lake's response to climate change and their driving forces

Lake warming has been reported on numerous lakes world widely [*Coats et al.*, 2006; *Hampton et al.*, 2008; *O'Reilly et al.*, 2015], and recently for lake Nam Co on the TP [*Huang et al.*, 2017]. However, no significant trends of lake temperature and stratification are found by Flake simulations over two freshwater lakes of Ngoring and Gyaring [*Kirillin et al.*, 2017]. After the aforementioned rigorous evaluations in Nam Co with good performances in simulated seasonal variations of T_s, D_{ml} and turbulent heat flux, we conclude that the processes of lake-atmosphere interaction and internal mixing regimes could generally be reproduced. Thus, Flake simulations, including their meteorological forcing, are analyzed together to summarize lakes' response to climate change and their driving forces behind.

6.4.4.1 Lake's response to climate change

Firstly, under the climatic background of significant air warming and moistening, wind stilling and solar dimming on the TP [K Yang et al., 2014], increasing trends of air temperature, specific humidity and decreasing trends of wind speed, solar radiation are clearly present in the corrected ITP forcing data (Figure 6.14a-c), with values of 0.81 ℃ decade^{-1}, 0.0001 kg kg^{-1} decade^{-1}, -0.1 m s^{-1} decade^{-1} and -2.4 W m^{-2} decade^{-1}. The most significant trend is downward longwave radiation, which has a value of 12.3 W m^{-2} decade^{-1}. The simulated lake surface temperature shows a clear warming, with a warming rate of 0.44 ℃ decade^{-1} while the simulated bottom temperature (40 m) shows a slightly weak and insignificant increasing trend, with a value of 0.01 ℃ decade^{-1}. Thus, a fast warming surface and a slow warming bottom indicates a more stable water column, accompanied by the simulated decreasing trend of mean D_{ml} of -0.23 m decade^{-1}. In addition, the date of spring overturn happens much earlier while the date of autumn overturn postpones a little bit, which result in a much longer stratification days in Nam Co. Further, both the simulated latent heat flux and

sensible heat flux are showing increasing trends, with values of 6.1 W m^{-2} decade^{-1}and 4.4 W m^{-2} decade^{-1} respectively.

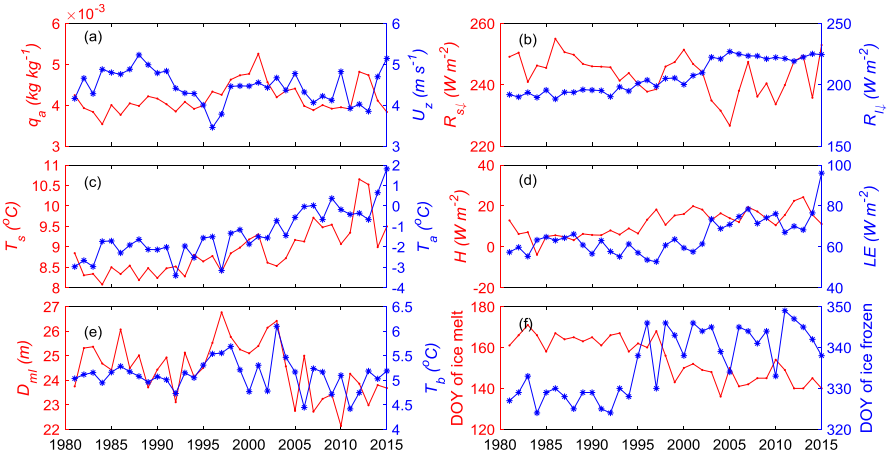

Figure 6.14 The inter-annual variations of (a) specific humidity (q_a) & wind speed (U_z); (b) downward shortwave radiation ($R_{s\downarrow}$) and downward longwave radiation ($R_{l\downarrow}$); (c) simulated surface temperature (T_s) and air temperature (T_a); (d) simulated H and LE; (e) simulated mixed layer depth (D_{ml}) and bottom temperature (T_b); (f) simulated DOY of ice melt and DOY of ice frozen.

6.4.4.2 Driving forces behind lake's variations

Lake warming is considered as the response of inland water bodies to global warming and it has been found all over the world. Increasing trends of T_s and turbulent heat flux in Nam Co have also been recognized by Flake simulations in our research, similar to those found in previous publications [Huang et al., 2017; Lazhu et al., 2016]. T_a and $R_{l\downarrow}$ are attributed to the lake warming [Huang et al., 2017] while meteorological variables of T_a, $R_{s\downarrow}$ and $R_{l\downarrow}$ play the dominate role in simulation of evaporation [Lazhu et al., 2016]. In order to investigate the relative significance in trends of each forcing variable on the trends of simulated T_s and turbulent heat flux, the trend removal analysis [Xu et al., 2006] is performed according to the following steps: (i) trends in the meteorological variables (including $R_{s\downarrow}$, $R_{l\downarrow}$, T_a, q_a, U_z) are removed, forming 5 stationary time series. (ii) 7 experiments of Flake simulations are performed with different combination of forcing data used, including the trend-removed for single variable of (EXP1) $R_{s\downarrow}$, (EXP2) $R_{l\downarrow}$, (EXP3) T_a, (EXP4) q_a, (EXP5) U_z and original forcing for other variables; (EXP6) original forcing (OD); and (EXP7) the trend-removed data for all variables (TRA). (iii) Trends of simulated T_s and turbulent heat flux are

established by simple linear regression method and inter-compared amongst each other.

The simulation results after trend removal are shown in Table 6.3 and Figure 6.15. First, for the trends of simulated T_s, trends removal of $R_{s\downarrow}$ (0.49 ℃ decade^{-1}), q_a (0.41 ℃ decade^{-1}), and U_z (0.46 ℃ decade^{-1}) show relatively minor influences on the lake warming, compared with the trend of 0.44 ℃ decade^{-1} by original data. Trend removal of T_a could reduce the lake warming a little bit, but a clear increasing trend (0.32 ℃ decade^{-1}) could still be found. The trend approaches to zero for simulations with trend removal for all variables (0.02 ℃ decade^{-1}) or simply by single variable of $R_{l\downarrow}$ (0.13 ℃ decade^{-1}). Thus, $R_{l\downarrow}$, rather than T_a, play the dominant role in lake warming. Second, the simulated LE show an obvious increasing trend (6.1 W m^{-2} decade^{-1}) for original data series while the large trends would disappear for EXP7 (TRA forcing) and EXP6 (trend removal for $R_{l\downarrow}$), with negative trends of -1.9 W m^{-2} decade^{-1} and -0.8 W m^{-2} decade^{-1}, respectively. Trends removal of $R_{s\downarrow}$ and q_a could increase the trend of LE while trend removal of U_z have very small influences compared with that by original forcing. Further, trend removal of T_a could reduce the increasing trend of simulated *LE*. Thus, the increasing trend in $R_{l\downarrow}$ could attribute to the increasing trend of *LE* while the increasing trend of T_a could also contribute to a much smaller magnitude. Third, the increasing trend of H by original forcing has a value of 4.4 W m^{-2} decade^{-1}. The detrend single parameter of U_z and q_a have minor influence on the trend of simulated *H*. The trend removal by $R_{s\downarrow}$ and T_a could enlarge the trend of H through temperature gradient while trend removal of $R_{l\downarrow}$ could reduce that through decreasing the simulated T_s. An increasing trend of simulated *H* still exist with a value of 1.9 W m^{-2} decade^{-1} for TRA. Thus, the simulated *H* could be influenced by a combination effect of $R_{s\downarrow}$, $R_{l\downarrow}$ and T_a through their impacts on lake-atmosphere temperature gradients.

Table 6.3 The trends of simulated $\boldsymbol{T_s}$, *LE* and *H* for all different experiments. TRA: trend remove for all variables; $\boldsymbol{R_{s\downarrow}}$, $\boldsymbol{R_{l\downarrow}}$, $\boldsymbol{T_a}$, $\boldsymbol{q_a}$, $\boldsymbol{U_z}$: trend removal for each single variable; OD: ordinary data.

	TRA	$R_{s\downarrow}$	$R_{l\downarrow}$	T_a	q_a	U_z	OD
T_s (℃ decade^{-1})	-0.0006	0.091	0.026	0.053	0.075	0.078	0.080
LE (W m^{-2} decade^{-1})	-1.41	9.58	-0.24	5.04	8.91	8.51	8.27
SH (W m^{-2} decade^{-1})	2.04	5.79	-0.97	7.96	4.45	4.68	4.89

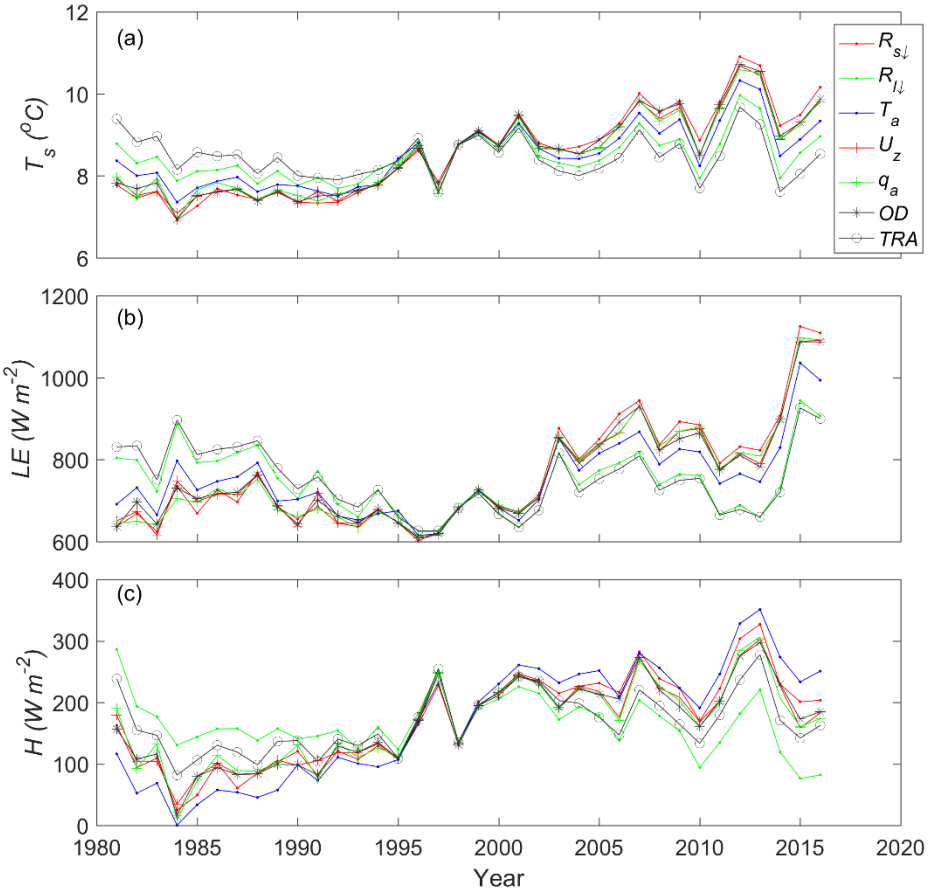

Figure 6.15 The plots of simulated annual evaporation (dot line) by using (a) downward shortwave radiation with trend removed, (b) downward longwave radiation with trend removed, (c) air temperature with trend removed, and (d) wind speed with trend removed and original data for all other variables. the simulated annual evaporations by using original meteorological variables (star line) and by using meteorological variables with all trends removed (circle line) are plotted as reference in each subplot.

6.5 Discussions

6.5.1 Uncertainties in traditional evaporation methods

The actual evaporation and potential evaporation, which have a complementary relationship, become identical when evaporation is not limited by ready access to water but rather by the available energy (Szilagyi 2008). Further, an oasis effect of possible sensible heat advection and mixing of dry air from its surroundings may affect small lakes. However, the evaporation amounts we obtained using the

PE, **BT** and **BS** methods all nearly match, which indicates a radiation-limited and humid environment caused by the presence of Nam Co lake. When these three methods are applied to a lake in a more arid environment, their differences should be much larger. The poor performance of the **de** method may result from strong lake-land breeze, which will alter the drying power of the air. The water surface temperature and site-specific bulk transfer coefficients are key parameters in Dalton type methods, whereas the thermal temperature distribution in the water plays a significant role in the energy-budget-based methods. The relatively good performance of the **Mak** method under condition S3 indicates that solar radiation and air temperature can provide good estimates of evaporation from small lakes.

Only the trends in wind speed and specific humidity were used in our analysis of evaporation change. The strange behaviors of wind speed in 1990s and specific humidity in the 2000s shown in Figure (6.6) probably originate in the relevant data sources and do not influence our conclusions. Because small lakes have a fast thermal response to solar heating, the DI trend of $\boldsymbol{R_{s\downarrow}}$ corresponds well to that of evaporation in the "small lake". However, the overall trend of evaporation during the 1979-2015 period contrasts with that of $\boldsymbol{R_{s\downarrow}}$, which may be attributed to the temperature-related parameter. When air warms, its ability to hold water vapor increases, and evaporation thereby increases. The short duration of the ice-cover period due to increased air temperature may increase the amount of absorbed solar radiation stored in the water, thus enhancing the increasing trend of annual evaporation and causing additional positive climate feedback. However, the increased downward longwave radiation indicates an increase in cloud covers, thereby causing a decrease in shortwave radiation, which will cause negative feedback. Pan evaporation and reference evapotranspiration over the TP decreased significantly during the few decades prior to 2000 (Hobbins et al. 2004; Xing et al. 2016). In contrast, an increasing rate of lake evaporation in the recent ten years is indicated by our findings.

6.5.2 Uncertainties in mixed-layer depth related issues

The amplitudes of diurnal variation of simulated $\mathbf{T_s}$ with $\boldsymbol{K_d}$ value close to in-situ observations are smaller than that of the observed $\mathbf{T_s}$ during summer open-water periods of the "small lake" (Figure 6.10d1 and 6.10d2) and the "large lake" (Figure 6.11d1 and 6.11d2) respectively in Flake modeling. The reason should result from the inadequate parameterization scheme for diurnal variation of $\boldsymbol{D_{ml}}$ estimation (see Supplement Materials). The related important parameters for $\boldsymbol{D_{ml}}$ estimation includes: (1) the dimensionless constants $\boldsymbol{C_n}$, $\boldsymbol{C_i}$ and $\boldsymbol{C_s}$ in equation 8s,

which are derived from Zilitinkevich and Mironov [1996], with $\boldsymbol{C_n}$ ranging from 0.1-0.5, $\boldsymbol{C_s}$ from 1.2-100, $\boldsymbol{C_i}$ at order of 10; (2) the dimensionless constant $\boldsymbol{C_{rh}}$ in equation 7s for $\boldsymbol{D_{ml}}$ estimation of a stably or neutrally stratified wind-mixed layer, with values ranging from 0.025 to 0.5 in different publications [Mironov, 2008]; (3), the constants of $\boldsymbol{C_{c1}}$ and $\boldsymbol{C_{c2}}$ in equation 1s. Sensitivity analysis of these aforementioned values show that: (1), variations of $\boldsymbol{C_n}$, $\boldsymbol{C_i}$ and $\boldsymbol{C_s}$ are not sensitive to estimation of $\boldsymbol{D_{ml}}$. (2) A smaller $\boldsymbol{C_{rh}}$ will have a much larger $\boldsymbol{D_{ml}}$, but with smaller amplitude of $\boldsymbol{D_{ml}}$ variation, and vice versa. (3) $\boldsymbol{C_{c1}}$ shows high sensitivity to the simulated $\boldsymbol{D_{ml}}$ estimation, but not for $\boldsymbol{C_{c2}}$. A larger $\boldsymbol{C_{c1}}$ will have a much larger $\boldsymbol{D_{ml}}$ and a much higher amplitude of $\boldsymbol{D_{ml}}$ variation. Thus, the most sensitive constants to $\boldsymbol{D_{ml}}$ estimation are $\boldsymbol{C_{c1}}$ and $\boldsymbol{C_{rh}}$ in heat flux driven mixing and wind driven mixing respectively. However, optimization of these constants could not improve the $\boldsymbol{D_{ml}}$ simulation both in the "small lake" and in the "large lake".

Moreover, a larger amplitude of $\boldsymbol{T_s}$ in the "small lake" than that in the "large lake" is observed (Figure 6.10d and Figure 6.11d). The reason results from the facts that: compared with the "large lake", surface warming during the day should be more significant in the "small lake", due to its weaker wind induced mixing, larger $\boldsymbol{K_d}$ and thus shallower $\boldsymbol{D_{ml}}$; while surface cooling at night in the "small lake" should also be much strong because of its smaller thermal capacity and larger water-air temperature gradient. Even though the seasonal variation of simulated $\boldsymbol{D_{ml}}$ could be captured in the "large lake", the amplitude of diurnal variation of $\boldsymbol{D_{ml}}$ is significantly underestimated relative to observations (Figure 6.11c1). Thus, the estimated $\boldsymbol{D_{ml}}$ of around 2 m during June to September (Figure 6.8b) in the "small lake" is most probably underestimated. The underestimation of the amplitude of diurnal $\boldsymbol{D_{ml}}$ will lead to underestimation of the amplitude of diurnal $\boldsymbol{T_s}$ (Figure 6.10d and Figure 6.11d). Even though a larger extinction coefficient could increase the amplitude of simulated $\boldsymbol{T_s}$ in the "small lake" (Figure 6.10d), the $\boldsymbol{D_{ml}}$ and $\boldsymbol{T_s}$ may indicate inadequate pattern of their seasonal variations as in the "large lake" (Figure 6.11c and 6.11d). Thus, a much robust $\boldsymbol{D_{ml}}$ estimation parameterization scheme is needed for Flake model development to account for the inappropriate diurnal variation of $\boldsymbol{D_{ml}}$ and $\boldsymbol{T_s}$.

6.5.3 Discussions on lake's response to climate change

The climate over the Tibetan Plateau shows decreasing trends in $R_{s\downarrow}$ and U_z, and increasing trends in $R_{l\downarrow}$, T_a and q_a, similar as in [*Yang et al.*, 2014]. The simulated lake warming during its stratification periods with a value of 0.44 ℃

decade^{-1} is a little smaller than the simulated lake warming rate of 0.52 ± 0.25 ℃ decade^{-1} during July to September by General lake model [*Huang et al.*, 2017], where increased T_a and $R_{l\downarrow}$ are considered as the driving forces for lake warming. Through trend removal analysis in section 3.4.2, our results support the above conclusion. Trend removal of T_a could decrease the increasing trend of T_s through combined effect of water-air interactions, with significantly increase in *H* and slightly decrease in *LE*. Thus, we further emphasize the significance of $R_{l\downarrow}$, which is the direct energy forcing for lake warming and shows higher significance than T_a.

Wind speed and vapor/temperature gradients between water and atmosphere are the main driving forces for latent/sensible heat flux interaction [*Wang et al.*, 2017]. Trends removal of decreasing U_z and increasing q_a could increase the trend of simulated *LE* respectively. Trend removal of T_a could decrease the increasing rate of T_s, and thus decrease the *LE* through reducing water vapor gradient. In addition, it could increase the temperature gradient, then increase the trend of simulated *H*. $R_{s\downarrow}$ and $R_{l\downarrow}$ are the direct energy forcing to T_s. Trend removal of decreasing (increasing) trend in $R_{s\downarrow}$ ($R_{l\downarrow}$) could enhance (reduce) the trend of T_s, and thus increase (decrease) the trend of *LE* (*H*) through their impacts on vapor(temperature) gradients. Thus, as the Tibetan Plateau is transformed from a cold & dry environment to a warm & wet environment, $R_{l\downarrow}$ may show an increasing trend in addition to an increase in T_a. The combined effects correspond to a continuous warming of T_s and increasing trends in lake-air turbulent heat flux, which can promote positive circulation over the Tibetan Plateau.

6.6 Conclusions

To explore lakes' response to climate change over the TP, EC measurements over the open water periods of the "small lake" and the "large lake" were collected and used for evaporation evaluation. Firstly, for the evaluation of tradition evaporation estimation methods, the conclusions are summarized as follows:

(1) The difference between the **PT** method and **DK** method could be attributed to the elevation-dependent variable γ. Generally, when heat storage in the water can be precisely obtained, the energy-budget-based methods perform better than the radiation-based methods and the Dalton type methods. When the parameters used in all the methods can be optimized, the Dalton type methods approach the performance of the energy-budget-based methods, with both types of methods performing better than the radiation-based methods. However, the radiation-based methods perform well under

conditions of inadequate measurements of water temperature and heat storage in the water; for example, the Mak method yield quite similar results before and after optimization. The results reveal the significance of solar radiation and the temperature-related parameter (or *Bo*) in lake evaporation prediction.

(2) Evaporation obtained from the **Mak** method shows a decreasing-increasing variation with a turning point in 2004. This decreasing-increasing variation mainly results from the decreasing-increasing variation in solar radiation and is further controlled by the variations in air temperature. However, considering the overall trends from 1979 to 2015, trend removal and sensitivity analysis suggest that air warming plays the dominant role in the increasing rate of lake evaporation. Heat storage in the water body and water surface temperatures are key parameters in estimation of lake evaporation. Otherwise, a combination of solar radiation and air-temperature-related parameters could provide a good alternative.

Secondly, the Flake modeling indicate that:

(3) The seasonal variation of water surface temperature and turbulent heat flux could be reproduced by Flake simulation. Forcing data is very important for diurnal and seasonal variation in Flake simulation.

(4) The depth and extinction coefficients are two important parameters for Flake simulation. For simulation of the small lakes, a larger extinction coefficient show higher priority; for large lakes, an appropriate extinction coefficient could lead to correct seasonal variation of simulated turbulent heat flux. However, the diurnal variation of water surface temperature could not be reproduced both for the “small lake” and the “large lake” and a much proper parameterization scheme is needed for mixed layer depth simulation in these high-elevation lakes on the Tibetan Plateau.

(5) Land-environment forcing will show significant difference with that by lake-environment forcing, due to the significant difference in observed higher wind speed and warmer air temperature in the latter.

(6) The surface warming, reduced lake stratification lengths, and increasing trend of latent heat flux and sensible heat flux are obtained. The downward longwave radiation show the dominant role in lake warming and increasing trend of evaporation in Nam Co.

Chapter 7 Conclusions and recommendations

The observation and modeling of vertical heat exchange over high-elevation lakes on the Tibetan Plateau are very important for catchment scale water and heat budget analysis and is of great significance for modeling of lakes' response and impact to climate change over the Third Pole region. This thesis contributes to a better quantification of the vertical heat exchanges over a small lake and a large lake of Nam Co basin, Tibetan Plateau. Four research questions have been given in Chapter 1, and this Chapter mainly answers the research questions and conclude the contents in Section 7.1. After that, recommendations for future work are illustrated in Section 7.2.

7.1 Conclusions

In this thesis, to explore vertical heat exchange of high-elevation lakes of the Tibetan Plateau, comprehensive observational datasets are collected in this study. We conducted field observations in the small Nam Co lake ("small lake") during 2012-2014 and Nam Co lake ("large lake") during 2015-2017, respectively. The in-situ observations include eddy covariance data, radiation observations, lake temperature profile observations, lake level variations and traditional meteorological observations (precipitation, air pressure, wind speed, wind direction, air temperature and air humidity), in addition to the ITP forcing and MODIS products. Based on these datasets, lake-atmosphere boundary layer models (bulk aerodynamic transfer method and multi-layer method), traditional evaporation estimation methods and Flake model are evaluated and validated to achieve our objectives and answer the aforementioned four research questions. The detail of the results could resort to Chapter 3, 4, 5 and 6 respectively and the main contents are summarized as follows:

Q1. *What are the characteristics of lake-atmosphere interaction processes in these high-elevation lakes? What are the adequate schemes of roughness lengths for momentum, heat and water to predict their turbulent heat fluxes?*

To achieve the goals of understanding the characteristics of lake-atmosphere interaction, testing the applicability of the models and improving the parameterization scheme over high-elevation lakes on the Tibetan Plateau, the eddy covariance observations in the "small lake" and in the "large lake" are used as direct measurements and validation dataset for bulk aerodynamic transfer model and multi-layer model simulations. Firstly, based on the lake-atmosphere

interaction observations, we found that the daily mean water surface temperature and humidity are higher than that in the air and wind speed plays an important role in water and heat transport of these lakes, thus unstable and neutral condition dominates in the atmosphere of lakes on the Tibetan Plateau, especially for small lakes. Exceptions are expected for the "large lake" during May and June, when the water surface temperature is lower than air temperature by a combination of satellite and meteorological observations. Even though, the monthly turbulent sensible heat flux and latent heat flux are positive during the open water period of these high-elevation lakes because of the high solar heating and observed positive net radiation. Further, the square root fitting rather than linear fitting fits the observations well and it indicates that free convection conditions had a significant impact on heat and vapor fluxes at the lake-atmosphere interface.

The simulation results of B method and M method show consistency, with the former of about 10% higher in simulated turbulent heat flux than that from the latter. And both the simulated latent heat flux and sensible heat flux show an underestimation in turbulent heat flux compared with the observations. The underestimated roughness lengths could explain the underestimation of the simulated sensible heat flux and latent heat flux. Thus, we use the EC observations to optimize roughness length for momentum by calibrating the Charnock number for rough flow and roughness Reynolds number for smooth flow, with values of 0.031 and 0.54 in high-elevation lakes rather than values of 0.013 and 0.11 in oceanic research. The simulated momentum roughness lengths with optimized parameters are also close to observations relative to the original oceanic parameters. Further, the two parameters for momentum roughness length optimized in the "small lake" are also suitable for the simulation in the "large lake". The calibrated models can be applied to estimate fluxes for gap-filling when the wind direction comes from the land surface.

Q2. *What are the exact evaporations during the open-water periods of "small lake" and "large lake"? And how are the energy budget of these two water bodies?*

Precise measurements of evaporation and understanding of the physical controls on turbulent heat flux over lakes have fundamental significance for catchment-scale water balance analysis and local-scale climate modeling. To obtain the exact evaporation during open water periods of the two lakes, we used the bulk transfer method (in Chapter 3), with parameters optimized for the specific wave pattern, to provide reliable and consistent results with EC measurements. To do gap-filling for observations with inadequate footprint or malfunction of the EC

instrument, the bulk transfer method could simulate quite reasonable turbulent heat flux in the "small lake" and "large lake" respectively. The results indicate that wind speed shows significance at temporal resolution of half-hourly, whereas water vapor and temperature gradients have higher correlations over temporal resolution of daily and monthly in lake-atmosphere turbulent heat exchange of the "small lake". While the temperature gradient show high correlation with the sensible heat flux rather than the wind speed in the "large lake". The diurnal variation of sensible heat flux peaks in the early morning while that of the latent heat flux peaks in the afternoon.

The total evaporation during open-water period (April to mid-November) of the "small lake" is approximately 812 mm while the total evaporation during open-water period (May to January) of the "large lake" is 981 ± 18 mm. The energy budget during the open-water period could be around 0.97 in the "small lake" while the energy budget closure ratio during observational period of the "large lake" is 0.856. The uncertainties exist in the unmeasured heat storage in deep depth, the spatial heterogeneity of net radiation, sensible heat flux, latent heat flux, the horizontal heat transfer, the unmatched footprints of the observations, etc.

Q3. *What differences exist in lake-air interaction processes of "small lake" and "large lake"? Whether evaporation in small water bodies are suitable for evaluation of that in large water bodies?*

Lakes impact atmosphere boundary layer processes and are thus important for catchment scale climate modeling and regional water and heat budget. To explore the differences of lake-atmosphere interaction parameters, meteorological variables and turbulent heat fluxes in the "small lake" and the "large lake", we collected eddy covariance observations and meteorological data during ice-free periods of the two water bodies. Significant differences exist in their lake-atmosphere interaction processes due to differences in their inherent attributes and environmental backgrounds. Relative to the "small lake", maximum surface temperature of the "large lake" is approximately 3 ℃ lower, in addition to a larger wind speed, a higher monthly average air temperature and delayed peaks of seasonal variation of water and air temperature. The typical values of roughness length and standard bulk transfer coefficient for momentum are about 80% and 21% higher respectively in the "large lake". The typical values of roughness lengths for heat and water are one order of magnitude lower in the "large lake" while the corresponding standard bulk transfer coefficients are only 7% lower. Thus, the parameterization schemes for the roughness lengths in the "small lake"

and the "large lake" should differ. The latent and sensible heat fluxes of the two lakes have quite different seasonal variations, with evaporation peaking in November over the "large lake" and in June over the "small lake". The estimated evaporation during ice-free season of the "large lake" (around 981 ± 18 mm) is also higher than that (812 mm) in the "small lake", which is mainly related to the observed lower Bowen ratio in the "large lake". Our results show evidences that it is inappropriate to evaluate lake evaporation by Pan observations, especially for its seasonal variation.

Q4. *How are lake's responses to climate change? And what are the driving factors behind?*

Lakes are considered as an important indicator to climate change and show specific responses and effects to variations of climatic variables. In order to investigate lakes' responses to climate change over the Tibetan Plateau Lake Zone and to determine the dominant driving forces behind, the performances of traditional evaporation estimation methods and Flake modeling are evaluated by eddy covariance and meteorological data over the "small lake" during 2012-2013 and over the "large lake" during 2015-2016. The results indicate that the elevation dependent parameter γ could explain the existing differences of the simulation results between the **PT** method and **DK** method. When the parameters used in all the methods can be optimized, the Dalton type methods approach the performance of the energy-budget-based methods, with both types of methods performing better than the radiation-based methods. However, the radiation-based methods perform well under conditions of inadequate measurements of water surface temperature and heat storage in the water. Evaporation obtained from the **Mak** method shows a decreasing-increasing variation with a turning point in 2004. This decreasing-increasing variation mainly results from the decreasing-increasing variation in solar radiation and is further controlled by the variations in air temperature. However, considering the overall trends from 1979 to 2015, trend removal and sensitivity analysis suggest that air warming plays the dominant role in the increasing rate of lake evaporation.

Further, the lake processes are simulated by Flake modeling. The results indicate that the observed mixed layer depth (D_{ml}) in the "large lake" show clearly diurnal variation with monthly averaged amplitude of approximately 8 m and it results from the significant surface warming during the day and surface cooling at night. The Flake simulations could reproduce the seasonal variation of water surface temperature (T_s) and D_{ml} over daily and seasonal resolutions, but the amplitude of simulated T_s and D_{ml} are significantly underestimated. The seasonal

variations of simulated sensible heat flux (*H*) and latent heat flux (*LE*) are close to the observations with a proper extinction coefficient and lake depth, with RMSE values of simulated daily T_s, *H* and *LE* of only about 1 ℃, 8 W m^{-2} and 22 W m^{-2} respectively. The simulated *LE* through land-dominated forcing shows clear underestimation compared to that by lake-dominated forcing, and the reasons result from the observed larger wind speed and warmer air temperature in the latter. In addition, no significant differences exist for the simulations with different forcing data used in the "small lake". Lake warming and increasing trends of simulated *H* and *LE* are found through long term simulations of corrected ITP forcing. Downward longwave radiation ($R_{l\downarrow}$), rather than air temperature, is considered to play the dominant role in lake response to climate change. Our results found the significance of lake-dominant observations in lake modeling over the large lake and suggest the importance of $R_{l\downarrow}$ in lake warming and in trends of simulated *H* and *LE*.

7.2 Recommendations for future work

The vertical heat exchanges over the "small lake" and the "large lake" have been investigated using in-situ observations during the ice-free seasons of the two water bodies. However, the lake-atmosphere interaction processed during the ice-covered period should be paid more attentions by future field experiments. Sublimation over the ice-covered period of lakes have been considered to be close to zero (Ma et al. 2016), however, the sublimation during winter ice-covered period show quite high positive values in EC observations. How much evaporation during the ice-covered period should be another focus for high-elevation lakes on the Tibetan Plateau. Further, the Flake modeling show large bias in the two water bodies during periods of ice-melt, which may be related to the unsuitable description of ice-frozen processes and the improper parameterization schemes in Flake model. Thus, precise observation of ice surface temperature and the processes related to ice-formation and ice-melt needed to be carried out in the near future. Further, as lakes are always considered to be a weak carbon source to the atmosphere and it is not clear what's the role of high-elevation lakes on the Tibetan Plateau. Our observation data could provide a good data sources for the CO_2 interaction between lake and atmosphere. And these questions will be important research objectives for our future plan.

The evaporation in the "small lake" is smaller than that in the "large lake" and that could result from the differences in related meteorological observations of the two water bodies. However, as in-situ observations are always limited over

the enormous lakes on the Tibetan Plateau, how to include satellite data and reanalysis data to estimate evaporation over the other lakes on the Tibetan Plateau is another important issue. As the lake-atmosphere interaction parameters are optimized for small lake and large lake respectively and the input variables (lake surface temperature, wind speed, air temperature and humidity) of lake models can be obtained from remote sensing products and forcing data sets (such as MODIS products (Liang 2001) and ITPCAS (Institute of Tibetan Plateau research, Chinese Academy of Sciences) forcing data (Chen et al. 2011)), the calibrated models are well suited to describe lake-atmosphere heat flux in harsh and remote areas of the TP.

The evaporation is only one component of water balance in hydrological processes. After obtaining the precise evaporation over the lake surface, the issues related to precipitation, runoff, freezing-thaw processes and glacier melt water should be observed and researched in a much more detail. In addition, the spatial heterogeneity of these components, including the evaporation, precipitation and glacier melt water, are important for precise management of water resources. For example, the existence of lakes may influence the local climate through altering the spatial pattern of precipitation in the lake basin. Thus, to further simulate lakes' influence and impacts to local climate change, the validated lake models, for example, Flake model, should be coupled to regional climate model (for example, WRF), to provide accurate lake boundary layer conditions. The calibrated lake-atmosphere interaction parameters in the "small lake" and in the "large lake" are different and could provide reference values for parameterization schemes in lake modeling. Even though in-situ experiments of lake-atmosphere interaction are encouraged to carry out over lakes in different climates and environment background, our observations in the "small lake" and in the "large lake" could provide a good reference dataset for lake research over the Tibetan Plateau.

List of symbols

Greek

Symbol	Name	Units
α	Charnock Number	-
α_1	Priestley-Taylor empirically derived constant	-
γ	Psychrometric constant	Pa ℃
ε_a	Emissivity of the air	-
ε	Surface emissivity	-
ε_1	The ratio of molecular weight of water vapour to that of dry air	-
Δ	Slope of saturated vapor pressure curve	kPa K^{-1}
Γ	The profile coefficient	-
δ	The thicknesses of the molecular boundary layer	m
δ_z	The thickness of the buffer layer	m
δ_D	The thickness of the dynamical sublayer	m
σ	Stefan-Boltzmann constant	W m^{-2} K^4
Pr	The Prandtl number	-
ζ	Stability of air	-
λ	Latent heat of vaporization	J kg^{-1}
ν	Kinematic molecular viscosity	m^2 s^{-1}
ρ_a	Density of air	kg m^{-3}
v_t	Turbulent exchange coefficient	m^2 s^{-1}
v_m	Molecular exchange coefficient	m^2 s^{-1}
ρ_w	Density of water	kg m^{-3}
Ψ_h	Stability function for sensible heat transfer	-
Ψ_m	Stability function for momentum transfer	-

Roman

Symbol	Name	Units
a	Albedo of water surface	-
Bo	Bowen ratio	-
C_H	Bulk transfer coefficient for heat	-
C_E	Bulk transfer coefficient for water	-
C_p	Specific heat of air	J kg^{-1} K^{-1}
C_{pw}	Specific heat of water	J kg^{-1} K^{-1}
C_{DN10}	Bulk transfer coefficient for momentum at conditions of neutral conditions and at a reference height of 10 m	-
C_{HN10}	Bulk transfer coefficient for heat at conditions of neutral conditions and at a reference height of 10 m	-
C_{EN10}	Bulk transfer coefficient for water at conditions of neutral conditions and at a reference height of 10 m	-
C_{Dz}	Bulk transfer coefficient for momentum at observation height	-
C_{Hz}	Bulk transfer coefficient for heat at observation height	-
C_{Ez}	Bulk transfer coefficient for water at observation height	-
D_{ml}	Mixed layer depth	m
E	Evaporation	mm
E_w	Wet environment evapotranspiration	mm
E_p	Potential evapotranspiration	mm
E_s	Water vapor at the water surface	Pa
E_a	Water vapor of the air	hPa
E_{as}	The saturated vapour pressure	hPa
ΔE	The gradients of water vapor	Pa
g	Gravity acceleration	m s^{-2}
G_0	Ground surface heat flux	W m^{-2}
G_s	The heat storage change in the water	W m^{-2}
G_b	the heat transfer between water and the bottom sediments	W m^{-2}
G_a	The net energy due to water balance	W m^{-2}

G_c	The cumulative water heat storage	MJ m^{-2}
H	Sensible heat flux	W m^{-2}
k	von Karman constant	-
K_d	Extinction coefficient of the water	m^{-1}
L	Monin-Obukhov length	m
L_f	Latent heat of fusion	J kg^{-1}
L_v	latent heat of vaporization	J kg^{-1}
LE	Latent heat flux	W m^{-2}
P	Total precipitation	m
q	Specific humidity of the air	kg kg^{-1}
q_z	Specific humidity of the air at observation height	kg kg^{-1}
q_0	Specific humidity of water surface	kg kg^{-1}
q_*	Similarity scaling parameter of humidity	kg kg^{-1}
R_n	Net radiation	W m^{-2}
$R_{l\uparrow}$	Upward longwave radiation	W m^{-2}
$R_{l\downarrow}$	Downward longwave radiation	W m^{-2}
$R_{s\downarrow}$	Downward shortwave radiation	W m^{-2}
$R_{s\uparrow}$	Upward shortwave radiation	W m^{-2}
$R_r; Re$	Roughness Reynolds number	-
RH	Relative humidity	kg kg^{-1}
s	Slope of the saturated vapour pressure-temperature curve at mean air temperature	kPa ℃
ΔT	The gradients of temperature	K
t	Time	s
T	Air temperature	K
$T_0; T_s$	Surface temperature	K
T_V	Virtual air temperature	K
T_{ml}	Mixed layer temperature	K
T_d	Water temperature in the deep layer	K
$\overline{T_w}$	The mean water temperature	K
T_{wi}	The water temperature at layer i	K
T_r	The reference temperature of 0 ℃	K
T_b	Bottom layer temperature	K

T_*	Similarity scaling parameter of temperature	K
U_z	Wind speed	m s^{-1}
u_*; U_*	Friction velocity	m s^{-1}
w'	the fluctuation in the vertical wind component	m s^{-1}
z_m	Observation height of air temperature and/or wind speed	m
Z_{0h}	Roughness length for heat transfer	m
Z_{0m}	Roughness length for momentum transfer	m
Z_{0q}	Momentum roughness length for fully vegetative area	m

List of abbreviations

AWS	automatic weather station
ANN	artificial neural network
BREB	Bowen-ratio-energy-budget method
CAMP-Tibet	CEOP Asia-Australia Monsoon Project in Tibet
CRLE	Complementary Relationship Lake Evaporation method
CMA	China Meteorological Administration
EC	Eddy covariance
ECMWF	European Centre for Medium-Range Weather Forecasts
EBC	energy balance closure ratio
EOS	Earth Observation System
Flake	Fresh-water Lake model
FCCs	free convective conditions
GLDAS	Global Land Data Assimilation Systems
GAME-Tibet	GEWEX Asian Monsoon Experiment-Tibet
GEWEX	Global Energy and Water cycle Experiment
GMT	Greenwich Mean Time
ITPCAS	Institute of Tibetan Plateau Research/Chinese Academy of Sciences
LST	Land Surface Temperature
MODIS	Moderate Resolution Imaging Spectroradiometer
MOST	Monin-Obukhov Similarity Theory
NCEP	National Centers for Environmental Prediction
NASA	National Aeronautics and Space Administration
OLFM	Optimal Linear Fitting Method
PBL	Planetary Boundary Layer
TP	Tibetan Plateau
TORP	Tibetan Observation and Research Platform
TRMM	Tropical Rainfall Measuring Mission
USGS	Unites states Geological Survey
WRF	Weather Research and Forecasting model

Bibliography

Allen, R. G., L. S. Pereira, D. Raes, and M. Smith, 1998: Crop evapotranspiration - Guidelines for computing crop water requirements - FAO Irrigation and drainage paper 56. *Rome, Italy: Food and Agriculture Organization of the United Nations. ISBN 92-5-104219-5*.

Alt, H., and M. Godau, 1995: Computing the Fréchet distance between two polygal curves. *International Journal of Computational Geometry & Applications*, **05,** 75-91.

Andreas, E. L., and B. Murphy, 1986: Bulk Transfer Coefficients for Heat and Momentum over Leads and Polynyas. *Journal of Physical Oceanography*, **16,** 1875-1883.

Assouline, S., S. W. Tyler, J. Tanny, S. Cohen, E. Bou-Zeid, M. B. Parlange, and G. G. Katul, 2008: Evaporation from three water bodies of different sizes and climates: Measurements and scaling analysis. *Advances in Water Resources*, **31,** 160-172.

Ataktürk, S. S., and K. B. Katsaros, 1999: Wind Stress and Surface Waves Observed on Lake Washington. *Journal of Physical Oceanography*, **29,** 633-650.

Beljaars, A. C. M., and A. A. M. Holtslag, 1991: Flux Parameterization over Land Surfaces for Atmospheric Models. *Journal of Applied Meteorology*, **30,** 327-341.

Biermann, T., W. Babel, W. Ma, X. Chen, E. Thiem, Y. Ma, and T. Foken, 2013: Turbulent flux observations and modelling over a shallow lake and a wet grassland in the Nam Co basin, Tibetan Plateau. *Theoretical and Applied Climatology***,** 1-16.

Blanken, P. D., W. R. Rouse, and W. M. Schertzer, 2003: Enhancement of Evaporation from a Large Northern Lake by the Entrainment of Warm, Dry Air. *Journal of Hydrometeorology*, **4,** 680-693.

Blanken, P. D., C. Spence, N. Hedstrom, and J. D. Lenters, 2011: Evaporation from Lake Superior: 1. Physical controls and processes. *Journal of Great Lakes Research*, **37,** 707-716.

Blanken, P. D., and Coauthors, 2000: Eddy covariance measurements of evaporation from Great Slave Lake, Northwest Territories, Canada. *Water Resources Research*, **36,** 1069-1077.

Bourassa, M. A., D. G. Vincent, and W. L. Wood, 1999: A Flux Parameterization Including the Effects of Capillary Waves and Sea State. *Journal of the Atmospheric Sciences*, **56,** 1123-1139.

Bowen, I. S., 1926: The Ratio of Heat Losses by Conduction and by Evaporation from any Water Surface. *Physical Review*, **27,** 779-787.

Bruin, H. A. R. D., and J. Q. Keijman, 1979: The Priestley-Taylor Evaporation Model Applied to a Large, Shallow Lake in the Netherlands. *Journal of Applied Meteorology*, **18,** 898-903.

Brutsaert, W., 1982: Evaporation into the Atmosphere: Theory, History, and Applications,. *D.Reidel, Dordrecht, Netherlands.*

——, 1999: Aspects of bulk atmospheric boundary layer similarity under free-convective conditions. *Reviews of Geophysics*, **37,** 439-451.

Brutsaert, W., and H. Stricker, 1979: An advection-aridity approach to estimate actual regional evapotranspiration. *Water Resources Research*, **15,** 443-450.

Businger, J. A., J. C. Wyngaard, Y. Izumi, and E. F. Bradley, 1971: flux-profile relationship in the atmospheric surface layer. *Journal of the Atmospheric Sciences*, **28,** 181-189.

Charnock, H., 1955: Wind stress on a water surface. *Quarterly Journal of the Royal Meteorological Society*, **81,** 639-640.

Chen, B., X.-D. Xu, S. Yang, and W. Zhang, 2012: On the origin and destination of atmospheric moisture and air mass over the Tibetan Plateau. *Theor Appl Climatol*, **110,** 423-435.

Chen, Y., K. Yang, J. He, J. Qin, J. Shi, J. Du, and Q. He, 2011: Improving land surface temperature modeling for dry land of China. *Journal of Geophysical Research: Atmospheres*, **116,** D20104.

Chu, P. C., and C. Fan, 2011: Determination of Ocean Mixed Layer Depth from Profile Data. *Proceedings on 15th Symposium on Integrated Observing and Assimilation Systems for the Atmosphere, Oceans and Land Surface (IOAS-AOLS), American Meteorological Society, 23-27 January 2011, Seattle*.

Coats, R., J. Perez-Losada, G. Schladow, R. Richards, and C. Goldman, 2006: The Warming of Lake Tahoe. *Climatic Change*, **76,** 121-148.

Croley, T. E., 1989: Verifiable evaporation modeling on the Laurentian Great Lakes. *Water Resources Research*, **25,** 781-792.

Dalton, J., 1802: Experimental essays on the constitution of mixes gases: on the force of steam or vapor from water or other liquids in different temperatures, both in a Torricelli vacuum and in air; on evaporation; and on expansion of gases by heat. *Manchester Lit. Phil. Soc. Mem. Proc.*, **5,** 536-602.

De Bruin, H. A. R., 1978: A Simple Model for Shallow Lake Evaporation. *Journal of Applied Meteorology*, **17,** 1132-1134.

Deng, B., S. Liu, W. Xiao, W. Wang, J. Jin, and X. Lee, 2012: Evaluation of the CLM4 Lake Model at a Large and Shallow Freshwater Lake*. *Journal of Hydrometeorology*, **14,** 636-649.

Donelan, M., F. W. Donelan, S. D. Smith, and R. J. Anderson, 1993: On the dependence of sea surface roughness on wave development. *Journal of Physical Oceanography*, **23,** 2143-2149.

Downing, J., and Coauthors, 2006: *The Global Abundance and Size Distribution of Lakes, Ponds, and Impoundments.* Vol. 51, 2388-2397 pp.

Drexler, J. Z., R. L. Snyder, D. Spano, and K. T. Paw U, 2004: A review of models and micrometeorological methods used to estimate wetland evapotranspiration. *Hydrological Processes*, **18,** 2071-2101.

Duan, Z., and W. G. M. Bastiaanssen, 2015: A new empirical procedure for estimating intra-annual heat storage changes in lakes and reservoirs: Review and analysis of 22 lakes. *Remote Sensing of Environment*, **156,** 143-156.

Dutra, E., V. M. Stepanenko, G. Balsamo, and P. Viterbo, 2010: An offline study of the impact of lakes on the performance of the ECMWF surface scheme. *Boreal Environment Research*, **15,** 100-112.

Dyer, A. J., 1967: The turbulent transport of heat and water vapour in an unstable atmosphere. *Quarterly Journal of the Royal Meteorological Society*, **93,** 501-508.

Fairall, C. W., E. F. Bradley, D. P. Rogers, J. B. Edson, and G. S. Young, 1996a: Bulk parameterization of air-sea fluxes for Tropical Ocean-Global Atmosphere Coupled-Ocean Atmosphere Response Experiment. *Journal of Geophysical Research: Oceans*, **101,** 3747-3764.

Fairall, C. W., E. F. Bradley, D. P. Rogers, J. B. Edson, and G. S. Young, 1996b: Bulk parameterization of air-sea fluxes for Tropical Ocean Global Atmosphere Coupled Ocean Atmosphere Response Experiment. *J. Geophys. Res.,*, **101,** 3747-3764.

Fairall, C. W., E. F. Bradley, J. S. Godfrey, G. A. Wick, J. B. Edson, and G. S. Young, 1996c: Cool-skin and warm-layer effects on sea surface temperature. *Journal of Geophysical Research: Oceans*, **101,** 1295-1308.

Fang, X., and H. G. Stefan, 1996: Dynamics of heat exchange between sediment and water in a lake. *Water Resources Research*, **32,** 1719-1727.

Finch, J., and A. Calver, 2008: Methods for the quantification of evaporation from lakes. *for the World Meteorological Organization's Commission for Hydrology***,** 1-41.

Foken, T., 1979: Vorschlag eines verbesserten Energieaustauschmodells mit Berucksichtigung der molekularen Grenzschicht der Atmosphare. *Zeitschrift fur Meteorologie*, **29,** 32-39.

——, 1984: the paramiterisation of the energy exchange across the air-sea interface. *Dynamics of Atmospheres and Oceans*, **8,** 297-305.

Foken, T., 2008: Micro-meteorology. *Springer-Verlag, Berlin Heidelberg*.

Foken, T., and G. Skeib, 1983: Profile measurements in the atmospheric near-surface layer and the use of suitable universal functions for the determination of the turbulent energy exchange. *Boundary-layer Meteorology*, **25,** 55-62.

Foken, T., F. Wimmer, M. Mauder, C. Thomas, and C. Liebethal, 2006: Some aspects of the energy balance closure problem. *Atmospheric Chemictry and Physics*, **6,** 4395-4402.

Foken, T., M. Gockede, M. Mauder, L. Mahrt, B. Amiro, and W. Munger, 2004: Post-field data quality control. *Handbook of Micrometeorology***,** 181-208.

Gao, Z., Q. Wang, and S. Wang, 2006: An alternative approach to sea surface aerodynamic roughness. *Journal of Geophysical Research: Atmospheres*, **111,** D22108.

Gao, Z., Q. Wang, and M. Zhou, 2009a: Wave-Dependence of Friction Velocity, Roughness Length, and Drag Coefficient over Coastal and Open Water Surfaces by Using Three Databases. *Advances in Atmospheric Sciences*, **26,** 887-894.

——, 2009b: Wave-Dependence of Friction Velocity, Roughness Lneght, and Drag Coefficient over Coastal and Open Water Surfaces by Using Three Databases. *ADVANCES IN ATMOSPHERIC SCIENCES*, **26,** 887-894.

Gerken, T., T. Biermann, W. Babel, M. Herzog, Y. Ma, T. Foken, and H.-F. Graf, 2014: A modelling investigation into lake-breeze development and convection triggering in the Nam Co Lake basin, Tibetan Plateau. *Theoretical and Applied Climatology*, **117,** 149-167.

Gerken, T., and Coauthors, 2015: *High-resolution modelling of interactions between soil moisture and convective development in a mountain enclosed Tibetan Basin.* Vol. 19, 4023-4040 pp.

Gianniou, S. K., and V. Z. Antonopoulos, 2007: Evaporation and energy budget in Lake Vegoritis, Greece. *Journal of Hydrology*, **345,** 212-223.

Göckede, M., C. Rebmann, and T. Foken, 2004: A combination of quality assessment tools for eddy covariance measurements with footprint modelling for the characterisation of complex sites. *Agricultural and Forest Meteorology*, **127,** 175-188.

Granger, R. J., and N. Hedstrom, 2011: Modelling hourly rates of evaporation from small lakes. *Hydrol. Earth Syst. Sci.*, **15,** 267-277.

Guo, Y., Y. Zhang, N. Ma, H. Song, and H. Gao, 2016: Quantifying Surface Energy Fluxes and Evaporation over a Significant Expanding Endorheic Lake in the Central Tibetan Plateau. *気象集誌. 第 2 輯*, **94,** 453-465.

Haginoya, S., H. Fujii, T. Kuwagata, J. Xu, Y. Ishigooka, S. Kang, and Y. Zhang, 2009: Air-Lake Interaction Features Found in Heat and Water Exchanges over Nam Co on the Tibetan Plateau. *Scientific Online Letters on the Atmosphere*, **5,** 172-175.

Hampton, S. E., L. R. Izmest'Eva, M. V. Moore, S. L. Katz, B. Dennis, and E. A. Silow, 2008: Sixty years of environmental change in the world's largest freshwater lake – Lake Baikal, Siberia. *Global Change Biology*, **14,** 1947-1958.

He, J., and K. Yang, 2011: China Meteorological Forcing Dataset. Cold and Arid Regions Science Data Center. *Lanzhou*, **China**.

Heikinheimo, M., M. Kangas, T. Tourula, A. Venäläinen, and S. Tattari, 1999: Momentum and heat fluxes over lakes Tämnaren and Råksjö determined by the bulk-aerodynamic and eddy-correlation methods. *Agricultural and Forest Meteorology*, **98–99,** 521-534.

Hicks, B. B., and G. D. Hess, 1977: On the Bowen Ratio and Surface Temperature at Sea. *Journal of Physical Oceanography*, **7,** 141-145.

Hobbins, M. T., J. A. Ramirez, and T. C. Brown, 2004: Trends in pan evaporation and actual evapotranspiration across the conterminous US: paradoxical or complementary? *Geophysical Research Letters*, **31L13503,** L13503.

Huang, C. H., 2012: Modification of the Charnock Wind Stress Formula to Include the Effects of Free Convection and Swell. *Advanced Methods for Practical Applications in Fluid Mechanics*, **Prof. Steven Jones (Ed.),** ISBN: 978-953-951-0241-0240, InTech.

Huang, L., J. Wang, L. Zhu, J. Ju, and G. Daut, 2017: The Warming of Large Lakes on the Tibetan Plateau: Evidence From a Lake Model Simulation of Nam Co, China, During 1979–2012. *Journal of Geophysical Research: Atmospheres*, **122,** 13,095-013,107.

Hull, J. R., 1979: *Physics of the solar pond.*

Immerzeel, W. W., L. P. H. van Beek, and M. F. P. Bierkens, 2010: Climate Change Will Affect the Asian Water Towers. *Science*, **328,** 1382-1385.

Katsaros, K. B., 1998: turbulent flux of water vapor in relation to the wave field and atmospheric stratification, in Physical Processes in Lakes and Oceans. *Coastal Estuarine Stud.*, **54,edited by J.Imberger,** 157-172 AGU, Washington, D.C.

Kersten, M. S., 1949: Thermal properties of soils. Bulletin 28, 227 pp.

Kirillin, G., L. Wen, and T. Shatwell, 2017: Seasonal thermal regime and climatic trends in lakes of the Tibetan highlands. *Hydrol. Earth Syst. Sci.*, **21,** 1895-1909.

Krop¨¢£¿ek, J., F. Maussion, F. Chen, and S. Hoerz, 2013: Analysis of ice phenology of lakes on the Tibetan Plateau from MODIS data. *The Cryosphere*.

Large, W. G., and S. Pond, 1981: Open Ocean Momentum Flux Measurements in Moderate to Strong Winds. *Journal of Physical Oceanography*, **11,** 324-336.

——, 1982: Sensible and Latent Heat Flux Measurements over the Ocean. *Journal of Physical Oceanography*, **12,** 464-482.

Lazhu, and Coauthors, 2016: Quantifying evaporation and its decadal change for Lake Nam Co, central Tibetan Plateau. *Journal of Geophysical Research: Atmospheres*, **121,** 7578-7591.

Lee, X., and Coauthors, 2014: The Taihu Eddy Flux Network: An Observational Program on Energy, Water, and Greenhouse Gas Fluxes of a Large Freshwater Lake. *Bulletin of the American Meteorological Society*, **95,** 1583-1594.

Lei, Y., T. Yao, B. W. Bird, K. Yang, J. Zhai, and Y. Sheng, 2013: Coherent lake growth on the central Tibetan Plateau since the 1970s: Characterization and attribution. *Journal of Hydrology*, **483,** 61-67.

Li, W., S. Li, and P. Pu, 2001: Estimates of Plateau Lake Evaporation: A case Study of Zige Tangco. *Journal of Lake Sciences (in Chinese)*, **13,** 227-232.

Li, X.-Y., H.-Y. Xu, Y.-L. Sun, D.-S. Zhang, and Z.-P. Yang, 2007: Lake-Level Change and Water Balance Analysis at Lake Qinghai, West China during Recent Decades. *Water Resources Management*, **21,** 1505-1516.

Li, X.-Y., and Coauthors, 2016: Evaporation and surface energy budget over the largest high-altitude saline lake on the Qinghai-Tibet Plateau. *Journal of Geophysical Research: Atmospheres*, **121,** 10,470-410,485.

Li, Z., S. Lyu, L. Zhao, L. Wen, Y. Ao, and S. Wang, 2015a: Turbulent transfer coefficient and roughness length in a high-altitude lake, Tibetan Plateau. *Theor Appl Climatol***,** 1-13.

Li, Z., S. Lyu, Y. Ao, L. Wen, L. Zhao, and S. Wang, 2015b: Long-term energy flux and radiation balance observations over Lake Ngoring, Tibetan Plateau. *Atmospheric Research*, **155,** 13-25.

Liang, S., 2001: Narrowband to broadband conversions of land surface albedo I: Algorithms. *Remote Sensing of Environment*, **76,** 213-238.

Liu, B., M. Xu, M. Henderson, and W. Gong, 2004: A spatial analysis of pan evaporation trends in China, 1955–2000. *Journal of Geophysical Research: Atmospheres*, **109,** n/a-n/a.

Liu, H., Q. Zhang, and G. Dowler, 2012: Environmental Controls on the Surface Energy Budget over a Large Southern Inland Water in the United States: An Analysis of One-Year Eddy Covariance Flux Data. *Journal of Hydrometeorology*, **13,** 1893-1910.

Liu, H., Y. Zhang, S. Liu, H. Jiang, L. Sheng, and Q. L. Williams, 2009a: Eddy covariance measurements of surface energy budget and evaporation in a cool season over southern open water in Mississippi. *Journal of Geophysical Research: Atmospheres*, **114,** D04110.

Liu, H. Z., J. W. Feng, J. H. Sun, L. Wang, and A. L. Xu, 2014: Eddy covariance measurements of water vapor and CO2 fluxes above the Erhai lake. *Science China: Earth Science (in Chinese)*, **44,** 2527-2539.

Liu, J., S. Wang, S. Yu, D. Yang, and L. Zhang, 2009b: Climate warming and growth of high-elevation inland lakes on the Tibetan Plateau. *Global and Planetary Change*, **67,** 209-217.

Liu, W. T., K. B. Katsaros, and J. A. Businger, 1979: bulk parameterization of air-sea exchange of heat and water vapor including the molecular constraints at the interface. *Journal of the Atmospheric Sciences*, **36,** 1722-1735.

Long, Z., W. Perrie, J. Gyakum, D. Caya, and R. Laprise, 2007: Northern Lake Impacts on Local Seasonal Climate. *Journal of Hydrometeorology*, **8,** 881-896.

Lv, Y., 2008: Summertime numerical simulation and obervation of characteristic of ABL and local circulation over the Nam Co lake of the Tibetan Plateau. *Thesis*.

Lv, Y., Y. Ma, M. Li, and X. Yang, 2008: Numerical simulation of typical atmospheric boundary layer characteristics over lake Nam Co region

Tibetan Plateau in summer (in Chinese with English abstract). *Plateau Meteorology*, **25,** 733-740.

Ma, N., J. Szilagyi, G.-Y. Niu, Y. Zhang, T. Zhang, B. Wang, and Y. Wu, 2016: Evaporation variability of Nam Co Lake in the Tibetan Plateau and its role in recent rapid lake expansion. *Journal of Hydrology*, **537,** 27-35.

Ma, R., and Coauthors, 2011: China's lakes at present: Number, area and spatial distribution. *Science China Earth Sciences*, **54,** 283-289.

Ma, Y., O. Tsukamoto, J. Wang, H. Ishikawa, and I. Tamagawa, 2002: Analysis of aerodynamic and thermodynamic parameters over the grassy marshland surface of Tibetan Plateau. *Prog. Nat. Sci.*, **12,** 36-40.

Ma, Y., L. Zhong, Z. Su, H. Ishikawa, M. Menenti, and T. Koike, 2006: Determination of regional distributions and seasonal variations of land surface heat fluxes from Landsat-7 Enhanced Thematic Mapper data over the central Tibetan Plateau area. *J. Geophys. Res.*, **111,** 1-12.

Ma, Y., Z. Zhu, L. Zhong, B. Wang, C. Han, Z. Wang, and et.al, 2014: Combining MODIS, AVHRR and in situ data for evapotranspiration estimation over heterogeneous landscape of the Tibetan Plateau. *Atmospheric Chemictry and Physics*, **14,** 1507-1515.

Ma, Y., and Coauthors, 2004: Diurnal and inter-monthly variation of land surface heat fluxes over the central Tibetan Plateau area. *Theoretical and Applied Climatology*, **80,** 259-273.

Ma, Y., and Coauthors, 2009: Recent advances on the study of atmosphere-land interaction observations on the Tibetan Plateau. *Hydrol. Earth Syst. Sci.*, **13,** 1103-1111.

MaGuinness, J. L., and E. F. Bordne, 1972: A comparison of lysimeter-derived potential evapotranspiration with computed values. *Technical Bulletin 1452, US Department of Agriculture Africultural Research Service, Washington, DC.*

Mangarella, P. A., A. J. Chambers, R. I. Street, and E. Y. Hsu, 1973: Laboratory studies of evaporation and energy transfer through a wavy air-water interface. *Journal of Physical Oceanography*, **3,** 93-101.

Martynov, 2012: Interactive lakes in the Canadian Regional Climate Model, version 5: the role of lakes in the regional climate of North America. *Tellus A: Dynamic Meteorology and Oceanography*, **64**.

Massman, W. J., 1999: A model study of kB for vegetated surfaces using 'localized near-field' Lagrangian theory. *Journal of Hydrology*, **223,** 27-43.

Mauder, M., and F. Thomas, 2015: Eddy-Covariance Software TK3. *zenodo*.

McGuinness, J. L., and E. F. Bordne, 1972: A comparison of lysimeter-derived potential evapotranspiration with computed values, Tech Bull. *1452, 71 pp., Afric. Res. Serv., U.S. Dept. of Agric., Washing-ton, D.C.*

Menenti, M., and J. C. Ritchie, 1994: Estimation of effective aerodynamic roughness of Walnut Gulch watershed with laser altimeter measurements. *Water Resources Research*, **30,** 1329-1337.

Merlivat, L., and M. Coantic, 1975: Study of mass transfer at the air-water interface by an isotopic method. *J. Geophys. Res.*, **80,** 3455-3464.

Miehe, G., and Coauthors, 2011: Plant communities of central Tibetan pastures in the Alpine Steppe/Kobresia pygmaea ecotone. *Journal of Arid Environments*, **75,** 711-723.

Mironov, D., 2008: Parameterization of lakes in numerical weather prediction: description of a lake model. *COSMO Technical Report*, **11,** 47.

Monin, A. S., and A. M. Yaglom, 1965: Statisticeskaja gidromechanika,c.1.lzd.Nauka. *Moscow***,** 640.

Morrill, C., 2004: The influence of Asian summer monsoon variability on the water balance of a Tibetan lake. *Journal of Paleolimnology*, **32,** 273-286.

Nordbo, A., S. Launiainen, I. Mammarella, M. Leppäranta, J. Huotari, A. Ojala, and T. Vesala, 2011: Long-term energy flux measurements and energy balance over a small boreal lake using eddy covariance technique. *Journal of Geophysical Research: Atmospheres*, **116,** D02119.

O'Reilly, C. M., and Coauthors, 2015: Rapid and highly variable warming of lake surface waters around the globe. *Geophysical Research Letters*, **42,** 10,773-710,781.

Oku, Y., H. Ishikawa, S. Haginoya, and Y. Ma, 2006: Recent Trends in Land Surface Temperature on the Tibetan Plateau. *Journal of Climate*, **19,** 2995-3003.

Oswald, C. J., and W. R. Rouse, 2004: Thermal Characteristics and Energy Balance of Various-Size Canadian Shield Lakes in the Mackenzie River Basin. *Journal of Hydrometeorology*, **5,** 129-144.

Panin, G. N., and T. Foken, 2005: Air–sea interaction including a shallow and coastal zone. *Journal of Atmospheric & Ocean Science*, **10,** 289-305.

Panin, G. N., A. E. Nasonov, T. Foken, and H. Lohse, 2006: On the parametersisaton of evaporation and sensible heat exchange for shallow lakes. *Theoretical and Applied Climatology*, **85,** 123-129.

Panofsky, H. A., and J. A. Dutton, 1984: Atmospheric Turbulence. *Wiley-Interscience, New York***,** 397.

Penman, H. L., 1948: Natural Evaporation from Open Water, Bare Soil and Grass. *Proceedings of the Royal Society of London. Series A. Mathematical and Physical Sciences*, **193,** 120-145.

Perroud, M., S. Goyette, A. Martynov, M. Beniston, and O. Annevillec, 2009: Simulation of multiannual thermal profiles in deep Lake Geneva: A comparison of one-dimensional lake models. *Limnology and Oceanography*, **54,** 1574-1594.

Pond, S., D. B. Fissel, and C. A. Paulson, 1974: A note on bulk aerodynamic coefficients for sensible heat and moisture fluxes. *Boundary-layer Meteorology*, **6,** 333-339.

Priestley, C. H. B., and R. J. Taylor, 1972: On the Assessment of Surface Heat Flux and Evaporation Using Large-Scale Parameters. *Monthly weather review*, **100,** 81-92.

Rosenberry, D. O., T. C. Winter, D. C. Buso, and G. E. Likens, 2007: Comparison of 15 evaporation methods applied to a small mountain lake in the northeastern USA. *Journal of Hydrology*, **340,** 149-166.

Rouse, W. R., C. M. Oswald, J. Binyamin, P. D. Blanken, W. M. Schertzer, and C. Spence, 2003: Interannual and seasonal variability of the surface energy balance and temperature of Central Great Slave Lake. *J. Hydrometeor,*, **4,** 720-730.

Rouse, W. R., and Coauthors, 2005: The Role of Northern Lakes in a Regional Energy Balance. *Journal of Hydrometeorology*, **6,** 291-305.

Sempreviva, A., S. E. Larsen, N. G. Mortensen, and I. Troen, 1990: Response of neutral boundary layers to changes of roughness. *Boundary-Layer Meteorol*, **50,** 205-225.

Shi, X., S. Li, Andi, D. Li, and Z. Su, 2010: A study of the change of Qinghai Lake evaporation. *Climatic and Environmental Research (in Chinese)*, **15,** 787-796.

Shigenori, H., F. Hideyuki, K. Tsuneo, and X. Jianqing, 2009: air-lake interaction features found in heat and water exchanges over Nam Co on the Tibetan Plateau. *SOLA*, **5,** 172-175.

Singh, P., and K. Nakamura, 2009: Diurnal variation in summer precipitation over the central Tibetan Plateau. *Journal of Geophysical Research: Atmospheres*, **114,** D20107.

Singh, V. P., and C.-Y. Xu, 1997: EVALUATION AND GENERALIZATION OF 13 MASS-TRANSFER EQUATIONS FOR DETERMINING FREE WATER EVAPORATION. *Hydrol. Process.*, **11,** 311-323.

Small, E. E., and S. Kurc, 2001: The Influence of Soil Moisture on the Surface Energy Balance in Semiarid Environments. New Mexico Water Resources Research Institute.

Smith, S., and Coauthors, 1992: Sea surface wind stress and drag coefficients: The hexos results. *Boundary-Layer Meteorol*, **60,** 109-142.

Smith, S. D., 1988: Coefficients for sea surface wind stress, heat flux, and wind profiles as a function of wind speed and temperature. *Journal of Geophysical Research: Oceans*, **93,** 15467-15472.

——, 1989: Water vapor flux at the sea surface. *Boundary-Layer Meteorol*, **47,** 277-293.

Spence, C., P. D. Blanken, N. Hedstrom, V. Fortin, and H. Wilson, 2011: Evaporation from Lake Superior: 2: Spatial distribution and variability. *Journal of Great Lakes Research*, **37,** 717-724.

Stepanenko, V., and Coauthors, 2014a: Simulation of surface energy fluxes and stratification of a small boreal lake by a set of one-dimensional models. *Tellus A: Dynamic Meteorology and Oceanography*, **66,** 21389.

——, 2014b: Simulation of surface energy fluxes and stratification of a small boreal lake by a set of one-dimensional models. *Tellus A*.

Subin, Z. M., W. J. Riley, and D. Mironov, 2012: An improved lake model for climate simulations: Model structure, evaluation, and sensitivity analyses in CESM1. *Journal of Advances in Modeling Earth Systems*, **4,** M02001.

Sugita, M., H. Ikura, A. Miyano, K. Yamamoto, and W. Zhongwang, 2014: Evaporation from Lake Kasumigaura: annual totals and variability in time and space. *Hydrological Research Letters*, **8,** 103-107.

Szilagyi, J., 2008: Comment on "Comparison of 15 evaporation models applied to a small mountain lake in the northeastern USA" by D.O. Rosenberry, T.C. Winter, D.C. Buso, and G.E. Likens [J. Hydrol. 340 (3-4)(2007) 149-166]. *Journal of Hydrology*, **348,** 564-565.

Tanaka, K., H. Ishikawa, I. T. Hayashi, and Y. Ma, 2001: Surface energy budget at Amdo on Tibetan Plateau using GAME/Tibet IOP'98 Data. *J. Meteor. Soc. Japan*, **79(1B),** 505-517.

Tanaka, K., I. Tamagawa, H. Ishikawa, Y. Ma, and Z. Hu, 2003: Surface energy budget and closure of the eastern Tibetan Plateau during the GAME/Tibet IOP 1998. *Journal of Hydrology*, **283**.

Tanny, J., and Coauthors, 2008: Evaporation from a small water reservoir: Direct measurements and estimates. *Journal of Hydrology*, **351,** 218-229.

Taylor, P., R. I. Sykes, and P. Mason, 1989: On the parameterization of drag over small-scale topography in neutrally-stratified boundary-layer flow. *Boundary-Layer Meteorol*, **48,** 409-422.

Thiery, W., E. L. Davin, H.-J. Panitz, M. Demuzere, S. Lhermitte, and N. v. Lipzig, 2015: The Impact of the African Great Lakes on the Regional Climate. *Journal of Climate*, **28,** 4061-4085.

Thiery, W., A. Martynov, F. Darchambeau, J. P. Descy, P. D. Plisnier, L. Sushama, and N. P. M. van Lipzig, 2014a: Understanding the performance of the FLake model over two African Great Lakes. *Geosci. Model Dev.*, **7,** 317-337.

Thiery, W., and Coauthors, 2014b: LakeMIP Kivu: Evaluating the representation of a large, deep tropical lake by a set of 1-dimensional lake models. *Tellus*, **66**.

Thomson, R. E., and I. V. Fine, 2003: Estimating Mixed Layer Depth from Oceanic Profile Data. *Journal of Atmospheric and Oceanic Technology*, **20,** 319-329.

Venalainen, A., M. Frech, and M. Heikinheimo, 1999: Comparison of latent and sensible heat fluxes over boreal lakes with concurrent fluxes over a forest: implications for regional averaging. *Agricultural and Forest Meteorology*, **98-99,** 535-546.

Verburg, P., and J. P. Antenucci, 2010: Persistent unstable atmospheric boundary layer enhances sensible and latent heat loss in a tropical great lake: Lake Tanganyika. *J. Geophys. Res.*, **115**.

Vickers, D., and L. Mahrt, 2010: Sea-surface roughness lengths in the midlatitude coastal zone. *Q. J. R. Meteorol. Soc.*

Vincent, A. C., D. R. Mueller, and W. F. Vincent,, 2008: Simulated heat storage in a perennially ice-covered high Arctic lake: Sensitivity to climate change. *J. Geophys. Res.,*, **113**.

Vörös, M., V. Lstvánovics, and T. Weidinger, 2010: Applicability of the FLake model to Lake Balaton. *Boreal Environment Research*, **15,** 245-254.

Wang, B., Y. Ma, W. Ma, and Z. Su, 2017: Physical controls on half-hourly, daily and monthly turbulent flux and energy budget over a high-altitude small lake on the Tibetan Plateau. *Journal of Geophysical Research: Atmospheres***,** n/a-n/a.

Wang, B., Y. Ma, W. Ma, B. Su, and X. Dong, 2018: Evaluation of ten methods for estimating evaporation in a small high-elevation lake on the Tibetan Plateau. *Theoretical and Applied Climatology*.

Wang, B., Y. Ma, X. Chen, W. Ma, Z. Su, and M. Menenti, 2015: Observation and simulation of lake-air heat and water transfer processes in a high-altitude shallow lake on the Tibetan Plateau. *Journal of Geophysical Research: Atmospheres*, **120,** 12327-12344.

Wang, J., L. Zhu, G. Daut, J. Ju, X. Lin, Y. Wang, and X. Zhen, 2009a: Investigation of bathymetry and water quality of Lake Nam Co, the largest lake on the central Tibetan Plateau, China. *Limnology*, **10,** 149-158.

——, 2009b: Bathymetric survey and modern limnological parameters of Nam Co, centranl Tibet. *J.Lake Sci.*, **21,** 128-134.

Wang, S., and H. Dou, 1998: *An overview of lakes over China*. Science Press (in Chinese).

Wang, W., and Coauthors, 2014: Temporal and spatial variations in radiation and energy balance across a large freshwater lake in China. *Journal of Hydrology*, **511,** 811-824.

Webb, E. K., G. I. Pearman, and R. Leuning, 1980: Correction of flux measurements for density effects due to heat and water vapour transfer. *Quarterly Journal of the Royal Meteorological Society*, **106,** 85-100.

Webster, P. J., and R. Lukas, 1992: TOGA COARE: The Coupled Ocean—Atmosphere Response Experiment. *Bulletin of the American Meteorological Society*, **73,** 1377-1416.

Wei, D., X. Ri, Y. Wang, Y. Wang, Y. Liu, and T. Yao, 2012: Responses of CO2, CH4 and N2O fluxes to livestock exclosure in an alpine steppe on the Tibetan Plateau, China. *Plant Soil*, **359,** 45-55.

Wen, L., S. Lv, Z. Li, L. Zhao, and N. Nagabhatla, 2015: Impacts of the Two Biggest Lakes on Local Temperature and Precipitation in the Yellow River Source Region of the Tibetan Plateau. *Advances in Meteorology*, **2015,** 10.

Wen, L., S. Lyu, G. Kirillin, Z. Li, and L. Zhao, 2016: Air-lake boundary layer and performance of a simple lake parameterization scheme over the Tibetan highlands. *2016*.

Whalin, R. W., F.E. Camfield, N.E.Parker, R.A.Jachowski, and J. R. W. (Eds.), 1984: Shore Protection Manual, **1**.

Wilczak, J. M., S. P. Oncley, and S. A. Stage, 2000: Sonic anemometer tilt correction algorithms. *Boundary-layer Meteorology*, **99,** 127-150.

Winter, T. C., D. O. Rosenberry, and A. M. Sturrock, 1995: Evaluation of 11 Equations for Determining Evaporation for a Small Lake in the North Central United States. *Water resources research*, **31,** 983-993.

Wu, J., 1980: Wind-Stress coefficients over Sea surface near Neutral Conditions—A Revisit. *Journal of Physical Oceanography*, **10,** 727-740.

——, 1994: The sea surface is aerodynamically rough even under light winds. *Boundary-Layer Meteorol*, **69,** 149-158.

Wu, Y., H. Zheng, B. Zhang, D. Chen, and L. Lei, 2014: Long-Term Changes of Lake Level and Water Budget in the Nam Co Lake Basin, Central Tibetan Plateau. *Journal of Hydrometeorology*, **15,** 1312-1322.

Xiao, W., and Coauthors, 2013: Transfer Coefficients of Momentum, Heat and Water Vapour in the Atmospheric Surface Layer of a Large Freshwater Lake. *Boundary-Layer Meteorol*, **148,** 479-494.

Xing, W., W. Wang, Q. Shao, Z. Yu, T. Yang, and J. Fu, 2016: Periodic fluctuation of reference evapotranspiration during the past five decades: Does Evaporation Paradox really exist in China? *Scientific Reports*, **6,** 39503.

Xu, C.-y., L. Gong, T. Jiang, D. Chen, and V. P. Singh, 2006: Analysis of spatial distribution and temporal trend of reference evapotranspiration and pan evaporation in Changjiang (Yangtze River) catchment. *Journal of Hydrology*, **327,** 81-93.

Xu, C. Y., and V. P. Singh, 2001: Evaluation and generalization of temperature-based methods for calculating evaporation. *Hydrological Processes*, **15,** 305-319.

Xu, J., and Coauthors, 2009: The Implication of Heat and Water Balance Changes in a Lake Basin on the Tibetan Plateau. *Hydrological Research Letters*, **3,** 1-5.

Yang, K., T. Koike, H. Fujii, K. Tamagawa, and N. Hirose, 2002: Improvement of surface flux parametrizations with a turbulence-related length. *Quarterly Journal of the Royal Meteorological Society*, **128,** 2073-2087.

Yang, K., H. Wu, J. Qin, C. Lin, W. Tang, and Y. Chen, 2014: Recent climate changes over the Tibetan Plateau and their impacts on energy and water cycle: A review. *Global and Planetary Change*, **112,** 79-91.

Yang, K., H. Lu, S. Yue, G. Zhang, Y. Lei, Z. La, and W. Wang, 2017: Quantifying recent precipitation change and predicting lake expansion in the Inner Tibetan Plateau. *Climatic Change*.

Yang, K., and Coauthors, 2008: Turbulent flux transfer over bare-soil surfaces: characteristics and parameterization. *J. Appl. Meteor. Climatol.*,, **47,** 276-290.

Yang, M., F. E. Nelson, N. I. Shiklomanov, D. Guo, and G. Wan, 2010: Permafrost degradation and its environmental effects on the Tibetan Plateau: A review of recent research. *Earth-Science Reviews*, **103,** 31-44.

Yao, H. X., 2009: Long-Term Study of Lake Evaporation and Evaluation of Seven Estimation Methods: Results from Dickie Lake, South-Central Ontario, Canada. *Journal of Water Resource & Protection*, **01,** 59-77.

Yao, T., Y. Wang, S. Liu, J. Pu, Y. Shen, and A. Lu, 2004: Recent glacial retreat in High Asia in China and its impact on water resource in Northwest China. *Science in China Series D-Earth Sciences*, **47,** 1065.

Yu, S., J. Liu, J. Xu, and H. Wang, 2011: Evaporation and energy balance estimates over a large inland lake in the Tibet-Himalaya. *Environmental Earth Sciences*, **64,** 1169-1176.

Zeng, X., M. Zhao, and R. E. Dickinson, 1998: Intercomparison of Bulk Aerodynamic Algorithms for the Computation of Sea Surface Fluxes Using TOGA COARE and TAO Data. *Journal of Climate*, **11,** 2628-2644.

Zhang, B., Y. Wu, L. Zhu, J. Wang, J. Li, and D. Chen, 2011a: Estimation and trend detection of water storage at Nam Co Lake, central Tibetan Plateau. *Journal of Hydrology*, **405,** 161-170.

Zhang, G., H. Xie, S. Kang, D. Yi, and S. F. Ackley, 2011b: Monitoring lake level changes on the Tibetan Plateau using ICESat altimetry data (2003–2009). *Remote Sensing of Environment*, **115,** 1733-1742.

Zhang, G., T. Yao, H. Xie, K. Zhang, and F. Zhu, 2014: Lakes' state and abundance across the Tibetan Plateau. *Chin. Sci. Bull.*, **59,** 3010-3021.

Zhang, Q., and H. Liu, 2014: Seasonal changes in physical processes controlling evaporation over inland water. *Journal of Geophysical Research: Atmospheres***,** 2014JD021797.

Zhou, D., R. Eigenmann, W. Babel, T. Foken, and Y. Ma, 2011: The study of near-ground free convection conditions at Nam Co station on the Tibetan Plateau. *Theor Appl Climatol*, **105,** 217-228.

Zhou, S., S. Kang, F. Chen, and D. R. Joswiak, 2013a: Water balance observations reveal significant subsurface water seepage from Lake Nam Co, south-central Tibetan Plateau. *Journal of Hydrology*, **491,** 89-99.

——, 2013b: Water balance observations reveal significant subsurface water seepage from Lake Nam Co, south-central Tibetan Plateau. *Journal of Hydrology*, **491,** 89-99.

Zhu, L., M. Xie, and Y. Wu, 2010: Quantitative analysis of lake area variations and the influence factors from 1971 to 2004 in the Nam Co basin of the Tibetan Plateau. *Chin. Sci. Bull.*, **55,** 1294-1303.

Zhu, L., J. Jin, X. Liu, L. Tian, and Q. Zhang, 2017: Simulations of the Impact of Lakes on Local and Regional Climate Over the Tibetan Plateau. *Atmosphere-Ocean***,** 1-10.

Zilitinkevich, S., and D. V. Mironov, 1996: A multi-limit formulation for the equilibrium depth of a stably stratified boundary layer. *Boundary-Layer Meteorol*, **81,** 325-351.

Zolfaghari, K., C. R. Duguay, and H. Kheyrollah Pour, 2017: Satellite-derived light extinction coefficient and its impact on thermal structure simulations in a 1-D lake model. *Hydrol. Earth Syst. Sci.*, **21,** 377-391.